Studies on Chaotic Quantum Systems

Thesis submitted to

The University of Gujarat

for the Degree of

Doctor of Philosophy

in

Physics

by

M. S. SANTHANAM

August 1997

PHYSICAL RESEARCH LABORATORY
NAVRANGPURA, AHMEDABAD 380 009
INDIA

CERTIFICATE

I hereby declare that the work presented in this thesis is original and has not formed basis for the award of any degree or diploma by any University or Institution.

M. S. Santhanam
(Author)

Certified by:

Prof V. B. Sheorey
(Thesis Supervisor)
Physical Research Laboratory
Ahmedabad 380 009, India

Contents

1 Introduction **3**

1.1 Classical Chaos 4

1.1.1 Classical Phase Space Structure and Dynamics 6

1.2 Quantum Chaos 7

1.3 Numerical Techniques 9

1.4 Chaos in Physical Systems 10

1.5 Quantisation 11

1.5.1 Study of Eigenvalue Spectrum 12

1.5.2 Random Matrix Theory 13

1.6 Eigenfunctions and Its Structures 14

1.6.1 Scars of Classical Orbits 15

1.7 Localisation 16

1.7.1 Models for Localisation 17

1.7.2 Localisation in Nonlinear Oscillators 18

2 Parametric Scaling in Nonlinear Oscillators **21**

2.1 Parametric Scaling 21

2.2 Scaling of Poincaré Maps 26

2.3 Classical Dynamics of Coupled Quartic Oscillator 29

3 Quantum Mechanics of Nonlinear Oscillators **32**

3.1 Techniques for Solving Schroedinger Equation 33

3.1.1 Basis Set Diagonalisation 33

3.2 Discrete Symmetries of the Potential 34

3.3 Numerical Techniques 36

3.4 Numerical Banding of Hamiltonian Matrices 37

3.5 Accuracy and Errors 39

4 Localisation in Quartic Oscillators **42**

4.1 Scarred States in Quartic Oscillator 43

4.1.1 Husimi Distribution and the Scarring Orbit 44

4.2 Identification of Localised States 48

4.3 Information Entropy and Random Matrix Predictions 50

4.4 Structure of Localised States 54

4.5 Adiabatic Approaches for The Quartic Oscillator 60

4.6 Localisation and Stability 65

5 Three-dimensional Systems **75**
5.1 3D Sextic Oscillator 76
5.2 3D Coupled Quartic Oscillator 79
5.3 Group Structure of Quartic Oscillator 79
5.3.1 The Octahedral Group 81
5.3.2 The D_{4h} Group 82
5.3.3 The D_{2h} Group 83
5.4 Eigenvalue Spacing Distribution 84

6 Conclusions and Future Directions **88**

Bibliography **93**

Introduction

Systems that evolve with time are called dynamical systems. They encompass a wide variety of systems, from the purely mathematical and idealised constructs to microscopic physical systems like the atoms and macroscopic ones like the planets, eco-systems, weather and even stock market dynamics. Over the last five hundred years or so, the dynamical laws that govern the motion of the material particles have been formulated and have been successfully applied to many cases, the most famous being the prediction of the return of the Halley's comet. This triumph of classical physics had only served to reinforce one of its central premise, namely determinism, implying that the evolution of any dynamical system can be precisely *determined and predicted* for all the past and future times, if the initial conditions are known. In the language of mathematics, such dynamical systems are described by deterministic differential equations of the form $(d\mathbf{x}/dt) = \mathbf{f}(\mathbf{x})$, without any externally imposed random input in the equations. If we imagine the dynamics to be taking place in discrete time steps, then dynamical equations are the difference equations of the form, $\mathbf{x}_{n+1} = \mathbf{f}(\mathbf{x}_n)$, where n represents the discrete time steps.

An important class of dynamical systems are the Hamiltonian systems characterised by a Hamiltonian function $H(\mathbf{p}, \mathbf{q}, t)$, where $\mathbf{p}$ and $\mathbf{q}$ are the $2N$ dynamical variables for N degree of freedom systems. The dynamical system is defined by canonical or Hamilton's equation,

$$\dot{\mathbf{p}} = -\frac{\partial H}{\partial \mathbf{q}}, \qquad\qquad \dot{\mathbf{q}} = \frac{\partial H}{\partial \mathbf{p}}. \tag{1.1}$$

If the Hamiltonian is independent of time, then $H(\mathbf{p}, \mathbf{q})$ is a constant of motion. The dynamics is viewed in phase space, whose axes is labelled by each component of $\mathbf{q}$ and $\mathbf{p}$. The trajectory, $(\mathbf{q}(t), \mathbf{p}(t))$ determined *uniquely* by the given initial conditions constitutes the solution of these equations. In most cases, however, only simple systems like the pendulum or the two body problem, for instance sun and the earth, could be solved exactly. The exactly solvable systems are special in that they possess as many constants of motion as the number of degrees of freedom to facilitate the reduction of the problem to quadratures, *i.e* to performing an integral, and hence called integrable systems. They constitute prototype text-book classical systems that are regular and predictable.

But integrable systems are rather exceptional in nature. For instance, even the three body problem, the sun-earth-moon system leads to insurmountable difficulties in analytical treatment and is shown to be non-integrable except for certain special

configuration of the three bodies. However, in the other extreme limit of a large number of particles, like say 10^{23} atoms of gas in a container, statistical methods have been applied to obtain the ensemble averaged values for the physically relevant quantities, but the corresponding trade-off is in terms of the knowledge of the detailed behaviour of the individual particles. The crucial point to note is that the equations of motion (1.1) based on Newton's laws can be exactly solved only for a few systems with *simple* interactions. Since the whole edifice of classical physics and its understanding was built on such simple systems, it was widely believed till the end of the last century that any system with a given interaction is solvable but only that necessary analytical tools have not been discovered to solve many of them.

1.1 Classical Chaos

By the end of nineteenth century, it was realised from the studies on three-body problem that irregular dynamics is an inherent property of systems with complex interactions and can occur even if they are described by deterministic equations of motion. Solar system is an instance of a complex dynamical system consisting of several planets, moons and a sun. One of the important question concerns the stability of the solar system itself. Will the solar system remain stable forever as it is now or will it exhibit irregular behaviour and disintegrate. In the case of solar system the basic interaction is known to be gravitational in nature, but there are complex systems for which the interaction is either not known at all or cannot be written down in closed analytical form. The interactions within the nucleus of an atom are unknown and similar is the case of weather, ecosystems or stock markets. The common ground among these systems is that all of them are expected to behave randomly and are not predictable in general. For instance, in the case of weather system it is known that it cannot be predicted accurately beyond two weeks [1].

Chaos, the topic of study of this thesis, is one manifestation of complexity in any dynamical system. At the heart of unpredictability of such physical systems lies a particular property shared by all of them, namely the sensitivity to initial conditions. At this point some definitions are needed. There are several versions of definitions for chaos and we will follow Devaney's definition here [2]. A chaotic system should (a) be sensitively dependent on initial conditions (b) be topologically transitive and (c) have dense periodic points. A closed interval I denotes all real points y satisfying $p \leq y \leq q$ for some p and q. We consider a dynamical system $f : I \to I$ that maps a closed interval I onto itself. A system exhibits condition (a) if there exist $\delta > 0$ such that, for any point u in the closed interval I and its neighbourhood $\mathcal{N}$ of u, there exists a point v in $\mathcal{N}$ and $n \geq 0$ such that under iteration $|f^n(u) - f^n(v)| > \delta$. Essentially,

a system is sensitively dependent on initial conditions if there is atleast one point in every neighbourhood of u such that under iteration the resulting point separates from the neighbourhood of u. We need one more definition here. An open set S is one with $x \in S$, and $\epsilon > 0$ such that all points r in the open interval $x-\epsilon < r < x+\epsilon$ are contained in S. Topological trasitiveness is present if the system cannot be decomposed into two disjoint open sets that are invariant under iteration of the map. This means that the points under iteration move from any arbitrarily small neighbourhood to another. The system has dense periodic points if arbitrarily close to any point in the closed interval I we can find a periodic point. Thus, the definition of chaos involves three features, namely the unpredictability characterised by sensitive dependence on initial conditions, an element of regularity due to the presence of dense periodic points and nondecomposability in to two disjoint non-interacting systems.

Chirikov provides a practical definition of chaos [3]. In fact, chaos requires stronger form of the condition (a). In chaotic systems, unpredictability is related to strong local instability of motion which manifests itself in *exponential* separation of two trajectories whose initial conditions differ only infinitesimally. According to Chirikov, this is only a necessary condition. The bounded phase space is another requirement. When these conditions are met chaotic dynamics results and this can be taken as a working definition of classical chaos.

We look at some quantitative measures for chaos. The mean rate of separation of trajectories with infinitesimal difference in their initial conditions is characterised by Lyapunov exponents. Again we restrict to Hamiltonian systems. To obtain this quantity, we linearise the equations (1.1) about any reference trajectory $\gamma = (\bar{\mathbf{q}}, \bar{\mathbf{p}})$,

$$\begin{aligned} \frac{d\delta q}{dt} &= \left(\frac{\partial^2 H}{\partial p^2}\right)_\gamma \delta p + \left(\frac{\partial^2 H}{\partial q \partial p}\right)_\gamma \delta q \\ \frac{d\delta p}{dt} &= -\left(\frac{\partial^2 H}{\partial q^2}\right)_\gamma \delta q + \left(\frac{\partial^2 H}{\partial q \partial p}\right)_\gamma \delta p \end{aligned} \tag{1.2}$$

where p and q are N-dimensional phase space variables, δp and δq are the N-dimensional vectors in tangent space. The quantity $d(t) = \sqrt{(\delta p)^2 + (\delta q)^2}$ is the length of tangent vector. Then, maximal Lyapunov exponent Λ is defined as,

$$\Lambda = \lim_{\substack{d(0)\to 0 \\ t\to\infty}} \frac{1}{t} \; ln \; \frac{d(t)}{d(0)} \tag{1.3}$$

Each of the $2N$ directions corresponding to the eigenvectors of the coefficient matrix in eq. (1.2) will experience a stretching and contracting motion, and in principle there will be $2N$ Lyapunov exponents corresponding to each of these directions. But, in practice, Λ will yield the exponent corresponding to the direction of maximum stretching. A positive Lyapunov exponent is indicative of chaos, *i.e* strong exponential separation of two trajectories with closeby initial conditions.

Another point of view of chaotic motion is given by the algorithmic theory of dynamical systems [4] which shows that even under power-law like separation of nearby trajectories prediction becomes possible and only exponential divergence will lead to randomness and hence unpredictability. Thus in chaotic systems unpredictability supersedes classical determinism. However, most generic physical systems in nature, like the many-electron atoms to galaxies, including the coupled oscillator systems we study in this thesis, are mostly not completely chaotic. These are termed mixed systems in which chaotic and regular regions coexist in the phase space.

1.1.1 Classical Phase Space Structure and Dynamics

Since the dynamics is viewed in phase space, the difference between regular and chaotic motion is clearly manifested in the geometric structure of the phase space. An N dimensional Hamiltonian system is completely integrable if it has N integrals of motions $F_1....F_N$ whose Poisson bracket with one another vanish, *i.e* if $F_i, F_j{}_{PB} = 0$, for $i, j = 1, 2...N$. For such a system, the presence of N constants of motion confines the trajectories to lie on some N dimensional manifold in $2N$ dimensional phase space. Liouville-Arnold theorem asserts that the structure of this manifold is that of a N-torus [5]. For a two-dimensional integrable system, the phase space is a 2-torus, a cartesian product of two circles and has the structure of a cycle tube. These are called the invariant tori because any point on the tori is mapped on to itself upon iteration. These tori constitute the foundation for regular and predictable dynamical properties of the integrable systems. Typically a non-integrable system can arise as a perturbation to an integrable Hamiltonian, though it need not always be the case. Perturbation destroys all the constants of motion except the Hamiltonian itself. For weak perturbations, Kolmogrov-Arnold-Moser theorem shows that invariant tori still persist under certain restricted conditions [6]. As perturbation strength increases, the invariant tori are continually destroyed and dynamics makes a transition from regular to predominantly chaotic behaviour.

In general, it is nontrivial to visualise these qualitatively varied types of dynamics in a Hamiltonian system. However, Poincaré section is a technique that allows us to visualise the dynamics in conservative Hamiltonian systems. It is particularly well-suited for two-dimensional systems, like the ones studied in this thesis. The idea is to define a suitable plane in the four dimensional phase space and look at the intersections of the trajectory with this plane. Our Hamiltonian will be of the form,

$$H = p_x^2 + p_y^2 + V(x, y) = E \tag{1.4}$$

where E is the energy. We take a cut through the phase space by fixing say $x = 0$.

Then, the above equation can be rewritten as,

$$p_x = \pm\sqrt{E - p_y^2 - V(0, y)} \tag{1.5}$$

This defines a section (y, p_y) with $x = 0$ and $p_x > 0$. As the system evolves in time, y and p_y are plotted whenever $x = 0$ and $p_x > 0$. If the system is integrable then the invariant tori cuts through the suitably defined section and hence we obtain points which smoothly join to form curves in the Poincaré section. In the absence of tori, *i.e* under conditions of strong chaos, the trajectory is free to wander around anywhere on the energy surface defined by eq. (1.4) and this is reflected as a splatter of points in the Poincaré section. It must be pointed out that studying Poincaré sections is completely equivalent to studying the dynamics in phase space. With the advent of powerful computers Poincaré section is a popular means to identify and visualise the chaotic and regular regions in a system.

This brings us to another popular approach to the study of dynamics, namely through maps. Though not pointed out, the Hamiltonian system defined by differential equations (1.1) is continuous time system. The phase space variables $(\mathbf{p}, \mathbf{q})$ are continuous functions of time and their evolution constitutes a flow. But it is also possible to have dynamical systems defined in terms of difference equations. Maps are such discrete time systems and are of generic form $\mathbf{x}_{n+1} = \mathbf{G}(\mathbf{x_n})$. The Poincaré section described above can also be viewed as a map. Given a point on the section, the Poincaré map obtains the next point on the section. The difference is that for Poincaré maps the time difference between successive points is not the same unlike the case of other maps. Hence study of maps and flows are equivalent methods for understanding the dynamical systems. However maps are computationally and analytically easier to handle. But the use of maps is restricted since the dynamics of most physical systems cannot be reduced to maps. For example, the nonlinearly coupled oscillators serve as models for many physical systems but cannot be written as a map. Since the continuous time systems like these can have immediate experimental consequences it motivates their study inspite of the involved computational and analytical effort required to unravel their dynamics.

1.2 Quantum Chaos

In 1920s quantum mechanics replaced classical mechanics as the fundamental dynamical law of nature. But, the correspondence principle asserts that classical mechanics can still be recovered as a particular limiting case of quantum mechanics. The obvious question arises as to how the classical chaos will manifest itself in the quantum domain. The cornerstone of quantum theory is the uncertainty principle, which forbids precise determination of canonically conjugate dynamical variables like

the position x and momentum p_x simultaneously. Mathematically, it is stated as, $[\hat{x}, \hat{p_x}] = i\hbar$. Quantum theory predicts only the probabilities for a particle's position and momentum. Hence the concept of trajectories is absent in quantum mechanics. The classical definition of chaos in terms of the trajectories can not be carried over to quantum mechanics and it is still an open question as to what constitutes quantum chaos. The prevailing knowledge is that in the semiclassical limit $(\hbar \to 0)$ of quantum mechanics signatures of classical chaos are evident in the statistical properties of the eigenvalues and the eigenfunctions.

In this thesis, we are interested in the quantum dynamics of time-independent model dynamical systems with known nonlinear interactions. We study several coupled oscillator models in this thesis. These models are complex enough to capture the various dynamical nuances of chaos, but simple enough to overcome certain computational difficulties that one would face in studying a more realistic system. For instance, the system of one-electron atom in a magnetic field can be transformed, through a coordinate transformation, to nonlinearly coupled sextic oscillators [7]. Thus qualitative dynamics of coupled oscillators are similar to that of a class of physical problems like atom in static magnetic field etc.

Though there is no acceptable definition for quantum chaos, there is atleast one version that attempts to define quantum chaos in terms that are familiar in classical mechanics. Bohm's formulation [8] incorporates trajectory picture in quantum mechanics through a wavefunction ansatz $\psi = Re^{iS/\hbar}$, where S is the real action function and density $P = R^2$. This transforms the time-dependent Schroedinger equation,

$$i\hbar\frac{\partial\psi}{\partial t} = \left(-\frac{\hbar^2}{2m}\nabla^2 + V(\mathbf{x}, t)\right)\psi \tag{1.6}$$

with external potential V mass m, into a Hamilton-Jacobi like equation,

$$\frac{\partial S}{\partial t} + \frac{(\nabla S)^2}{2m} + V + Q = 0$$

where $Q = -\hbar^2\nabla^2 R/2mR$ is the 'quantum' potential. By identifying $\nabla S/m$ as the velocity of the quantum particle, this approach attempts to define chaos in quantum domain on an equal footing with the classical definition. Thus quantum versions of Lyapunov exponents and KS entropy have been calculated making it possible to have direct comparison with corresponding classical measures. Though such interpretations and measures have been reported in the literature [9] to identify and define quantum chaos, there is still no consensus on this subject. Hence, in this study, the term quantum chaos is used in the conventional sense, *i.e* to denote a quantum system whose classical limit is chaotic.

1.3 Numerical Techniques

As we encounter new phenomena, it becomes necessary to adopt new methods to study them. The study of nonlinear dynamical systems leads us to pursue computational methods in a big way since most of the problems, whether it is diagonalising large matrices or solving coupled differential equations, defy even approximate analytical treatments. We recognise that this trend is not peculiar to nonlinear dynamics but seems to be emerging in other branches of physics too, though nonlinear dynamics has a strong computational component by necessity. Though the motivation to study and understand the dynamics of complex systems had been there since the last one century, in the last few decades, this has attracted much attention mainly because the computational tools to tackle these problems have become available only in recent times. This is one area in which science and technology had to keep pace with one another. Many important milestones in understanding the physics of nonlinear systems were based on computer intensive visualisation or numerical techniques. In fact, the collective effort of numerical analysts and physicists has led to birth of computational physics, as a distinct entity from the conventional theoretical and experimental physics. Ian Percival has said it more eloquently [10], 'We have only been able to reveal a small part of modern dynamics. This part, like many others, has been strongly influenced by electronic computers. Not only do they allow us to calculate what could not be calculated before, but they can present us with moving pictures of dynamical processes, which are a challenge to our understanding. They enable many to share a picture which was at one time the preserve of very few, like Poincaré.'

In this thesis, we have extensively relied upon numerical and visual evidences to extract the physics, which otherwise would have been impossible by the more conventional means. To give a glimpse of the crucial role played visualisation and computation we provide briefly two instances of our improvisation of numerical techniques to facilitate this huge exercise in numerical computation. One of the methods to compute highly excited states of any smooth potential is the basis set diagonalisation of a sufficiently large Hamiltonian matrix. By choosing eigenfunctions of the harmonic oscillator as the basis set, the Hamiltonian matrix will be banded leading to considerable saving on CPU time and storage. In quantum mechanical problems, if the unperturbed part is not harmonic oscillator it may not be beneficial to choose harmonic oscillator basis states since it can lead to poor convergence of eigenvalues. Hence, in general the Hamiltonian matrix is a real symmetric matrix but not banded. This is exactly the scenario in our study of quartic oscillator presented in this thesis. Hence, we numerically banded the Hamiltonian matrix though we were not using harmonic oscillator eigenfunctions for a basis set. Thus the calculation of nearly 2000 excited states would have been impossible without this numerical band-

ing procedure. Secondly, in order to study the classical structures in phase space, we integrate Hamilton's equations of motion. In nonlinear systems, chaos frustrates any attempt to control the accumulation of error for long time integration. This hurdle is overcome to a great extent by using symplectic integrators [11] that exactly conserve the integral invariants. Some of the pictures of Poincaré sections presented in this thesis have been calculated using symplectic methods. Once again, the symplectic integrators are not numerical sophistication for its sake, an but absolute necessity in the presence of chaos.

1.4 Chaos in Physical Systems

At this point, it is worthwhile to dwell on the experimental aspects of quantum chaos and some applications of the studies and undertaken in this thesis. Many atomic and molecular systems provide several examples of multi-dimensional quantum Hamiltonian systems whose underlying classical dynamics exhibits chaos. Atoms in strong magnetic fields have emerged as one of the testing grounds for quantum chaos [12]. In the weak field regime, this is called the normal Zeeman effect and is solved by perturbation methods. But, if the external magnetic field and the Coloumb interaction are of comparable strengths, dynamics becomes chaotic. This is the kind of scenario in white dwarf stars which abound in hydrogen atoms. Indeed, in compact astrophysical objects like white dwarf stars and neutron stars, very high magnetic fields of order 10^2 – $10^9 T$ are present [13]. However, in terrestrial laboratories the atom is excited to a Rydberg state using lasers. Then magnetic field strengths of only few Tesla are needed to achieve the same effect of comparable field and Coloumb interaction. This is one system in which the ideas of quantum chaos can be experimentally verified.

The interaction for hydrogenic atom in strong magnetic field contains a quadratic Zeeman term which makes the problem non-trivial. We confine to a particular magnetic quantum number manifold, say $m = 0$, and assume magnetic field $\mathbf{B}$ to be directed along the z axis. In such a case, the Hamiltonian written in cylindrical coordinates is,

$$H = \frac{1}{2M}(p_\rho^2 + p_z^2) - \frac{e^2}{(\rho^2 + z^2)^{1/2}} + \frac{1}{8}M\omega_c^2\rho^2 \tag{1.7}$$

where the ϕ motion has been separated and $\omega_c = eB/Mc$ is the cyclotron frequency. Rewriting it in semi-parabolic coordinates [12] we get,

$$H = \frac{1}{2}(p_u^2 + p_v^2) - 4\epsilon(u^2 + v^2) + 8u^2v^2(u^2 + v^2) \tag{1.8}$$

where the scaled energy $\epsilon = E\gamma^{-2/3}$ is the parameter and $\gamma = B/B_0$ with $B_0 = 2.35 \times 10^5 T$. It is to be noted that in this form this system resembles the Hamiltonian for a particle in a two-dimensional non-linear potential with ϵ as the parameter. Thus

dynamics of certain nonlinearly coupled oscillators are qualitatively similar to that of an atom placed in a strong magnetic field [12].

Due to rapid technological strides, particularly in lasers and semiconductor technology, the ideas of quantum chaos could now be subjected to experimental tests. Rydberg states of hydrogen atoms interacting with a time varying microwave field has been the subject of active investigation, both theoretically and experimentally. Theoretical studies [14] using an one-dimensional model predicted an increase in quantum ionisation threshold, as a result of localisation, over and above the classical threshold, beyond a critical value of the microwave field. This has been experimentally verified [15]. Numerical investigations on several chaotic quantum systems have shown the existence of eigenstates that display selective enhancements in probability density $|\psi(\mathbf{q})|^2$, called scars, in the vicinity of the unstable classical periodic orbits. In fact, a major part of this work is concerned with the scarred states and their relation to certain classical quantities. The signatures of scars were experimentally observed, using tunnel-current spectroscopy, for a system of electron confined to a semiconductor quantum well in a strong magnetic field [16]. In the last few years, new and interesting experimental possibilities have come up to test the ideas of quantum mechanics and quantum chaos using micron-scale confined structures, popularly known as quantum dots [17]. The electron transport through quantum dots, shows fluctuations in conductance that have universal character determined only by symmetry restrictions. It was suggested that the statistical properties of these fluctuations can be predicted from the chaotic classical scattering dynamics and will provide an experimentally realisable system for studying the quantum manifestations of classical chaos [18]. Following this, the theoretical studies of universal conductance fluctuations have linked them with universality in certain properties of random matrices and quantum manifestations of classical chaos. In the last decade several of these laboratory experiments were performed to understand them from the point of view of quantum chaos [19].

1.5 Quantisation

Quantisation procedure involves solving the time-independent Schroedinger equation with potential $V(\mathbf{x})$,

$$\left(-\frac{\hbar^2}{2m}\bigtriangledown^2 + V(\mathbf{x})\right)\psi(\mathbf{x}) = E\psi(\mathbf{x}) \tag{1.9}$$

to obtain eigenvalues E_n and eigenfunctions $\psi_n(q)$. We will not go into the different kinds of eigenvalue spectra and the requirements on eigenfunctions. In this study throughout we will deal with discrete eigenvalue spectra and normalisable eigenfunctions. The eigenvalues and eigenfunctions provide all the information about a quan-

tum system. In the study of quantum chaos, this information is used to learn about the quantum dynamics, quantum signatures of classical chaos and other quantum effects like localisation etc. Another interesting question is the semiclassical behaviour, in the limit of very highly excited states or $\hbar \to 0$, of the chaotic quantum systems. There exist a few prescriptions to construct a quantum Hamiltonian corresponding to a given classical system, and similarly for the for the inverse problem; to associate, in the limit $\hbar \to 0$, a classical function to a given quantum operator. Wigner-Weyl transform [20] of any operator $\hat{A}$ is,

$$A_w(\mathbf{q},\mathbf{p}) \equiv \int d\mathbf{y} < \mathbf{q}+\mathbf{y}/2|\hat{A}|\mathbf{q}-\mathbf{y}/2 > \exp(-i\mathbf{p}.\mathbf{y}/\hbar) \tag{1.10}$$

is one of the widely used approaches. The inverse of this transform is also well defined. One of the earliest semiclassical quantisation procedures is the familiar WKB method for one-dimensional systems involving wavefunction ansatz,

$$\psi(q) = A(q)e^{iS(q)/\hbar} \tag{1.11}$$

in which the function $S(q)$ is expanded in powers of $\hbar$. The WKB method and its multidimensional counterpart, EBK method are valid only for integrable systems or for those that have invariant structures in phase space. They essentially express the classical action along any independent circuit in multiples of Planck's constant h. Towards understanding classically nonintegrable quantum systems the first question was posed by Einstein; how to quantise a system that has no invariant tori in phase space ?. After several decades of neglect, this question was answered by the periodic orbit theory, mainly the work of Gutzwiller, Balian and Bloch and others [21, 22, 23].

1.5.1 Study of Eigenvalue Spectrum

Where does one look for quantum chaos? Percival [24] has suggested that the quantum spectrum associated with the regular and irregular regimes will be qualitatively different. Thus, the information about the underlying chaotic classical dynamics can be found, if at all, in the eigenvalues and the eigenfunctions of the quantum system. Since then considerable progress has been made in understanding the individual eigenvalues through its relation to the classical periodic orbits and also their collective statistical behaviour. We will look at both of them in little more detail. For a particle in a potential $V(q)$ satisfying the Schroedinger equation $\hat{H}\psi_n(q) = E_n\psi_n(q)$, the density of states is given by the trace of the spectral operator,

$$d(E) = \text{Tr}\ \ \delta(\hat{H} - E_n) = \sum_n \delta(E - E_n) \approx \bar{d}(E) + d_{osc}(E)$$

where $\bar{d}(E)$ is the average contribution obtained from the semiclassical rule for a N dimensional system that each quantum state at energy E is associated with a

phase space volume $(2\pi\hbar)^N$ and $d_{osc}(E)$ represents the fluctuations about the average. The Laplace transform of the quantum propogator in position representation $< x_2|e^{iHt/\hbar}|x_1 >$, gives the Green's function which is related to the density of states by the relation,

$$d(E) = -(1/\pi)\ \text{Im Tr}\ \hat{G}(E)$$

Essentially, the periodic orbit theory of Gutzwiller applies the semiclassical approximation to the trace of the Greens function as a sum over all the classical periodic orbits to obtain the oscillatory part of the density of states $d_{osc}(E)$ [21]. The periodic orbit theory is significant because it is one of the few general theoretical results that links classical and quantum mechanics when the classical dynamics is chaotic. It provides a framework to semiclassically estimate the eigenvalues of a chaotic system.

1.5.2 Random Matrix Theory

For a quantum system with complex unknown interactions, like the nucleus, the energy spectrum can be quite complicated since the density of states typically increases with energy. Hence, in the regions of highly excited states most of the good quantum numbers lose their meaning except spin and parity. As in the case of classical statistical mechanics, where we resorted to ensemble averages in the face of having to contend with 10^{23} equations of motion, here again we confront a similar situation where it is impossible to study all the details of the individual energy levels. So we resort to statistical methods to study the collective properties of energy levels, giving up the detailed knowledge of the individual levels. The most well studied quantity in this statistical theory is the distribution of eigenvalue spacings, $s = E_{n+1} - E_n$.

However, the challenging aspect of the statistical theory of energy levels is their connection with another branch of mathematics, the random matrix theory (RMT). Random matrices are those for which the matrix elements are random variables derived from some distribution. Wigner pioneered its application to nuclear physics with the conjecture that the local statistical behaviour of levels in a sequence with same spin and parity is identical with the eigenvalues of a random matrix. Later on, the exact results for eigenvalue spacing distribution and other statistical measures were derived rigorously by Mehta, Dyson and others [25]. Since the work Bohigas et. al. [26] it is now well-known that the eigenvalue spacing distribution $P(s)$ for the classically chaotic time-reversal symmetric system is same as that for the familiar Gaussian Orthogonal Ensemble (GOE) given by,

$$P(s) = \frac{\pi s}{2}\ \exp\left(\frac{-s^2\pi}{4}\right) \tag{1.12}$$

The level spacing distribution for systems without time-reversal symmetry, modelled

by Gaussian Unitary Ensemble, is given by,

$$P(s) = \frac{32s^2}{\pi^2} \exp\left(\frac{-4s^2}{\pi}\right) \tag{1.13}$$

For quarternion real Hamiltonian matrices, the appropriate ensemble is the Gaussian Symplectic Ensemble (GSE). In the last one decade, many classically chaotic systems were subjected to numerical tests for their eigenvalue spacing distributions and the appropriateness of the random matrix model for these distributions has been amply verified [59]. In fact, there is some consensus that the universal nature of eigenvalue spacing distribution is a signature of quantum chaos. But, there are still some crucial unanswered questions: Random matrix theory is a statistical theory and holds good for systems with large number of degrees of freedom. But even two degree of freedom systems we deal in quantum chaos also exhibit good agreement with RMT predictions. Secondly, the relationship between quantum chaos and random matrix ensembles is yet to be rigorously established.

The eigenvalues of chaotic systems have been sufficiently analysed and understood, but this constitutes only half the story. Comparatively, the eigenfunctions of chaotic systems are still largely unexplored. This is so because eigenvalues are easy to compute and handle but reliable computation of highly excited eigenfunctions is an onerous task. Verification of theories on eigenfunctions are not straightforward, because theoretical studies have no prediction for individual eigenfunctions. In this thesis, the focus is on the structure and morphology of eigenfunctions, localised states and their connection with periodic orbits. We will also outline some efficient numerical and visual techniques to study the eigenfunction structures.

1.6 Eigenfunctions and Its Structures

The first attempt towards understanding the structure of wavefunctions was made by Berry in late 70s [27]. The principal question is whether the underlying chaotic dynamics is manifested in the eigenfunctions and what is its structure under conditions of strong classical chaos. To answer this question we need to invoke the semiclassical wavefunction, which is the work of Maslov, VanVleck, Keller and others [28]. The basic idea is to associate a wavefunction $< \mathbf{q}|\psi >$ with a N dimensional surface in $2N$ dimensional classical phase space such that the semiclassical evolution of $< \mathbf{q}|\psi(t) >$ corresponds to the evolution of the N dimensional surface. Berry and Voros [29] use the semiclassical wavefunction,

$$\psi_I(\mathbf{q}) = \mid \det \frac{\partial^2 S(\mathbf{q},\mathbf{I})}{\partial \mathbf{q}\, \partial \mathbf{I}} \mid^{1/2} \exp(\frac{i}{\hbar} S(\mathbf{q},\mathbf{I}))$$

where $S(\mathbf{q},\mathbf{I})$ is the action function associated with the single-valued surface and it satisfies the classical Hamilton-Jacobi equation. Using a similar semiclassical wave-

function and its Wigner function as the principal tool they make conjectures about the nature of eigenstates in the semiclassical regime. This is now refered to as the semiclassical eigenfunction hypothesis. Wigner function [30] is a quasi-probability distribution in phase space variables and is useful in studying quantum-classical correspondence. Essentially, it is the Weyl transform of the density operator $\hat{D} = |\psi >< \psi|$. According to this hypothesis, the Wigner function of a semiclassical eigenstate will be concentrated on the region explored by a typical orbit over infinite times. For a chaotic system, this implies that the Wigner function will reduce to a microcanonical ensemble on the energy shell, whereas for integrable systems it will be concentrated on the invariant tori. This line of argument indicates that the classical invariant regions, like the tori or energy shell, are responsible for the structures in eigenfunctions and the unstable periodic orbits that form a set of measure zero in chaotic systems can have no influence on them. Even intuitively the enhanced structures in eigenfunction over and above the average were not expected, since for classically chaotic systems all periodic orbits are either unstable or neutral, and a wave packet constructed to be centered on such a trajectory, would be expected to spread out fast. The combination of Berry-Voros hypothesis, which drew support from an earlier work of Shnirelmann [31], and such intuitive arguments led to the understanding that all the eigenfunctions of chaotic systems would be structureless and Gaussian random in nature.

1.6.1 Scars of Classical Orbits

Later numerical computations showed that this view of semiclassical eigenfunctions is incomplete. The first evidence in the form of visual images of the probability density, modulus squared of the wavefunction $|\psi(\mathbf{q})|^2$, came from the studies on the dynamics of a smooth sphere in a stadium shaped billiards. Many eigenfunctions in this system clearly showed enhancements in probability density selectively in certain regions coinciding with the vicinity of the underlying periodic orbits. We have accurately computed nearly 2000 eigenstates for nonlinearly coupled oscillator models and many of them flagrantly violate Berry-Voros hypothesis and a study of these eigenstates constitutes the core of this thesis. The lesson from the numerical computation is that most of the quantum eigenfunctions are not simply structureless but exhibit a rich variety of structures in the form of density enhancements that are distinguishable from the background. At this point, it would not be out of place to recognise, as we said earlier, that numerical and visual techniques have played a pivotal role in this important breakthrough that led to subsequent theoretical investigations.

Central to Berry-Voros hypothesis is the assumption that isolated periodic orbits have no influence on the eigenfunctions. But the theoretical arguments of Heller

places the entire burden of the density enhancements (*scars*) on the isolated periodic orbits [32]. A scarred eigenstate is one whose probability density near a periodic orbit differs significantly from the statistically expected density based on Berry's conjecture of gaussian random eigenfunctions. Physically this implies that the particle is more likely to be found in the scarred regions than in the rest of the classically allowed phase space. By propagating Gaussian wavepackets $\phi(t)$ along the classical periodic orbit of time period T and Lyapunov exponent λ, it can be shown that the spectral intensity, defined as the Fourier transform of the correlation function,

$$S_T(\omega) = \int_{-T}^{T} e^{i\omega t} < \phi(0)|\phi(t) >$$

represents the strength of overlap between the Gaussian wavepacket and the eigenstate, $| < \Psi_E|\phi > |^2$. The spectral intensity $S_T(E)$ reveals a band structure with frequency $\omega = 2\pi/T$ indicating that some eigenstates show enhanced overlap with the Gaussian wavepacket propagated along the periodic orbit. In this case the band strength enhancement is by a factor ω/λ in comparison with the statistically expected estimate based on Gaussian random eigenstate postulated by the semiclassical eigenfunction hypothesis. This argument provides the basis for the occurance of scars and associates them with the least unstable isolated classical periodic orbits. Later, scars were studied from different points of view, though the essential qualitative conclusions remain the same. In the general analytical framework of scarring as developed by Berry, the spectral Wigner function averaged over a small energy scale is shown to be influenced by isolated periodic orbits semiclassically [33]. The stability of the periodic orbits is shown to affect the scar weight and scar amplitude significantly. In the later chapters, our numerical computation on eigenstates will be interpreted in the light of Berry's scar formula. Bogomolny's approach [34], based on Gutzwiller's periodic orbit theory, shows that periodic orbits will manifest as scars in a group of eigenfunctions averaged over a small energy interval though it does not predict anything about the individual eigenfunctions. Whatever the theory the lesson is that, chaos notwithstanding, the scars are here to stay. In fact, far from being only a computational artifact these scarred states, like the 'bouncing ball' states discovered in the stadium billiards problem were actually observed in a rectangular microwave cavity with a circular disc inside it [35].

1.7 Localisation

Scars indicate that the movement of the quantum particle inside the potential is quite restricted; it does not access the whole of the classically available phase space but for most of the time is confined to certain subregions. This is in sharp contrast with the

behaviour of a classical chaotic system that explores almost the entire phase space in course of its evolution. This brings to fore another unique feature of quantum mechanics, namely the localisation. It is a generic phenomena in many branches of physics. The most well-known is the Anderson localisation in condensed matter physics for the motion of a charged particle in the presence of potential wells of random depths [37]. In this case it was rigorously shown that due to quantum interference effects the envelope of all the eigenstates are typically exponentially localised, $|\Psi(\mathbf{r})| \sim e^{-(|\mathbf{r}-\mathbf{r}_0|/l)}$, where l is the localisation length.

'Localisation' has been used to denote phenomena in a wide class of problems, and there is probably no consensus on what exactly this term means [36]. It comes in several varieties. Apart from Anderson-type localisation, there is perturbative localisation [38], dynamical localisation [39], scarring localisation [40] and a bewildering array of mechanisms to go with them. All the scarred states are in some sense localised. But, in this study of chaotic quantum systems the term localisation is reserved for very special kind of scarred states that show exceptional decoupling from a large part of the phase space and is mostly associated with simple periodic orbits of short time period. The localisation phenomena, in the context of quantum chaos, still continues to occupy the centre stage because it is fraught with theoretical challenges and experimental possibilities [41]. For instance, a comprehensive theory encompassing all the nuances of localisation in quantum mechanics still remains an open problem. We will now outline two theoretical and experimental attempts that uncover the mechanism of localisation that lurks behind chaos.

1.7.1 Models for Localisation

In many fields, simple models continue to be the guiding spirit for further understanding. The classical Taylor-Chirikov standard map [42],

$$P_{t+1} = P_t + KSin\theta_t \qquad \theta_{t+1} = \theta_t + P_{t+1} \qquad (mod\ \ 2\ \pi)$$

with one classical parameter K, plays such a role in quantum chaos. For the kicked systems the perturbing potential is in the form of delta kicks and comes in to play only once every time period. In the classical kicked rotor, a physical version of the standard map, the evolution of $< P^2 >$ is of a diffusive nature, leading to average energy growing linearly with time. The quantum kicked rotor, however, suppresses the classical diffusion in P^2 beyond a particular time, leading to localisation in momentum space. The work of Grempel *et. al.* [43] led to theoretical understanding of this phenomena. They showed that the quantum kicked rotor and the Anderson's tight binding model are equivalent and that the destructive quantum phase interference is the mechanism that is responsible for localisation in both the cases. The crucial

difference is that the potential for the kicked rotor is *not* random, whereas randomness is the basic ingredient for the Anderson's model. This kind of situation is termed dynamic localisation to emphasise that randomness arises from the dynamics rather than from the potential.

The significance of dynamical localisation stems from its generality. The contention was that it is not particular to the kicked rotor but a general phenomena that will suppress any quantum diffusion. This claim was tested for the case of photoelectric effect from the highly excited hydrogen atoms due to interaction with the microwave field. Theoretical studies with the one-dimensional model,

$$H = \frac{p_z^2}{2} - \frac{1}{|z|} + \epsilon z \cos(\omega t)$$

where ω is the microwave field frequency and ϵ is a parameter, showed that quantum diffusion is indeed suppressed leading to exponential-like localisation. Following this theoretical prediction, experiment was performed using short-pulse microwaves to ionise the highly excited hydrogen atoms. The predictions based on localisation effects was upheld by the results of the experiments [15].

1.7.2 Localisation in Nonlinear Oscillators

While dynamical localisation is attributed to quantum interference effects, it does not explain the origin of localisation in many classically chaotic quantum systems. The two-dimensional nonlinearly coupled oscillators form one such broad class of time-independent Hamiltonian systems that reveal striking and rich localisation properties. In fact, most of the studies on localisation have focussed on the kicked systems that could be reduced to maps. The scar theories outlined above have not yet been conclusively verified since, as explained earlier, it is a nontrivial task and also very few computational results exist for the very highly excited states of smooth Hamiltonian systems. This thesis is an attempt to fill this gap. We have done an indepth study of the eigenfunction structures and the localisation properties in two and three dimensional coupled oscillators. In the process we computed eigenfunctions lying as high as 2500 states above the ground state. The data generated is enormous and naturally presents itself as a quintessential visualisation problem. To extract physics out of this large body of numbers, we have relied upon evidences from the numerical and visual techniques. In the next few paragraphs we give a glimpse of some of the essential results and indicate where it fits in the progress towards understanding the eigenfunctions of chaotic systems.

It is instructive at this point to specify the potential for which the results in this thesis have been obtained. Four different potentials that have drawn our attention are : (a) $V_1(x,y) = x^4 + y^4 + \alpha x^2 y^2$, (b) $V_2(x,y) = x^2 + y^2 + \beta x^2 y^2$, (c) $V_3(x,y) = x^4 + y^4 +$

$z^4 + \alpha_1 x^2y^2 + \alpha_2 y^2z^2 + \alpha_3 x^2z^2$ and (d) $V_4(x, y) = x^6 + y^6 + z^6 + \beta_1 x^2y^2z^2$. A brief account of the classical dynamics of the above potentials is given at appropriate places in the thesis . All these potentials share certain common properties. All of them are mixed systems, that is chaos and regular regions coexist for almost all the parameter values. They are all bounded for all positive values of the parameters, which means that quantum mechanical spectrum is discrete. Except (b), others are homogeneous systems, implying that the dynamics at two different energies can be related by a simple scaling factor.

All these potentials are characterised by the existence of a channel. A particle trapped in a motion along the channel, executing oscillations with the time period of the underlying classical periodic orbit, will be confined to the periodic channel motion for a very long time. This is a simplistic physical picture of quantum localisation in terms of the classical motion. To be more concrete, we presently confine to oscillator systems given by the potentials (a) and (b) above. As scar theories assert, the channel periodic orbit in these systems strongly scars a series of quantum states even as far as 2500 states above the ground state we have computed. We expect that they will even survive up to the classical limit ($\hbar \to 0$). Thus, in the context of the nonlinear coupled oscillators, the term 'localisation' is used to denote states scarred by the channel periodic orbit in the sense mentioned above. We will simply call them as localised states, unless otherwise specified. These class of localised states are special in many ways. Firstly, these are effectively one-dimensional states and so semiclassical WKB-like formula can be obtained to estimate their energies. Apart from visually recognising them, we have also proposed numerical methods to identify these class of states. We have shown that information entropy of quantum states will unambiguously identify these class of states. Thirdly, the numerical evidence unequivocally suggests that these states are dominated by peaks whose falloff is exponential in the space of the eigenfunctions of the corresponding unperturbed systems, that is when $\alpha = \beta = 0$. This is the first observation of exponential localisation in a smooth Hamiltonian system. All these three features are discussed in detail in later chapters 4.

The simple periodic orbit responsible for confining the particle to channel motion can be either stable or unstable, *i.e* an orbit in the neighbourhood will either stay in the neighbourhood of the periodic orbit or move away from it. In the case of potentials in (a) and (b), the channel periodic orbit oscillates in stability as a function of the respective parameter, α and β in this case. Whenever the orbit crosses over from stable to unstable regime, or vice versa, the orbit bifurcates in to two new orbits or two orbits disappear at a point. We numerically showed that the Poincaré section of the homogeneous two-dimensional single parameter Hamiltonian systems scales with the parameter under certain conditions. The scaling exponents are dependent only

on the degree of homogeneity of the potential. More details of parametric local scaling is given in chapter 2.

Does the stability of the underlying orbit have any effect on the localised states? We numerically demonstrated that the exponential localisation is best at certain points in parameter space at which the channel orbit loses stability and gives birth to two new orbits. We also showed that the stability of the channel orbit is intimately correlated with the degree of localisation as measured by the information entropy. In this process we could verify that even the gross measures of localisation like the information entropy can distinguish subtle differences in the degree of localisation between two localised states. We appeal to the theories of Berry and Heller. Both these theories predict that scar enhancement is a function of the stability of the orbit. But quantitative agreement is ruled out for various reasons. We interpret our results in chapter 4 in the light of the scar formula, due to Berry.

Three dimensional systems form the core of chapter 5. Classically in three dimensional nonintegrable systems the trajectories can leak out of the gaps in tori to the other regions of energy shell. This is called Arnold diffusion [44], The motivation to study a three dimensional system is to look for signatures of Arnold diffusion in quantum eigenstates. But, in this study of three dimensional systems, we have studied the random matrix like behaviour of the eigenvalue spacing distribution. The three dimensional system exhibits a rich hierarchy of localised states than those observed for the two-dimensional system and promises much more interesting dynamical properties.

Parametric Scaling in Nonlinear Oscillators

Classical periodic orbits play a crucial role in both semiclassical and quantum mechanics, as pointed out in the introduction. For instance, it is known that periodic orbits are responsible for enhanced structures in the eigenfunctions. Though chaotic systems possess infinite periodic orbits, the most influential ones are those with short time period. They play a significant role in Gutzwiller's prescription for semiclassical quantisation of chaotic systems and in zeta-function approaches in classical and semiclassical mechanics [45]. In this chapter, we will discuss some scaling properties associated with simple periodic orbits, with short time period, in Poincaré sections for a class of homogeneous two-dimensional nonlinear oscillators of the form $H(\mathbf{q},\mathbf{p}) = p_x^2 + p_y^2 + V(x,y;\alpha)$, where α is a parameter, and with particular reference to the coupled quartic oscillator.

2.1 Parametric Scaling

One well-known property of homogeneous Hamiltonian systems is that their dynamics scales with energy [46]. If at energy E_0 there is a trajectory given by $(\mathbf{q_0},\mathbf{p_0})$, then at some other energy E there exists a similar trajectory $(\mathbf{q},\mathbf{p})$ and this can be obtained from the former by,

$$\mathbf{p}(t') = \left(\frac{E}{E_0}\right)^{(1/2)} \mathbf{p}_0(t) \qquad \mathbf{p}(t') = \left(\frac{E}{E_0}\right)^{(1/2)} \mathbf{p}_0(t)$$

$$t' = \left(\frac{E}{E_0}\right)^{(1/4)} \tag{2.1}$$

Thus, in case of homogeneous systems, it is sufficient to study the classical dynamics at one particular energy since dynamics at any other energy can be obtained by simple scaling as shown above. Scaling has other implications too. In general Hamiltonian systems, the orbits form one parameter families with energy being the parameter [47]. But in homogeneous Hamiltonian systems varying of energy simply scales the orbits without changing the orbit structure in the phase space, that is bifurcations and related phenomena cannot occur as a function of energy, in general. Hence we have to change the parameter associated with the Hamiltonian to study the changes in the orbit structure and thus the term parametric scaling denotes scaling of classical quantities with parameter variation.

Most studies on Hamiltonian systems have focussed on single parameter systems, which controls the onset of chaos in the system. Such a Hamiltonian system could

be integrable for more than one value of the parameter. As the parameter value moves away from last of these integrable values, the invariant tori will be continually destroyed and replaced by chaotic trajectories. Yet, as the predominant part of phase space is becoming increasingly chaotic, upon variation of the parameter, there could be periodic orbits that might alternate between stability and instability. This leads to regions of phase space in which secondary tori are born, eventhough rest of the phase space may be completely chaotic. This scenario is visually described using Poincaré sections at the end of this chapter. We will consider two classes of Hamiltonians which will exhibit the kind of behaviour outlined above. First of these, we call the class I, is given by,

$$H_{2n} = \frac{1}{2}p_1^2 + \frac{1}{2}p_2^2 + \frac{1}{2n}(\beta_1 q_1^{2n} + \beta_2 q_2^{2n}) + \frac{\alpha}{2}(q_1^2 q_2^{2n-2} + q_2^2 q_1^{2n-2}), \tag{2.2}$$

where the parameters β_1, β_2, $\alpha > 0$. For a fixed value of β_1 and β_2, the system makes a transition from regular to predominantly chaotic behaviour as a function α.

To get a concrete picture of the idea, we consider the well-studied model of nonlinearly coupled quartic oscillator [48, 40], with Hamiltonian given by,

$$H_4 = \frac{1}{2}p_1^2 + \frac{1}{2}p_2^2 + \frac{1}{4}\beta_1 q_1^4 + \frac{1}{4}\beta_2 q_2^4 + \frac{1}{2}\alpha q_1^2 q_2^2, \tag{2.3}$$

where $\alpha > 0$ is the chaos parameter at fixed positive values of β_1 and β_2. Note that this Hamiltonian is a special case of eq. (2.2) for $n = 2$. In fig. (2.1), the contour plot of the potential for coupled quartic oscillator in eq. (2.3) is shown. This system is integrable

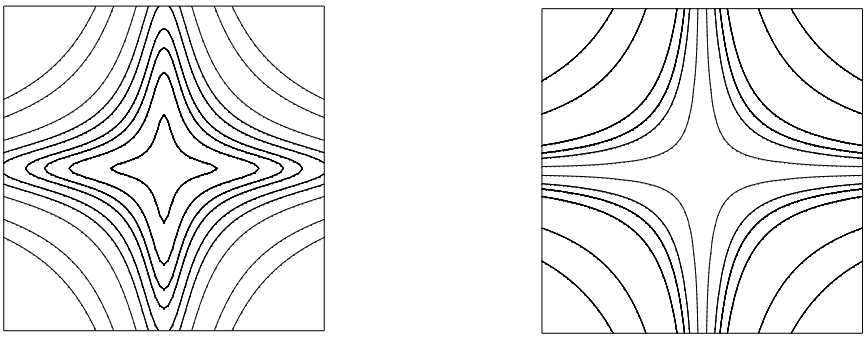

Figure 2.1: *Contours of coupled quartic oscillator potential for (a)* $\alpha = 90$ *and for (b)* $\alpha = \infty$*. The axes are* x *and* y*.*

for $\alpha = 0, 1, 3$ and becomes increasingly chaotic for larger values of the parameter. More details on the classical dynamics of the quartic oscillator is presented later in this chapter.

Although there are infinite periodic orbits in the chaotic regime of this system, the object of further interest is the periodic orbit given by the initial condition $(x, y =$

$0, p_x, p_y = 0)$, the straightline orbit, to be referred as the channel periodic orbit since its trajectory coincides with the x-axis lying along the channel of the potential. This channel orbit is plays a crucial role in the semiclassics and quantum mechanics of the oscillator; as we will see later they scar a series of states in the quantum spectrum. It has has short time-period and interesting stability properties. Its time period is given by,

$$T(E) = E^{-1/4}\sqrt{\pi}\ \ \frac{\Gamma(1/4)}{2\ \ \Gamma(3/4)} \tag{2.4}$$

To determine the stability of the channel orbit, the Hamilton's equations of motion for the coupled quartic oscillator in eq. (2.3) are linearised as indicated in chapter 1 and is represented in a matrix form, $\delta\dot{\mathbf{z}} = J\ (\alpha)\delta\mathbf{z}$, where $\mathbf{z} = (\mathbf{q}, \mathbf{p})$. This matrix equation is integrated for one time period of the periodic orbit, in which case the matrix J is called the monodromy matrix. The trace of the monodromy matrix is indicative of the stability of the periodic orbit. For conservative two-dimensional Hamiltonians, the orbits are stable if $\mid$ Tr $J(\alpha)\ \mid < 2$ and are unstable if $\mid$ Tr $J(\alpha)\ \mid > 2$ [44]. The fig. 2.2 shows the oscillating stability of the channel orbit in the positive α range. The channel orbit corresponds to positive α range and the diagonal orbit to negative α values, and as we shall see a transformation exists between them. In general, it is

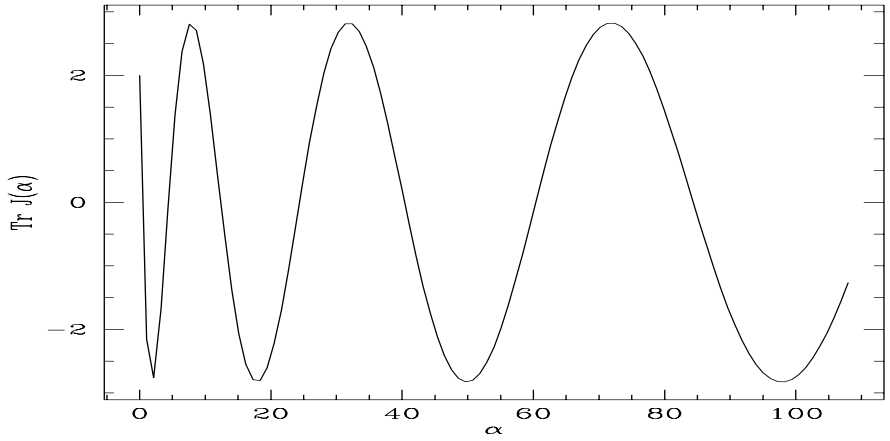

Figure 2.2: *The stability of the channel of coupled quartic oscillator as a function of the parameter* α.

not possible always to determine Tr $J(\alpha)$ analytically for any arbitrary periodic orbit. However, for this simple channel periodic orbit of the coupled quartic oscillator the analytical expression for Tr $J(\alpha)$, due to Yoshida [49], is given by,

$$\text{Tr } J(\alpha) = 2\sqrt{2}\cos\left(\frac{\pi}{4}\sqrt{1 + 8\frac{\alpha}{\beta_1}}\right), \tag{2.5}$$

where $J(\alpha)$ is the monodromy matrix for the *half* Poincaré map of the oscillator [50]. Due to reflection symmetries present in the oscillator in eq. (2.3), given a section

of an orbit, its reflected version about any of the x or y axes is also a section of another orbit. As pointed out in chapter 1, the usual Poincaré map is chosen, say, with condition, $(x = 0, y, p_x > 0, p_y)$. However, taking into account these symmetries we define half Poincaré map with the condition $(x = 0, y, \pm p_x, p_y)$, and this has all the properties of the conventional Poincaré maps. As an aside we note that, in the context of a hydrogenic electron in a uniform field given by eq. (1.7), experiments give a peak in the Fourier transform of the absorption spectrum for every orbit closed in (ρ, z) space which start and end at the nucleus. If this system written in semiparabolic coordinates as in eq. (1.8), then for every such orbit with return time τ in (ρ, z) space, there is a periodic orbit in the space of semiparabolic coordinates that passes through the origin with time period $T = 2\tau$. The signal associated with such periodic orbits appear at $T/2$ and are related to properties of one-half cycle of the periodic orbit.

The analytical result eq. (2.5) exactly reproduces the numerically calculated stability curve in fig. 2.2. By inverting this formula using the stability conditions mentioned above, we find that at values of $\alpha = \beta_1 n(2n+1)$, where n is an integer, the channel orbit changes stability through a pitchfork bifurcation, since at these α values Tr $J(\alpha) = \pm 2$. Pitchfork bifurcation of the channel orbit leads to the birth of two new orbits of the same time period and stability while the channel orbit itself changes stability. It is useful to note that the Hamiltonian bifurcation theory applied to two-dimensional conservative systems, admits five and only five types of bifurcations [50].

The windows of stable regimes of the channel orbit, which occurs as a function of α, manifests itself in the form of stable islands in the vicinity of the fixed point $(q_2 = 0, p_2 = 0)$ corresponding to the channel orbit in the half-Poincaré map of the coupled quartic oscillator. Significantly, at the values of α at which the stability is the same and the slope dTr $(J(\alpha))/\mathrm{d}\alpha$ has the same sign the stable islands have the same structure, though due to increasing chaos in the rest of the phase space the area of the stable region shrinks with increase in α. For example, in fig. 2.3 shows two such sections in the vicinity of the channel orbit at two different α values at which the channel orbit is just about to lose stability through a pitchfork bifurcation, i.e Tr$J(\alpha) = 2$ and slope is positive. The figure clearly shows that though the area of stability is shrinking, the island structure in the section around the channel orbit is similar. This is indicative of possible scaling.

Following this lead, we look for scaling behaviour as follows. As the fig. 2.3 shows, the fixed point of the channel orbit is surrounded by fixed points of the period eight orbit lying close to the boundary of the stability region beyond which the chaotic sea takes over. Let the period eight orbit's intersection with the positive q_2 axes be at $d_1(\alpha)$ and with the positive p_2 axes be at $d_2(\alpha)$. The distances $d_1(\alpha)$ and $d_2(\alpha)$ were measured from the Poincaré sections. The figure below shows the $\log(\alpha)$ plotted against the

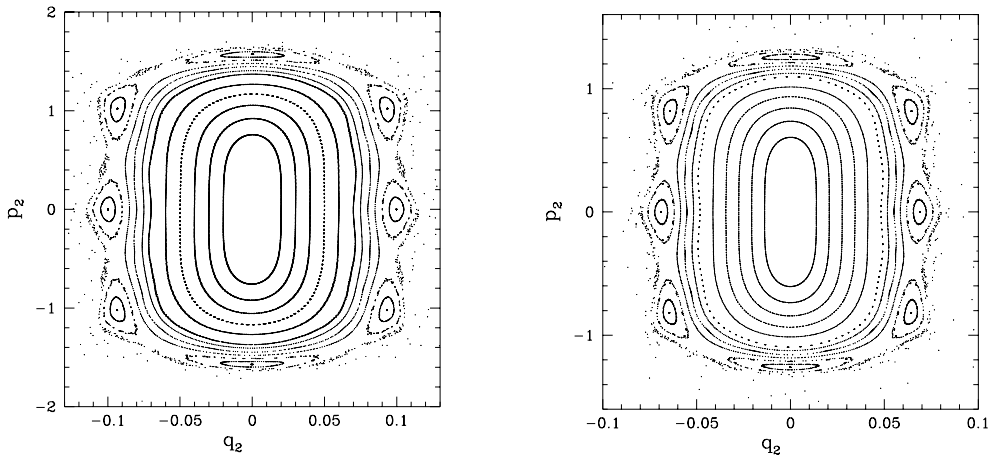

Figure 2.3: *Poincaré map of the coupled quartic oscillator potential in the vicinity of the channel orbit for (a)* $\alpha = 66$ *and (b)* $\alpha = 120$.

distances $log(d_{1,2}(\alpha))$ and the straightline obtained implies scaling of these distances with α, i.e., $d_1(\alpha) \sim \alpha^{-\gamma_1}$, and $d_2(\alpha) \sim \alpha^{-\gamma_2}$. γ_1 and γ_2 are slopes of the straight lines and will the scaling exponents. The lines shown are those of best fit. Their slopes γ_1 and γ_2 are equal to -0.621 and -0.372 respectively. This numerical experiment was repeated for the coupled quartic oscillator with $\beta_1 = 0.5$ and the slopes γ_1 and γ_2 are found to be independent of β_1. This is also borne out from the fig. 2.4(a) shown below.

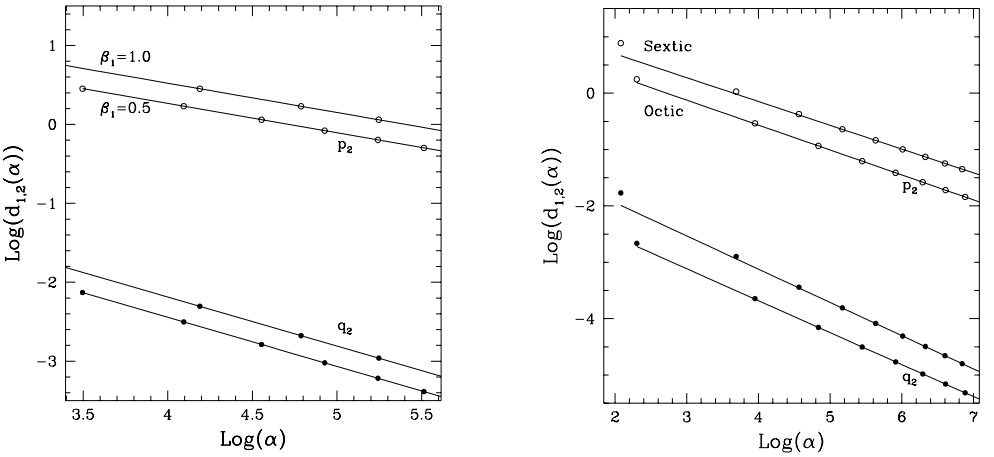

Figure 2.4: *The scaling of the distances for (a) the coupled quartic oscillator system, (b) The sextic and octic oscillators.*

2.2 Scaling of Poincaré Maps

The principal results [51] of this section are based on the numerical evidence presented above. Let

$$q_2' = f(q_2, p_2; \alpha) \qquad\qquad p_2' = g(q_2, p_2; \alpha) \tag{2.6}$$

be the half-Poincaré map, with $\alpha' > \alpha$. Due to the reflection symmetries in the oscillator, $f(q_2, p_2; \alpha) = -f(-q_2, -p_2; \alpha)$, and similarly $g(q_2, p_2; \alpha) = -g(-q_2, -p_2; \alpha)$. Since the Poincaré section scales, the above functions also will scale as follows,

$$\begin{aligned}
(\frac{\alpha'}{\alpha})^{-\gamma_1} f(q_2, p_2; \alpha) &= f((\frac{\alpha'}{\alpha})^{-\gamma_1} q_2, (\frac{\alpha'}{\alpha})^{-\gamma_2} p_2; \alpha'). \\
(\frac{\alpha'}{\alpha})^{-\gamma_2} g(q_2, p_2; \alpha) &= f((\frac{\alpha'}{\alpha})^{-\gamma_1} q_2, (\frac{\alpha'}{\alpha})^{-\gamma_2} p_2; \alpha').
\end{aligned} \tag{2.7}$$

where γ_1 and γ_2 are scaling exponents with values -0.625 and -0.325 respectively for coupled quartic oscillator of both kinds ($\beta_1 = 1.0, 0.5$ for n=2 in eq. 2.2) as demonstrated above.

However this scaling relation is more general in nature. It covers all the two-dimensional homogeneous Hamiltonian systems whose Poincaré sections around channel orbits scale with the parameter α. We performed a similar numerical exercise for the coupled sextic and octic oscillators, corresponding to $n = 3$ and $n = 4$ of the general Hamiltonian in eq. (2.2). The fig. 2.4(b) shows that the scaling still holds good and the slopes γ_1 and γ_2 for the sextic are -0.589 and -0.422, while for the octic potential they are -0.566 and -0.442. We also verified the scaling in coupled oscillators up to $n = 7$ of the class I Hamiltonians.

Based on the numerical evidence presented above, the following conjecture is made for the scaling exponents [51]: The scaling exponents, for class I Hamiltonians in eq. (2.2) is given by,

$$\gamma_1 = \frac{2n+1}{4n} \quad \gamma_2 = \frac{2n-1}{4n}. \tag{2.8}$$

such that the area of stability goes as α^{-1}. Note that the scaling exponents depend only on the degree of homogeneity of the potential. The validity of the above scaling relationships are restricted to a certain region around the periodic orbit, in this case around the origin of the section. The scaling is in this sense only local. We have observed that the area of stability may be safely taken as the region in which the scaling holds, although this can be a serious underestimation, as we will now see. The exponents found from the above can be used to directly verify the scaling of the half first return maps as given by the eq. (2.7). In the case of the Hamiltonian of eq. (2.3), fig. 2.5 shows the absolute value of the difference of the two sides of eq. (2.7) for the function f and g, for the case when $\alpha' = 120$ and $\alpha = 66$. At these values of the parameter the trace is 2.0 and is increasing when the stability is about to be lost in a

pitchfork bifurcation and there are large stable islands (see fig. 2.3). Comparing figs. 2.3(a) and 2.3(b) with fig. 2.5 indicates that the area over which the scaling remains valid is much larger than the 'area of stability'. A similar result is obtained in the case of the function g as well.

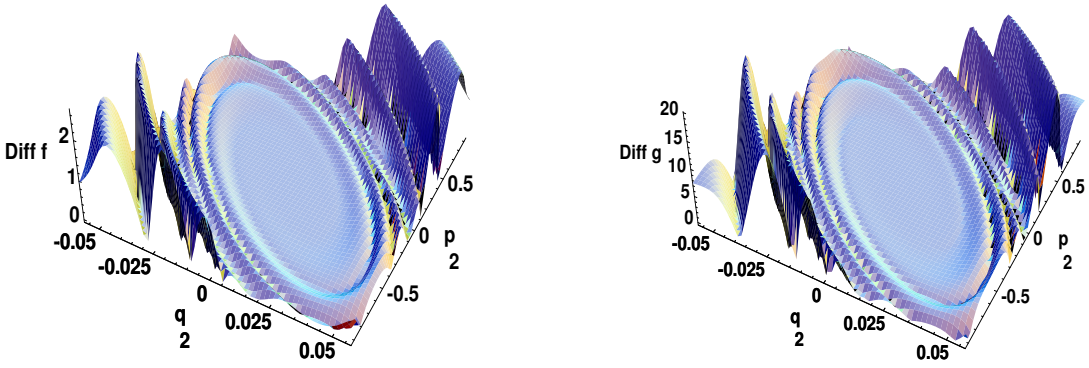

Figure 2.5: *The absolute difference between the two sides of eq. 2.7 (diff f and diff g) is plotted for functions f and g, when the channel orbit is stable.*

The scaling relation in eq. (2.7) is found to be valid even when the channel orbit is unstable, that is when there are no stable islands in the section. For instance, at $\alpha = 136$ and $\alpha = 78$, there are no stable islands in the section and the channel orbit is about to gain stability after a brief spell of instability. In fig. 2.6 we verify the scaling in this case, by plotting the absolute difference between both the sides of eq. (2.7).

Though there is ample evidence for scaling of the sections in the vicinity of the channel orbit, it is important to note that the orbits themselves may not scale. The orbits, in course of their time evolution, explore the chaotic regions of phase space in which the scaling relation eq. (2.7) is not valid. The scaling of orbits can be expected only if the evolving orbit does not go beyond the confines of the stable region in the phase space. Measuring the distances in the sections is the underlying approach to verify scaling as exemplified in the figs. (2.4). However this can be a cumbersome procedure. One rather efficient method is to determine the exponents based on eq. (2.7). First, we assume a fixed initial condition with $p_2 = 0$ and search along a range of values in the exponents for γ_1. This is possible since γ_1 unaffected by the value of γ_2. Once γ_1 is determined by the above procedure we can use it in eq. (2.7) and search for γ_2. Then using these values of exponents we can numerically verify the validity of the scaling equation, as we have shown in figs. 2.5 and 2.6.

The stability of the channel orbit is affected by the parameter α only if terms linear

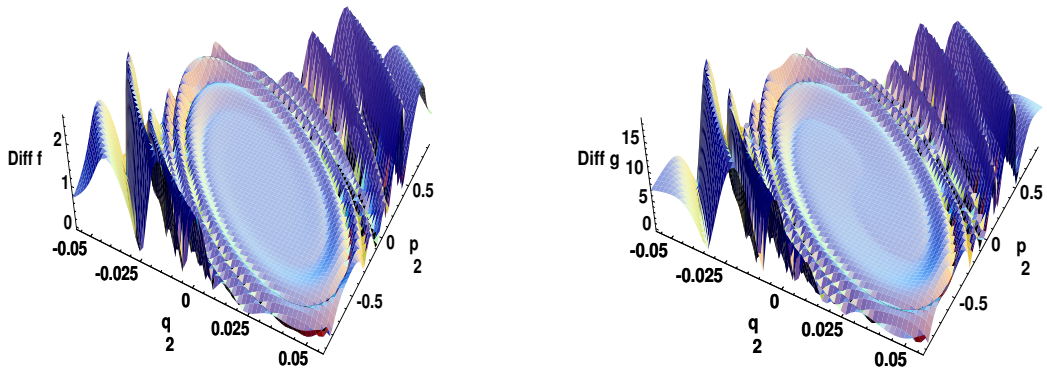

Figure 2.6: *The absolute difference (diff f and diff g) between the two sides of eq. (2.7) is plotted for functions f and g, when the channel orbit is unstable.*

in q_1 or q_2 are present in the linearised Hamilton's equations 1.2, or alternatively if the potential part of the Hamiltonian contains a quadratic term. All the class I Hamiltonians belong to this class. But we can construct Hamiltonians for coupled oscillators whose channel orbit stability is independent of the parameter α simply by not including any quadratic term in the potential. For the class II Hamiltonians of the form,

$$H'_{2n} = \frac{1}{2}p_1^2 + \frac{1}{2}p_2^2 + \frac{1}{2n}(\beta_1 q_1^{2n} + \beta_2 q_2^{2n}) + \frac{1}{n}\alpha q_1^n q_2^n, \quad n > 2. \tag{2.9}$$

the channel orbit is always marginally stable (Tr $J(\alpha) = 2$), independent of α and there is a stable region around this orbit which continuously scales with α. We found the corresponding exponents to be well predicted by the following rule:

$$\gamma_1 = \gamma_2 = \frac{1}{n-2}\,, \tag{2.10}$$

so that the area of stability island still scales as α^{-1} only in the case when $n = 4$. The term $q_1^n q_2^n$ ($n > 2$) is like a "gauge term" as far as the stability of the central orbit is concerned, since these terms do not enter the stability equations and hence do not affect the stability properties of the channel orbit. In this class of Hamiltonians the symmetry of parity is broken when n is odd, and the potential in these cases is bounded only if $-1 < \alpha < 1$. If n is odd, the *half* Poincaré map defined earlier for class I Hamiltonians is not valid, and hence we use the usual definition of *full* Poincaré map, namely, the successive intersections of the trajectory with the plane $q_1 = 0$ and $p_1 > 0$.

For example, in case of the Hamiltonian specified by the potential $(q_1^6 + q_2^6)/6 + \alpha q_1^3 q_2^3/3$, the phase space is largely chaotic for the seemingly low values of the coupling parameters near unity. Complete chaos is however absent, not only because

of the channel orbit but also due to the existence of one more stable island. In this case, the scaling exponents cannot be determined by measuring distances in the sections, as was done previously for class I Hamiltonians, because of lack of sufficiently convenient fixed points to measure distances. Hence the scaling exponents γ_1 and γ_2 are determined using the scaling relation eq. (2.7) by the method mentioned. In fact we have verified that the scaling relation holds good for any two different parameter values at which the stability of the channel orbit and the slope of the stability curve is the same; these parameter values need not necessarily be points of bifurcation.

The central result of this chapter is the local scaling of sections with respect to a single parameter for a class of nonlinear oscillators as distinct from the well-known scaling of orbits with respect to energy for the homogeneous Hamiltonian systems. The scaling exponents depend only on the degree of homogeneity of the potential.

2.3 Classical Dynamics of Coupled Quartic Oscillator

For further studies on quantum chaos, we will concentrate on the coupled quartic oscillator in the rest of this thesis. Now, to prepare the ground for the quantum studies, some more classical properties of coupled quartic oscillator is presented. For this, we will consider a slightly different Hamiltonian given by,

$$H(p_x, p_y, x, y; \alpha) = p_x^2 + p_y^2 + x^4 + y^4 + \alpha x^2 y^2 \tag{2.11}$$

where α is a parameter and we have taken $\hbar = 1$ all throughout this thesis. First we will look at the limiting case when $\alpha = \infty$, corresponding to the potential shown in fig. 2.1(b). In this limiting case the Hamiltonian is of interest in SU(2) Yang-Mills field theory [52]. This extreme parameter limit was of special interest because it was one of the prime candidates for a completely chaotic Hamiltonian system. However, it was later shown to contain few stable periodic orbits corresponding to miniscule islands in phase space [53]. The potential is bounded for all values of α greater that -2 (fig. 2.1(a)), except at $\alpha = \infty$. In this limit when $\alpha = \infty$, though classically the potential is open along the channels, the quantum energy spectrum is discrete [54].

The system is integrable as well as separable for $\alpha = 0, 2, 6$. The Poincaré section shows predominance of irregular trajectories as α increases beyond 6. The sections in fig. 2.7 provide a graphical description of integrability and chaos in the coupled quartic oscillator. The area of the regular regions shrink with an increase in α. Due to bounded stability oscillations of the channel periodic orbit, there are certain windows of α values for which infinitesimally small regular region around the channel orbit exists and this happens even for very high values of α. The formula due to Yoshida [49] for the trace of the monodromy matrix applied to the case of the quartic oscillator

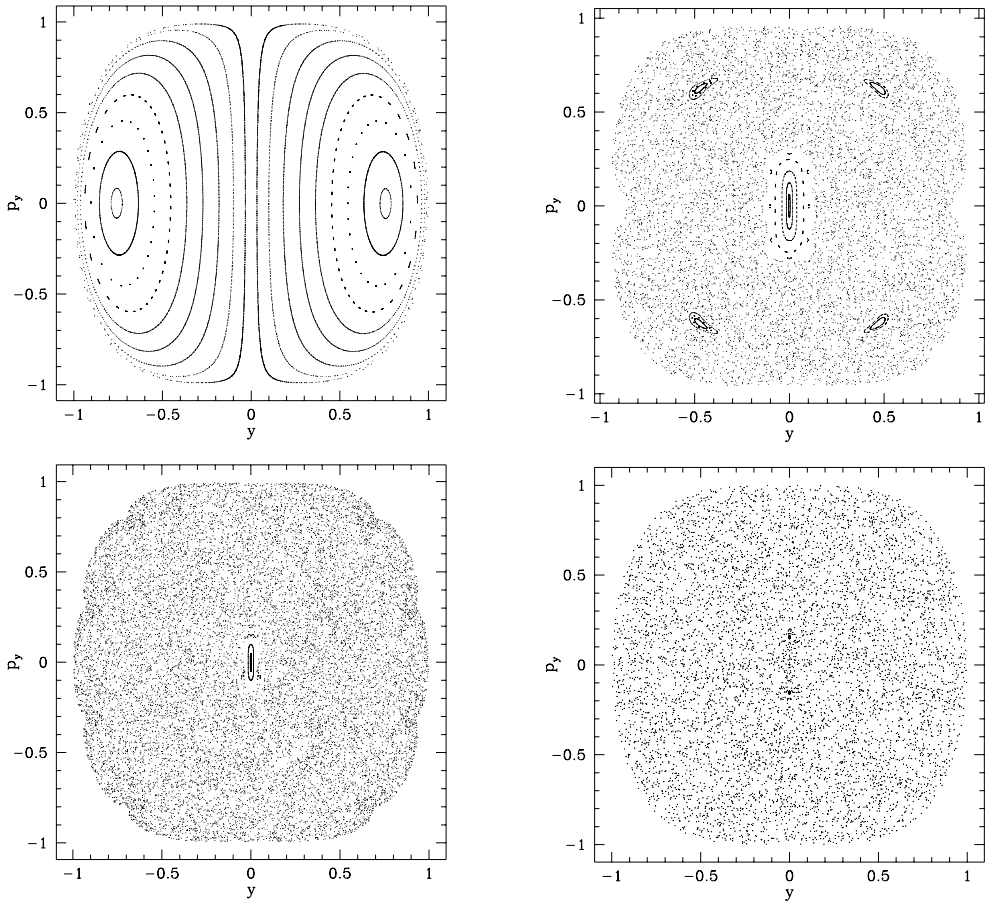

Figure 2.7: *The Poincaré sections at (a) integrable case* $\alpha = 2$ *and (b) nonintegrable case* $\alpha = 12$. *Predominantly chaotic sections at (c)* $\alpha = 90$ *and (d)* $\alpha = 96$.

in eq. (2.11) gives,

$$\text{Tr } J(\alpha) = 2\sqrt{2}\cos\left(\frac{\pi}{4}\sqrt{1+4\alpha}\right), \tag{2.12}$$

By inverting this formula using these stability conditions we find that at values of

$$\alpha = n(n+1) \tag{2.13}$$

where n is an integer, the channel orbit changes stability through a pitchfork bifurcation. Note that $\alpha = 90$ is a point of pitchfork bifurcation at which the channel orbit is just about to become unstable. The enlarged Poincaré sections in fig. 2.8 give a graphic view of bifurcation. The stable island around the fixed point of the channel orbit at $\alpha = 90$ bifurcates into two fixed points and moves away from the centre along p_y. At $\alpha = 96$, the two new fixed points can be seen, whereas the channel orbit itself has become unstable as seen from the hyperbolic fixed point at $y = 0, p_y = 0$.

The duality in the parameter space enables us to map the parameter interval [0,2] onto [6,2] and the interval [-2,0] onto [∞,6] and

$$\frac{H(p_x, p_y, x, y, ; \alpha)}{(\alpha+2)^{1/6}} = \frac{H(p_u, p_v, u, v, ; \alpha')}{(\alpha'+2)^{1/6}} \tag{2.14}$$

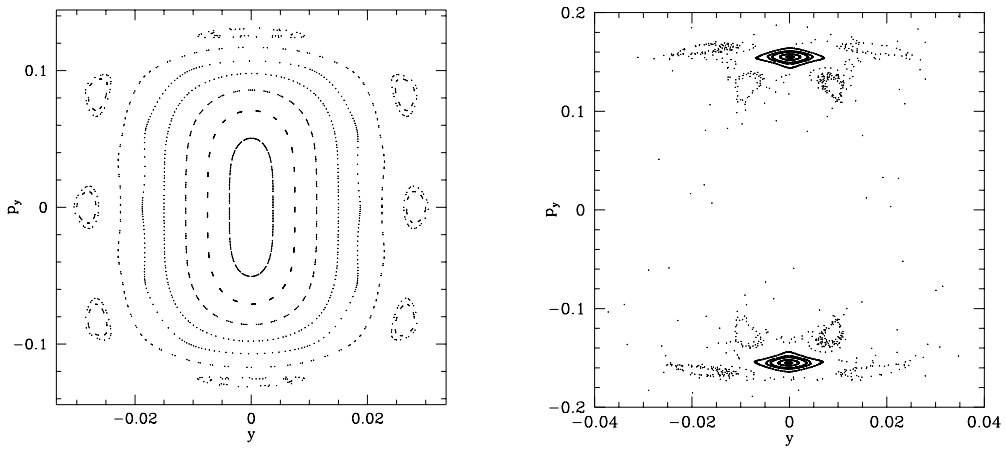

Figure 2.8: *The enlarged Poincaré sections in the vicinity of the channel orbit for (a)* $\alpha = 90$ *and (b)* $\alpha = 96$*. One fixed point at* $\alpha = 90$ *undergoes a pitchfork bifurcation leading to two new fixed points which have separated out at* $\alpha = 96$*.*

where

$$\alpha' = \frac{(12 - 2\alpha)}{(2 + \alpha)} \tag{2.15}$$

Geometrically, this transformation given by,

$$u = (4 + 2\alpha)^{1/6} \frac{(x + y)}{2}, \quad v = (4 + 2\alpha)^{1/6} \frac{(x - y)}{2}, \tag{2.16}$$

corresponds to rotation of the potential by $\pi/4$ and a scaling. As will be pointed out in the next chapter, this property is used to check the correctness of the eigenfuction calculations.

We have discovered some new classical local scaling behaviours for a class of homogeneous Hamiltonian systems. It is natural to examine its implications of classical properties of the channel orbit in the quantum regime, since by now it is well established that periodic orbits play a crucial role in determining the structures in the quantum eigenfunctions. From the point of view of eigenfunctions of the coupled quartic oscillators, to be studied in detail in the subsequent chapters, two important aspects of classical dynamics will have a significant bearing on them. First is the bounded stability oscillations of the channel orbit. Secondly, the parameter values α at which the bifurcation takes place, given by eq. (2.13), will play a significant role in understanding the structures in the eigenfunctions of the channel localised states.

Quantum Mechanics Of Nonlinear Oscillators

The focus of this chapter is two fold. Firstly, to present certain quantum aspects of the two dimensional coupled oscillators that will be studied in this thesis. In order to pursue the quantum mechanics of coupled quartic oscillators and other potentials studied in this thesis, we solve the time-independent Schroedinger equation given by eq. (1.9). As pointed out in the introduction, there are very few problems in both classical and quantum mechanics that can be exactly solved and hence the need to look for numerical solutions. In quantum chaos, since most of the available theoretical frame work provides results in the semiclassical regime, the interest is to compute highly excited states of the system, from the point of view of verifying the theoretical predictions and also to look for new signatures of classical chaos in the quantum regime. In this sense, the computational techniques form an indispensable tool. Hence the computational techniques adopted to obtain the results will be another concern of this chapter.

We begin with the coupled quartic oscillator model given by eq. (2.11). To set the tune, we again write down explicitly the Schroedinger equation for which we are looking for a solution.

$$\left(-\frac{\hbar^2}{2m}\bigtriangledown^2 + x^4 + y^4 + \alpha x^2 y^2\right)\Psi(x,y) = E\Psi(x,y) \tag{3.1}$$

The classical scaling property [46] of the Hamiltonian in eq. (2.3) referred to in the beginning of chapter 2, implies as usual the connection between spectra at different values of the Planck constant. In particular for the above Hamiltonian we get

$$E(\hbar;\alpha) = C^4\, E(\hbar/C^3;\alpha), \tag{3.2}$$

where C is any constant. Thus scaling allows us to equate climbing higher up in the spectrum with getting closer to the classical limit. In addition the property of duality in the parameter space implies the relationship between spectra at identical values of the Planck constant but at different values of the coupling constant, those connected by the eq. (2.15). Similar to the classical relation in eq. (2.14), we get

$$\frac{E(\hbar;\alpha)}{(2+\alpha)^{1/6}} = \frac{E(\hbar;\alpha')}{(2+\alpha')^{1/6}}. \tag{3.3}$$

Thus when we study the coupled quantum oscillator at $\alpha = 64.6667$, it is the same as studying it at $\alpha = -1.76$, however the convergence of the number of eigenvalues for a given matrix dimensionality is significantly better for the positive α domain.

3.1 Techniques for Solving Schroedinger Equation

Since exact closed form solution is not known and the parametric regimes of our concern do not permit the application of approximate techniques like the perturbation methods, we attempt the next best option; seeking 'numerically exact' solution. The literature provides few methods, that can be numerically implemented, for solving the eq. (3.1) to obtain the eigenvalues E and the eigenfunctions $\Psi(x, y)$. Iterative methods [55] form one such class in which starting from a guess initial eigenvalue the numerical integrations of the Schroedinger equation are performed and its corresponding eigenfunction is computed. This eigenfunction is used to refine the eigenvalue and this procedure is iteratively performed to determine the eigenvalue. As an alternative to iteration procedures, Feit et. al. have proposed a spectral method [56]. The Fourier transform of the correlation function $< \Psi(\mathbf{r}, 0)|\Psi(\mathbf{r}, t) >$ shows peaks corresponding at the position of eigenvalues and this is used to determine the eigenvalues. The correlation function itself is calculated using the split operator FFT method. More details on this method are given in ref [56].

3.1.1 Basis Set Diagonalisation

The other popular method is the basis set diagonalisation, which we will adapt here. This method is based on the fact that an arbitrary wavefunction can be expanded in a complete set of basis states. Let $\mathcal{H}_0$ be a preferably classically integrable Hamiltonian with the eigenvalue equation, $\mathcal{H}_0(\hat{\mathbf{p}}, \hat{\mathbf{q}})\psi_n(\mathbf{q}) = \epsilon_n\psi_n(\mathbf{q})$ whose eigenfunctions $\psi_n(\mathbf{q})$ and eigenvalues ϵ_n are known, such that the eigenfunctions form a complete set. The quantum Hamiltonian is of the form,

$$H(\hat{\mathbf{p}}, \hat{\mathbf{q}}) = \mathcal{H}_0(\hat{\mathbf{p}}, \hat{\mathbf{q}}) + V(\hat{\mathbf{q}}; \alpha) \tag{3.4}$$

where α is the perturbing parameter and $H_0(\hat{\mathbf{p}}, \hat{\mathbf{q}})$ is the unperturbed Hamiltonian. Then the usual approach is to the expand the eigenfunctions $\Psi_n(\mathbf{q})$ of $H(\hat{\mathbf{p}}, \hat{\mathbf{q}})$ in terms of the eigenfunctions of $\mathcal{H}$ as follows,

$$\Psi_n(\mathbf{q}) = \sum_{j=1}^{\infty} a_{n,j}\psi_j(\mathbf{q}) \tag{3.5}$$

In many cases, $\mathcal{H}_0$ might be the unperturbed Hamiltonian $H_0(\hat{\mathbf{p}}, \hat{\mathbf{q}})$ itself, in which case, the basis set $\psi_n(\mathbf{q})$ is called the unperturbed basis for obvious reasons. Thus, the matrix elements of Hamiltonian operator $\hat{H}$ is computed in the chosen basis and a sufficiently large Hamiltonian matrix is diagonalised to obtain the eigenvalues and the eigenstates of the system of our interest. For the coupled oscillators we will study in this thesis, the above procedure cannot be performed analytically but can only be done numerically.

Notice that as per eq. (3.5), we will have to sum up infinite terms, in principle, to construct the required eigenstate. However, in practice the number of basis states is truncated leading to what is called the convergence problem in the computed eigenvalues. Though the above procedure is fairly straightforward to implement, however, in practice the choice of proper basis states plays a crucial role in efficient diagonalisation to obtain a large number of eigenvalues of the system.

3.2 Discrete Symmetries of the Potential

However, before we try to compute the numerical solution, the discrete symmetries present in the potential can be exploited to simplify the problem further. Group theory provides the mathematical tool to study the symmetries in the potential and incorporate them in the solution. This attempt at devising a group theoretical framework is not just an exercise in elegance of solution. This affords the following advantages. Firstly, the matrix element theorm [57] in group theory shows that the matrix elements between functions of different symmetry classes vanish. Hence, the Hamiltonian matrix constructed in an appropriately symmetrised set of basis states is block diagonal in form and so we are left with matrices of smaller dimensions to deal with. Thus, from a computational point of view, it leads to significant saving in CPU time and storage space. It is now well known that the quantal energy level spacings, for classically chaotic quantum systems show level spacing distribution of the appropriate RMT ensemble and for classically integrable systems show Poisson distribution [58]. The universal level spacing distributions, modelled by random matrix theory, arise from the presence of avoided crossings in the spectrum, since the systematic degeneracies arising from the presence of symmetries is removed by confining to particular symmetry class. Thus, symmetry considerations are important from the point of view of spectral statistics [59].

Briefly, the procedure is as follows. By studying the contours of the potential we identify those transformations that will leave the potential invariant. In practice it is useful to consider the transformations of an equivalent geometrical object under which the potential remains invariant. These symmetry transformations form the elements of the group for the potential under consideration. We then construct the character table for the relevant group using orthogonality theorems [57]. With the help of the character table we construct symmetry adapted basis functions that will transform according to the different irreducible representations. In this chosen special basis, the Hamiltonian matrix is block diagonal in form.

The Schroedinger eq. (3.1) for the coupled quartic oscillator is solved numerically in the basis of the linear combination of the eigenfunctions of corresponding unper-

turbed system, namely the $\alpha = 0$ case of the eq. (3.1). The specific form of the basis function to be chosen is dictated by symmetry considerations as follows. The coupled quartic oscillator given by eq. (2.3) belongs to C_{4v} symmetry group with 4 one-dimensional representations and one two-dimensional representation. The C_{4v} is the group of all symmetry transformations of a square. The symmetrised two-dimensional basis states which will transform according to 4 one-dimensional irreducible representations of the C_{4v} are are of the general form,

$$\psi_k^R(x,y,z) = \phi_n^{o/e}(x)\phi_m^{o/e}(y) \pm \phi_n^{o/e}(y)\phi_m^{o/e}(x) \tag{3.6}$$

where, R represents the four one-dimensional irreducible representations, k represents a unique doublet of quantum numbers (n,m) and o/e represents odd or even parity depending on the representation being considered. The functions $\phi_n(x)$ are obtained numerically by accurately solving a one-dimensional Schroedinger equation,

$$\left(-\frac{\hbar^2}{2m}\frac{\partial^2}{\partial x^2} + x^4\right)\phi_n(x,y) = E_n\phi_n(x,y) \tag{3.7}$$

for the bound states of the quartic oscillator. One of the methods used to solve such one-dimensional Schroedinger equations is the Hill determinant method [60]. In this method, a convenient wavefunction ansatz is assumed as the basis states and substituted in the Schroedinger equation leading to recurrence relation for the coefficients of the assumed basis states. The condition for nontrivial solutions for the coefficients leads to a determinant whose roots are identified with the eigenvalues. But this method has been shown to be useful to obtain the spectra for certain potentials [61] and unreliable in certain other cases [62]. In our work the Schroedinger eq. in (3.7) is solved by a generalised phase-amplitude method proposed by Larsen [63]. In this method the phase and amplitude functions of the two linearly independent solutions of (3.7) are determined separately through appropriate quantisation conditions. Hence it is possible to determine accurately the eigenvalues and eigenfunctions for very high quantum numbers. More details of this procedure are given in [64].

With the choice of basis states given by eq. (3.6), the Hamiltonian matrix will be block diagonal in form. In this thesis, we will study only the eigenfunctions from the A_1 symmetry class of the coupled quartic oscillator, and thus the chosen basis function for A_1 representation is given by,

$$\psi_j(x,y) = \mathcal{N}(n,m)\{\phi_n(x)\phi_m(y) + \phi_m(x)\phi_n(y)\} \tag{3.8}$$

the index j refers to a *unique* pair of *even* indices $\{n,m\}$ and $\mathcal{N}(n,m)$ is a normalisation factor,

$$\mathcal{N}(n,m) = \frac{1}{\sqrt{(2+2\delta_{n,m})}} \tag{3.9}$$

The eigenfunctions of eq. (3.1) will be given by,

$$\Psi_n(\mathbf{q}) = \sum_{j=1}^{\infty} a_{n,j}\psi_n(\mathbf{q}) \tag{3.10}$$

where $a_{n,j} =< \psi_n(\mathbf{q}) \mid \Psi_n(\mathbf{q}) >$ are the expansion coefficients or the eigenvectors in the unperturbed basis.

3.3 Numerical Techniques

Implementing the basis set diagonalisation numerically we have computed about 2500 eigenstates, counted sequentially from the ground state, for the coupled quartic oscillator for several parameter values ranging from $\alpha = 64$ to 96. In this section, we will go through briefly the numerical improvisation adopted to reliably compute the highly excited states. From this point onwards we will confine to quartic oscillator model unless otherwise specified.

First step is to compute the one dimensional states by solving eq. (3.7). In this work, one-dimensional basis states $\phi_n(x)$ are computed using a generalised phase-amplitude method. This method associates the phase and amplitude of the wave-function to a function that satisfies the Riccati equation. Since the phase and the amplitude of the eigenstate is separately computed this approach is particularly suitable for calculating highly excited eigenstates. We will not pursue the details of this method here, since it is known for quite sometime now and is reported in the literature [64]. For the purposes of our studies, we have computed one-dimensional quartic oscillator states with quantum numbers up to $n = 400$.

Once the two-dimensional basis states $\psi(x, y)$ for A_1 symmetry class are assembled, the next step is to construct the Hamiltonian matrix $< \psi_j(x, y) \mid H \mid \psi_{j'}(x, y) >$. This requires a large number of integrals of the form

$$\int_{\infty}^{\infty} dx \;\; \phi_m(x) \; x^2 \;\; \phi_n(x) \tag{3.11}$$

corresponding to the coupling terms in the potential, which are again numerically performed. For the Hamiltonian matrix of order N, the number of such integrals required will be $N(N+1)/2$. In all our calculations, we have typically employed 200 one-dimensional even parity quartic oscillator eigenfunctions to construct Hamiltonian matrices of order about 15000.

At this point the question might raised as to the wisdom of using quartic oscillator basis states instead of using the more convenient harmonic oscillator states. Many of the reported work on coupled quartic oscillator have employed harmonic oscillator eigenfunctions as basis states. The advantages with using harmonic oscillator eigenfunctions as basis states are well-known; the harmonic oscillator spectrum is exactly

known, the Hamiltonian matrix will be banded, the matrix elements can be analytically calculated and hence the Hamiltonian matrix is also exactly known. Though employing harmonic oscillator states are advantageous from the computational point of view, they are not suitable for computing a large number of excited states. The eigenfunction for a highly excited state of the quartic oscillator has more nodes than the corresponding one of the harmonic oscillator. Thus many more harmonic oscillator states would be required to construct a quartic oscillator eigenfunction accurately. Thus computation of a large number of converged eigenvalues and eigenfunctions using lesser number of basis states is possible with quartic oscillator eigenfunctions. This factor outweighs all other computational advantages of using harmonic oscillator basis.

The diagonalisation of the Hamiltonian matrix is carried out using standard routines from EISPACK and LAPACK [65]. The modus operandi is to tridiaonalise the given matrix first and then obtain the eigenvalues by the well-known bisection method. The eigenvectors are then computed by an inverse iteration process. Since these numerical methods and the computer codes are well documented [66] we will not discuss about them here. By this procedure, we obtained about 2500 eigenvalues, converged up to 6 decimal places, for the coupled quartic oscillator by diagonalising Hamiltonian matrices of order 15000. It must be noted that the convergence of eigenvalues does get poorer as the parameter α increases. Hence the convergence obtained is for the parametric regions of our interest in this thesis, namely $\alpha = 64$ to 96 and is not true in general for any arbitrary value of the parameter.

The CPU time consumption, for the entire computational exercise mentioned above, can be prohibitive. For instance, in the IBM RS6000/580 RISC processor machine, diagonalising a real symmetric matrix of order 15000 can take about few days of CPU time. The RAM (random access memory) required to run the programs is much more than what this computer offers. If we keep increasing the size of matrix, even the best of the computer might run out of RAM space. Hence this procedure is computer intensive, if not impossible, and time consuming. It would be greatly helpful if the Hamiltonian matrix can be banded without using harmonic oscillator basis states, since banded symmetric matrices consume less RAM space and can be diagonalised much faster than a dense matrix of the same size.

3.4 Numerical Banding of Hamiltonian Matrices

Though in principle any complete orthogonal set of basis states is sufficient to solve the problem, in practice an efficient numerical diagonalisation depends crucially on the choice of appropriate basis states. One of the important advantages of the har-

monic oscillator eigenfunctions as basis states is that the the Hamiltonian matrix in this basis is banded leading to significant saving on CPU time and storage. To solve the coupled quartic oscillator problem, we will have to obtain numerically the matrix elements, $M(n,n') =< \phi_n(x)|x^2|\phi_{n'}(x) >$, as pointed out earlier. In fig. 3.4 we show $\log| < \phi_n(x)|x^2|\phi_{n'}(x) > |$ plotted against n' for three different fixed values of n. The figure shows that the matrix elements fall off exponentially as a function of n'. Based

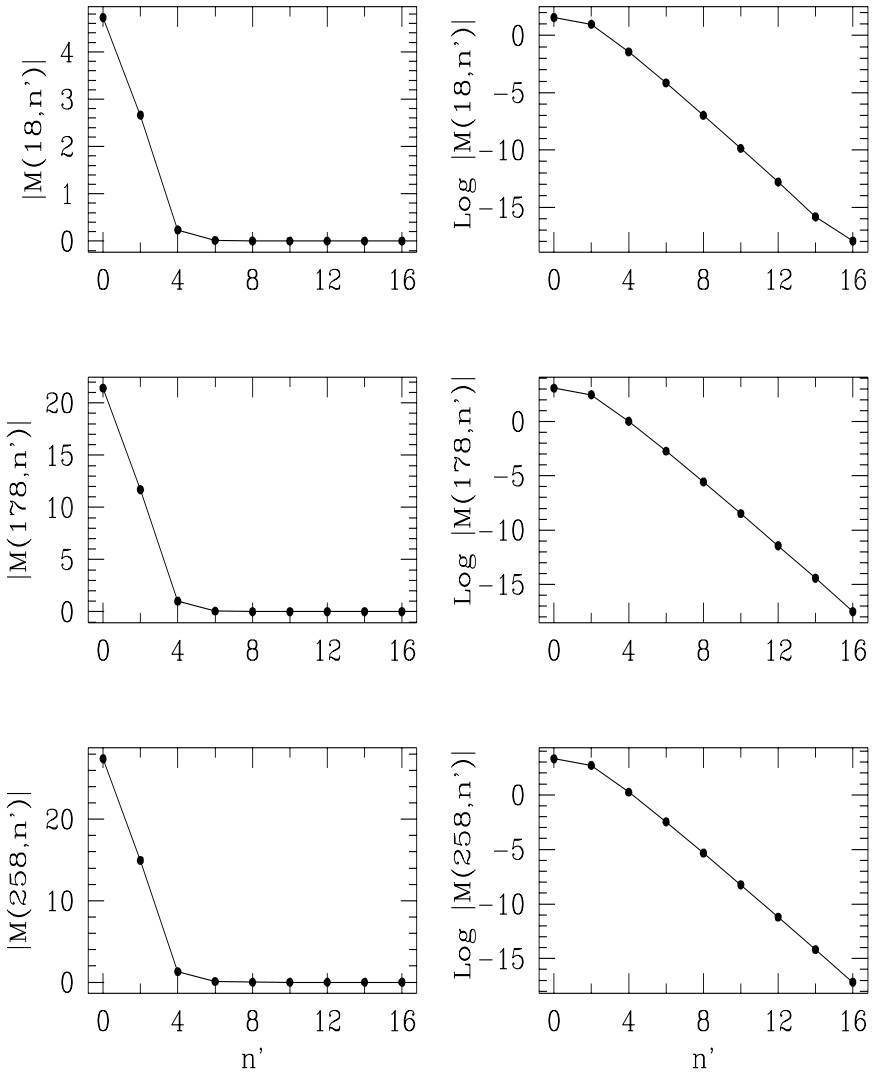

Figure 3.1: *The exponential fall of the matrix elements of x^2 in the one-dimensional quartic oscillator basis. The plots are the matrix elements and the logarithm of the matrix elements.*

on the numerical values of the matrix elements, we found that,

$$| < \phi_n(x)|x^2|\phi_{n'}(x) > | \approx 10^{-10} \approx 0 \qquad\qquad n' > (n \pm 10) \tag{3.12}$$

This condition was imposed on the one-dimensional matrix elements while computing the full Hamiltonian matrix for the coupled quartic oscillator. This leads to an effectively banded Hamiltonian matrix, the next best to using the harmonic oscillator eigenfunctions. At this point two salient features need to be noted. From the symmetrised form of the basis states used in eq. (3.8) we note that the matrix elements for the two-dimensional quartic oscillator actually involves product of the matrix elements given in eq. (3.11) and hence the numerical banding will be much more effective. Secondly, the magnitude of the matrix elements depends only on the difference $|(n' - n)|$ and not on the magnitude of the individual quantum numbers and so the banding criteria will remain true for even large values of n and n'. In the case of Hamiltonian in eq. (2.3), we constructed a Hamiltonian matrix of order 12880 and by imposing the above condition the bandwidth, the number of super or sub-diagonals with non-zero entries, was found to be 790. This procedure leads to considerable saving in CPU time and RAM space for running the programs.

3.5 Accuracy and Errors

We conclude this chapter with a small note on the accuracy of our computational results. All the eigenvalues presented in this thesis have an accuracy of 10^{-6}. We note that the accuracy or the convergence of the eigenvalues is not affected by the above numerical banding we have performed. In fig. 3.5 we show the difference between first 2100 eigenvalues (ΔE) obtained from a diagonalisation of a full Hamiltonian matrix of order 6105 and from the corresponding numerically banded matrix of order 6105 and with a bandwidth of 540. If E_f and E_b represent the eigenvalues from the full matrix and eigenvalues from the banded matrix respectively, then $(\Delta E) = |E_f - E_b$. The number of converged eigenvalues, about 900 in this case, is also unaffected by the banding procedure. The figure shows that even at the worst, the eigenvalues of the Hamiltonian matrix differ only by about 10^{-3}, even though they may not have converged to the energy eigenvalue of the system being considered.

Behind every numerical attempt, there could be a lurking fear about the correctness of the results obtained. In our case, we performed several checks and took advantage of the approximate methods like variational method to check few of the obtained energies. However, checking correctness of the eigenvectors is not so trivial. The study of eigenfunctions has a strong component for visualisation using computer graphics. To illustrate visualisation and at the same time to check the eigenstate computation, we consider the following. In eq. (2.16) the transformation between two domains of parameters α and α' is shown. For instance, a wavefunction at $\alpha = 64.66$ and at $\alpha' = -1.76$ are related by a rotation of basis by 45^o. Thus, a channel lo-

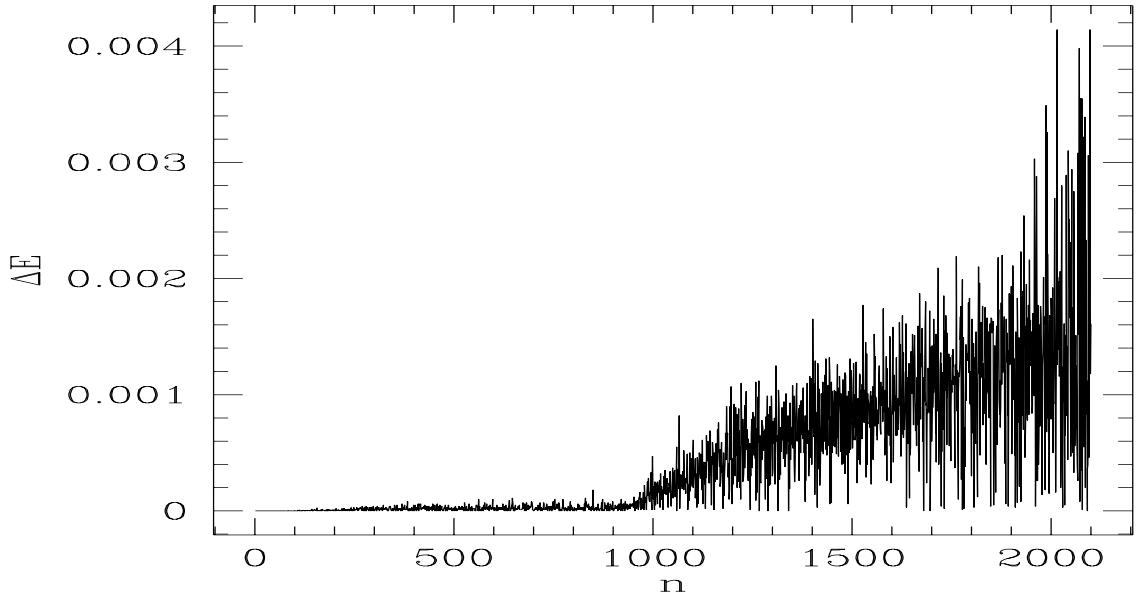

Figure 3.2: *The quantity* (ΔE) *is plotted for first 2000 eigenvalues. The information lost due to banding is insignificant.*

calised state at $\alpha = 64.66$ will appear to be exactly look like the corresponding state at $\alpha = -1.76$ except that the latter is rotated by 45^o and scaled.

We close this chapter also by displaying two eigenfunctions in fig. 3.4 and fig. 3.3 as an evidence of correctness of eigenvectors coming from two independent calculations. The fig. 3.4 and fig. 3.3 shown in the next page are the two wavefunctions related by the tranformation eq. (2.16). Apart from such visual methods of verifying eigenvector calculations, other essentially numerical methods have also been adopted and checked for accuracy.

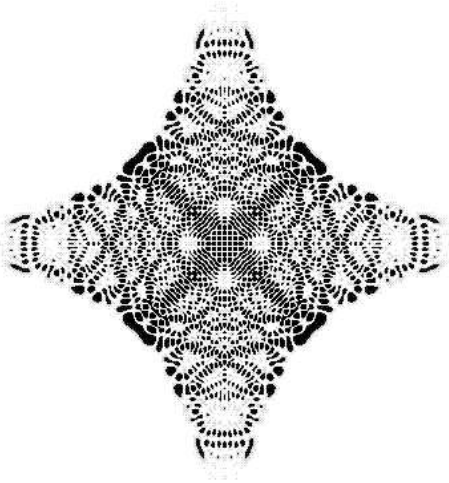

Figure 3.3: *Eigenfunction of the coupled quartic oscillator. State number 407 at* $\alpha = 64.66$.

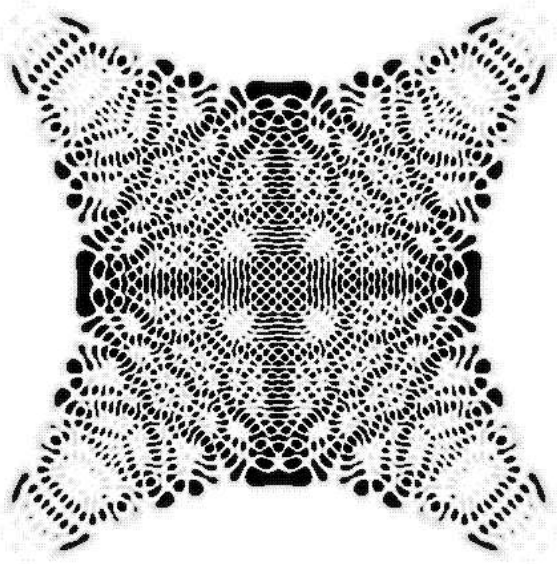

Figure 3.4: *Eigenfunctions of the coupled quartic oscillator. State number 407 at* $\alpha = -1.76$. *This shows the expected relation between the two eigenfunctions based on eq. (2.16).*

Localisation in Quartic Oscillators

At the outset, the term 'localisation' needs some clarification. Though localisation is used in various contexts in the study of quantum systems in different branches of physics, in this thesis and in the particular context of the coupled quartic oscillators we will reserve this term to denote eigenstates scarred by the channel periodic orbit defined by the initial condition $(x, y = 0, p_x, p_y = 0)$. They will be referred to as channel localised states or simply as localised states, unless otherwise specified. In the fig. 4.1 shown below, we have plotted the $\mid \Psi(x, y) \mid^2$ as an image plot. All such black and white images of eigenstates shown in this thesis are probability density plots with darker regions representing higher intensity and pure white corresponds to zero intensity. The difference between a typical state and a localised state is clearly brought

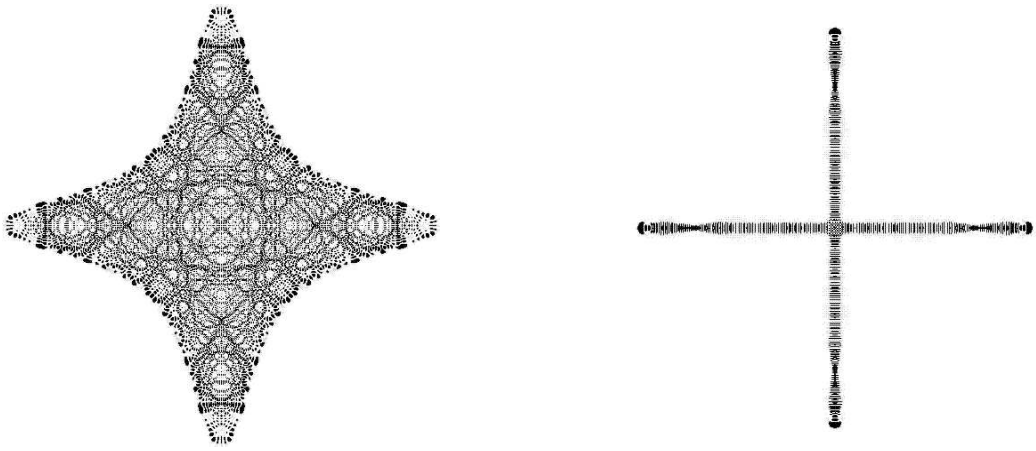

Figure 4.1: *Eigenstates of coupled quartic oscillator : (a) A typical eigenstate, 1973rd state (b) A localised state, 1972nd state. (both at* $\alpha = 90.0$

out in this figure. Most of our results pertain to localised states of the kind shown above. These localised states are remarkable since they form a denumerably infinite series in the spectrum; that is they occur at regular intervals in the spectrum and this interval between the successive localised states keeps increasing as we explore the highly excited regions of the spectrum. For instance, in the region of state numbers 400-500, there are about 15 states between successive localised states whereas high up in the spectral region of 2000th state, there are about 30 states between successive localised states. The localised states are known to affect the spectral statistical properties like the eigenvalue spacing distribution [67] and eigenvector statistics [68, 69]. Since the regions of high probability density in the localised states coin-

cides with the coordinate axis (see figure above) the energies of these states can be estimated using certain approximate methods that includes standard semiclassical quantisation. In this chapter, the analysis of the systematics, structure and morphology of the localised states proceeds along the following lines. We propose a numerical method based on the information entropy measure to identify these localised states. The numerical evidence shows that these class of states are exponentially localised in the unperturbed basis. We use the entropy measure to show that the stability of the underlying periodic orbit correlates strongly with the degree of localisation. With this brief outline of the plan we proceed to give the details.

4.1 Scarred States in Quartic Oscillator

In the integrable quartic oscillator ($\alpha = 0$) all the eigenfunctions are localised on the invariant tori. As the parameter α increases beyond 6, the invariant tori are continually destroyed and the only invariant structure of significant measure in the classical phase space is the energy surface. Since it was implicitly assumed that only the classical invariant structures can affect the quantum wavefunctions, it was expected that as we approach the classical limit ($\hbar \to 0$), the quantum wavefunctions will carry the imprint of the classical dynamics on the energy surface. For a classically chaotic system, the structure in the wavefunctions were expected to reflect the ergodic nature of the classical trajectories on the energy surface [27]. However, as Heller's arguments later showed, isolated periodic orbits can also influence the eigenfunction structures and some of them do so more than the others [32]. Thus the structures in the eigenfunctions reflect the variety available in the structure of periodic orbits, of which the channel periodic orbit is one of the simplest. In this chapter we will concentrate on the quantum states scarred by the channel periodic orbit.

In one of the first studies on the eigenfunctions, Eckhardt [71] *et. al.* have surveyed about 60 eigenfunctions from the ground state for the quartic oscillator in each of the four irreducible representations of C_{4v} point group and associated them with classical periodic orbits. In the course of our work presented below, we have computed a large number of eigenfunctions exploring further the higher end of the quantum spectrum. In this section we present some more eigenfunctions in the highly excited regions with state numbers ranging from 1500 to 2000 for several values of the parameter, but all of them confined to A_1 irreducible representation of C_{4v} group. Here we display a gallery of eigenfunctions. The three numbers that follow each eigenfunction are the parameter value α, the state number and the energy of the state.

From the series of wavefunctions presented above, we come to the following conclusions. Structurally, scarred states of the quartic oscillator display one or more of the following simple features, namely, (i) localisation along the channel scarred by the channel periodic orbit, (ii) localisation along a straightline rotated by 45^o to the channel state, scarred by its underlying orbit, (iii)localisation along a simple closed curve, scarred by ring orbits. However, as we see there are many other scarred states with interesting structures influenced by more than one periodic orbit. They do not fall in any of the above categories. For instance, we have noticed some peculiar states which appear localised at distinct points rather than along lines or curves [72]. The interest in the three predominant structural types mentioned above stems from the fact that, as of now, approximate theoretical analysis has been possible only for these types of scarred eigenstates. To this well-known list, we add one more class of scarred states, which we call the shadow state. These states also form a series and are localised along the channels but not scarred by the channel orbit alone. The shadow states always occur in the vicinity of the channel localised states. Although they follow every channel localised state it is not clear if they form a series in the same sense as the channel localised states do.

As pointed out, the channel localised states form a dominant series in the spectrum. One of the important questions is wheather these localised states will exist in the highly excited spectral regions, which correspond to going closer to the classical limit. Probing much deeper in the semiclassical regime, even as high as up to 2500 states that we computed for various α values from 60 to 96, we found that the localised states scarred by the channel orbit continue to exist and possibly might even survive the classical limit.

4.1.1 Husimi Distribution and the Scarring Orbit

At this point, we digress a bit to point out the importance of Husimi distribution in identifying the classical orbit responsible for scarring an eigenstate. In general, associating a periodic orbit with a scarred state is not straightforward, except in some simple cases like the channel localised states. One method of doing this is to study the Husimi distribution. Given a minimum uncertainty wavepacket of the harmonic oscillator,

$$\begin{aligned} < x,y|q_1,q_2,p_1,p_2 > &= \Phi^{coh}_{q_1,q_2,p_1,p_2}(x,y) \\ &= \sqrt{\frac{1}{2\pi\hbar\sigma_x\sigma_y}}\exp\left(-\frac{(x-q_1)^2}{4\sigma^2}-\frac{(y-q_2)^2}{4\sigma^2}+\frac{i}{\hbar}(p_1x+p_2y)\right) \end{aligned} \tag{4.1}$$

centered at the phase space point (q_1,q_2,p_1,p_2), the inner product of an eigenstate, $< x,y|\Psi_E >$, with the minimum uncertainty state, $| < \Phi(q_1,q_2,p_1,p_2)|\Psi_E(x,y) > |^2$ is

called the Husimi distribution [73]. This is a quasi-probability distribution, originally introduced as a Gaussian smoothing of the Wigner function to make the Wigner function positive definite. Husimi function gives the probability for an eigenstate to be found in the given coherent state. Physically this corresponds to probability for finding the particle in a volume $\hbar^N$ centered around the point in phase space. Note that Husimi distribution as defined above is a function of four variables (q_1, q_2, p_1, p_2) and is difficult to visualise on a plane. Hence, we take a cut by setting $q_1 = 0$. Then,

$$< \Psi_E|0, q_2, p_1, p_2 >= \int \exp\left(-\frac{x^2}{4\sigma^2} - \frac{(y-q_2)^2}{4\sigma^2} + \frac{i}{\hbar}(p_1 x + p_2 y)\right) \quad dx \;\; dy \tag{4.2}$$

Now, we will integrate over the p_1 variable since the dominant contribution from p_1 comes from the vicinity of $x = 0$ due to the presence of $\exp(-x^2)$ term. This gives,

$$< \Psi_E|q_2, p_2 >= \int \exp\left(-\frac{(y-q_2)^2}{4\sigma^2} + \frac{i}{\hbar}p_2 y\right) \quad \Psi_E(0, y) \;\; dx \;\; dy \tag{4.3}$$

The Husimi distribution we visualise on the plane is given by,

$$\rho^H(q_2, p_2) = | < \Psi_E|q_2, p_2 > |^2 \tag{4.4}$$

The quantity we have shown in eq. (4.4) has peaks in intensity at points where there are periodic points in the corresponding Poincaré section. Taking lead from the peaks in the quantum surface of section, we search for the periodic point in the corresponding Poincaré section and thus locate the periodic orbit we are seeking. In this sense, Husimi distribution is an important tool to study quantum-classical correspondence.

This procedure is demonstrated here for an eigenstate which we identified unambiguously as a shadow state. We choose 1964th eigenstate at $\alpha = 90$ to identify the classical orbit responsible for scarring this eigenstate. The eigenstate is shown in the gallery of pictures shown above. The fig. 4.2 shows its Husimi distribution, the classical Poincaré section, the enlarged version of a miniscule stable region and the actual orbit. The Husimi shown in the fig. 4.2 corresponds to $(x - p_x)$ section and the coordinates of the peaks are at $(x = 0.0, p_x = 0.1545)$. The Poincaré section shows small dark island in the vicinity of this coordinate points. If we enlarge that dark region we see an intricate set of islands with a fixed point at $(x = 0.0, p_x = 0.154329)$. With the initial condition $(x = 0.0, p_x = 0.154329, y = 0.0, p_y = 0.0)$ we get the periodic orbit shown in the next figure. Earlier works have implemented a similar procedure to identify the periodic orbits that scar an eigenstate for the quartic oscillator system [74]. In ref. [74] they use an alternative definition of Husimi function based on fixing p_1 from the energy conservation principle. However, it must be noted in their case the orbits happen to be simple.

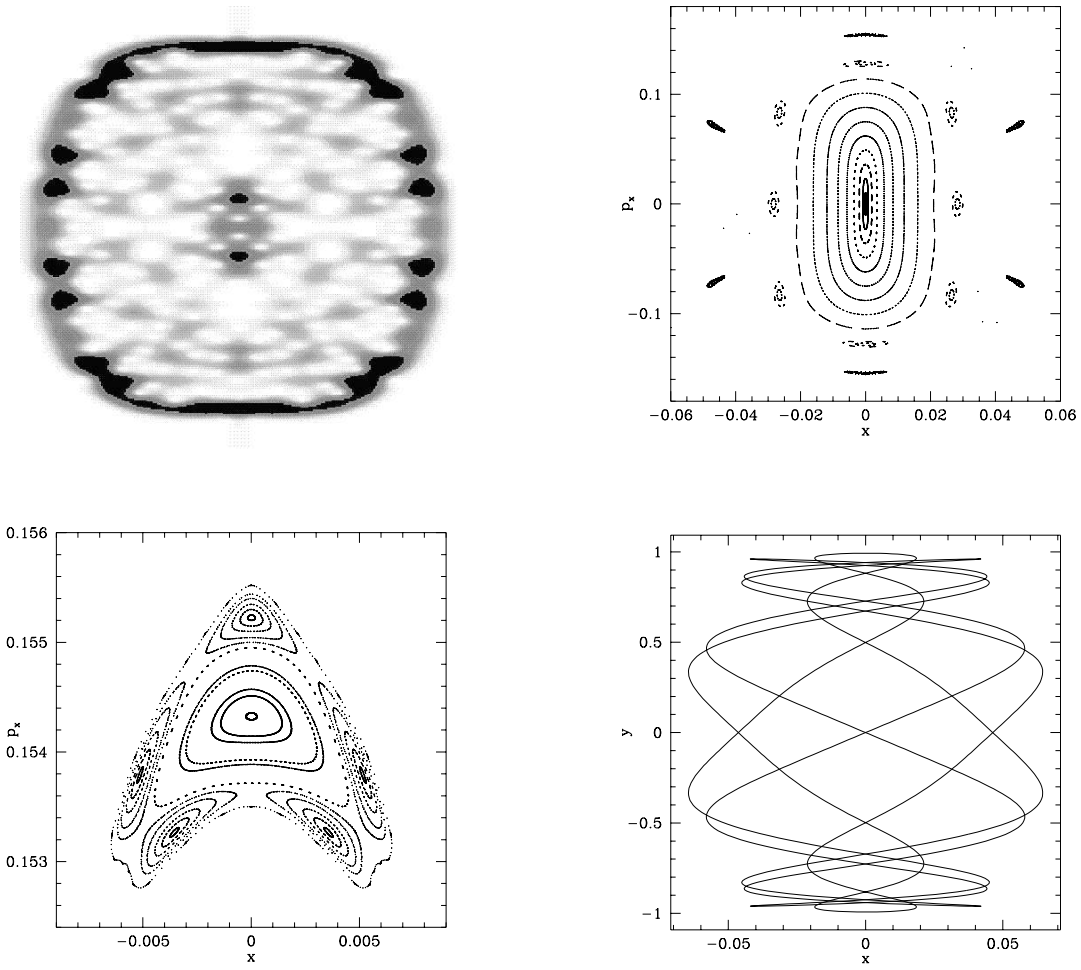

Figure 4.2: *Shadow state ; State number 1964 at* $\alpha = 90.0$. *(a) Husimi (*$x - p_x$ *section) for the shadow state (b)* $x - p_x$ *Poincaré section ; The scarring orbit corresponds to six dark islands shown in the section (c) The enlarged version of the vicinity of fixed points shown as dark islands in the previous figure and (d) the periodic orbit that scars the eigenstate.*

The 1964th eigenstate at $\alpha = 90$ is scarred by the complicated orbit shown above. The fig. 4.2 identifies a complicated orbit of long time period as responsible for scarring the shadow state, which lies along the channel but is *not* the channel periodic orbit. We recall that *all* the channel localised states are scarred by the *same* channel periodic orbit, scaled by the appropriate energy of the localised state. But our analysis indicates that the shadow states are not scarred by the same orbit. To understand the scenario, for the moment, we will consider only shadow states at $\alpha = 90$. If all the shadow states at this parameter value are scarred by the same orbit we expect that the Husimi function will exhibit peaks at different points which will essentially correspond to the same periodic orbit scaled by the energy of the eigenstate.

However, our analysis of a large number of shadow states indicates that the coor-

Table 4.1: *Table showing the coordinates of peaks in Husimi function. The values of coordinates are scaled to energy* $E = 1.0$

State number	Energy	x	p_x
319	1095.453	0.0	0.16363
896	2223.690	0.0	0.14842
1238	2767.116	0.0	0.16633
1604	3300.604	0.0	0.13761
1851	3633.026	0.0	0.17742

dinates of the peaks in Husimi function do not even approximately coincide with the fixed point of the miniscule island shown in fig. 4.2 but lie mostly within this island region. The Table 4.1.1 shows the coordinates of peaks obtained from the Husimi distribution. In fact, this happens to be the scenario for $\alpha = 96$ as well leading to the conclusion that the small stable island plays an important role in scarring the shadow states. The reason for this seems to be two fold. Firstly the Husimi distribution we define takes into account the wavefunction along a line and does not use the full information available in it. Secondly, the channel orbit undergoes higher period bifurcations continuously and there are always new orbits being born out of the channel orbit or some orbits coalease with it. In the Poincaré section, this is seen in the form of small groups of islands that surround the central island as shown in the figure fig. 4.2. Also note that the area of these islands are very small. At any given value of the parameter, there are such stable and unstable orbits in the vicinity of the channel orbit. We do not know the stability properties of these other orbits as a function of the parameter. It is possible that at some values of the parameter certain stable or unstable orbits exist when the scars in the shadow states are prominent and can be identified unambiguously with that orbit. At some other parametric values, due to changes in the orbit structure, the shadow states cannot be easily attributed to the same orbit. Thirdly, we should note that in the case of shadow state used as illustration above, it is a period-3 stable orbit which is responsible for scarring rather than a least unstable orbit as argued by Heller [32]. From the foregoing discussion, it is clear that the higher period orbits in the vicinity of the channel orbit are also responsible for scarring in channel states. Though we can identify the scarring orbit in some particular cases, it is not always possible to do so unless we track these orbits and their stability properties as a function of the parameter.

4.2 Identification of Localised States

A glance at the gallery of eigenfunctions shows the complexity of patterns exhibited by them. The states scarred by channel orbits form a small fraction of the total number of eigenstates we computed. There are about 60-70 channel localised states in first 2000 states. Many others exhibit various other types of structures and cannot be easily categorised. Hence to go beyond morphological features and take a complete view of all the states, quantitative methods are needed. The visual means are more computer intensive and for systems with more than two degrees of freedom, they may not be helpful. So we proposed the information entropy measure as a means to identify localised states [72]. It is well known that the concept of entropy has played a seminal role in the development of our knowledge of thermodynamics and classical mechanics. In classical mechanics entropy is a well defined mathematical concept. The concept of entropy has been applied to classically chaotic systems and detailed discussion of this are given by Gutzwiller [21]. In quantum mechanics, there is no definition for entropy that would tend to classical entropy in the limit $\hbar \rightarrow 0$. However, for mixed states described by density matrices ρ the Von Neumann entropy is defined as $S_{qm} = - \ \rho \ ln \ \rho$. Note that Von Neumann entropy for pure states is zero and reflects the perfect knowledge of the state. The information entropy, on the other hand, is a concept borrowed from Shannon's information theory [75] and has found wide applications in many branches of science [76].

In our work we shall discuss the information entropy of a quantum state, n, defined by,

$$\mathcal{S}_n^\alpha = - \int \int \ dx \ \ dy \ \ \rho_n^\alpha(x,y) \ \ \log \ \rho_n^\alpha(x,y) \tag{4.5}$$

where $\rho_n^\alpha(x,y) = \mid \Psi_n^\alpha(x,y) \mid ^2$. We also define information entropy in momentum space by,

$$\tilde{\mathcal{S}}_n^\alpha = - \int \int \ dp \ \ dq \ \ \tilde{\rho}_n^\alpha(p,q) \ \ \log \ \tilde{\rho}_n^\alpha(p,q) \tag{4.6}$$

where Fourier transform of coordinate space wavefunction is,

$$\tilde{\Psi}_n^\alpha(p,q) = \frac{1}{2\pi} \int \int \ dx \ \ dy \ \ e^{-\imath(px+qy)} \ \ \Psi_n^\alpha(x,y) \tag{4.7}$$

and $\tilde{\rho}_n^\alpha(p,q) = \mid \tilde{\Psi}_n^\alpha(p,q) \mid ^2$. The use of information entropy in many problems in physics and chemistry is well known. It had also recently been employed in the theory of quantum inference [77]. One of the earliest uses of an information entropy measure for distinguishing between regular and irregular classical trajectories in Hamiltonian systems was by Powell and Percival [78]. An information entropy measure for quantum eigenfunctions was also employed to study the degree of localisation for the kicked rotor [79]. Such a system was known to exhibit chaotic classical dynamics. Earlier such a measure had been employed to study localisation in a two dimensional solid

state model (see [79] and references therein). In this early work and in some of the subsequent work information entropy was calculated directly from the eigenvector coefficients. Let

$$\mathcal{I}_n^\alpha = -\sum_{j=1}^{M} \mid a_{nj}^\alpha \mid^2 \log \mid a_{nj}^\alpha \mid^2 \tag{4.8}$$

where a_{nj}^α are the normalised eigenvector coefficients mentioned in eq. (3.10) for the $n\ th$ eigenfunction of the system and which has M components, M being the dimensionality of the Hamiltonian matrix for the problem. This measure is obviously basis-dependent. This measure identifies the localised states by showing a pronounced dip in the information entropy curve corresponding to various localised states and was also visually confirmed. We will use this measure given by eq. (4.8) later to analyse the structure of localised states and its relation with stability of classical orbits. In fig. 4.3 information entropy in unperturbed basis eq. (4.8) is plotted against logarithm of the state number for quartic oscillator for $\alpha = 90.00$, for the range of states from 950 to 2000. The well pronounced dips correspond to channel localised states.

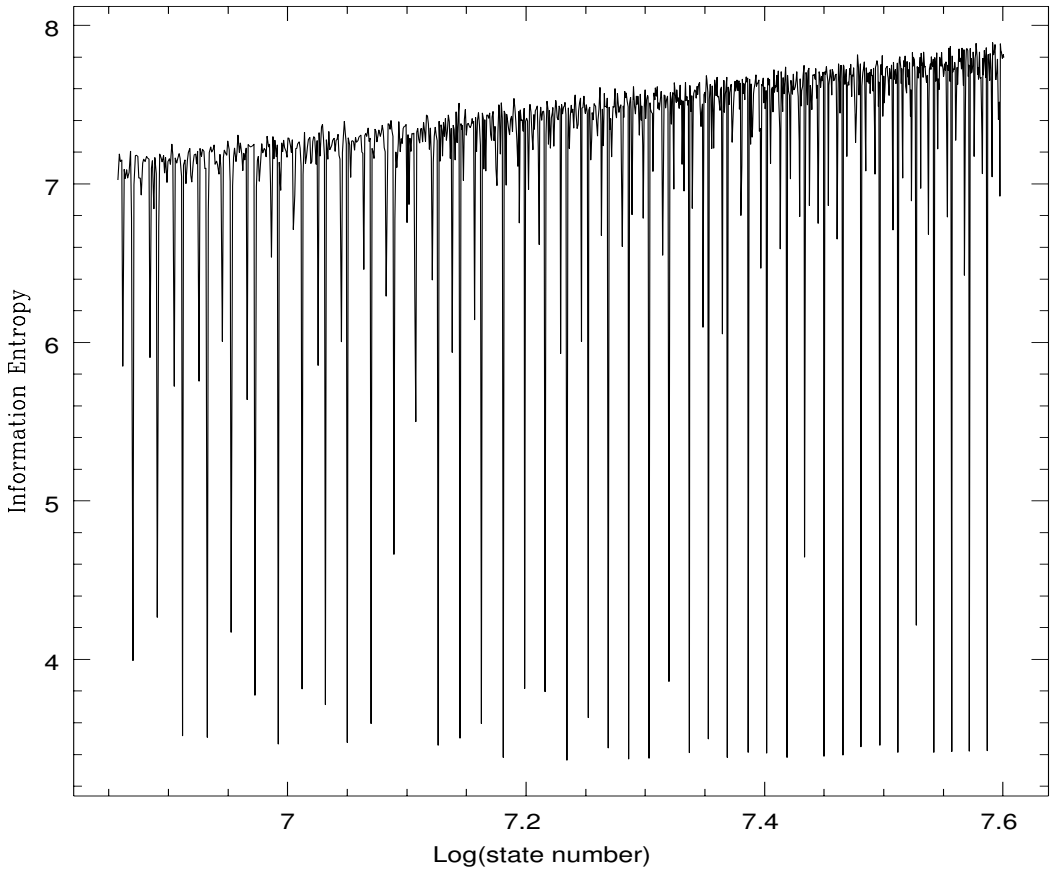

Figure 4.3: *Information entropy against the logarithm of the state number, in the unperturbed for state numbers from 900 to 2000 at* $\alpha = 90$.

Shadow states are marked by less pronounced dips and are sometimes ambiguous.

It must be emphasised that this measure picks out *only the channel localised states and no others*. In fig. 4.4 the information entropies defined in eqs. 4.5, 4.6 and 4.8 are plotted as function of logarithm of the state number. The following points emerge from the figs. 4.3 and 4.4, (i) all the three entropies show sharp minima for the same states which we visually and numerically identified as channel localised states, (ii) above about state number 300 an auxiliary minima appears soon after the main minima which we identified as the shadow localised states. In particular, we observe that the entropy measure picks out only the channel localised and shadow states and not those scarred by the other non-channel orbits. In fact, later we will see that though information entropy is a gross measure of localisation, it does distinguish between states which differ very little in their degree of localisation. The principle result of this section is that the localised states can be unambiguously identified by the information entropy measure.

4.3 Information Entropy and Random Matrix Predictions

At this point some remarks on statistics of eigenvectors is in order. It is now fairly well established from the pioneering work of Bohigas *et al* [26] that quantal energy level spacings distribution for classically chaotic quantum systems fall under three universality classes, determined by the symmetry properties of the Hamiltonian of the system. These level spacing distributions are modelled by appropriate ensembles from random matrix theory. For the Gaussian Orthogonal Ensemble (GOE), which models the fluctuation properties of the quartic oscillators, the eigenvectors are χ^2 distributed [80, 81]. In this case, the RMT prediction for information entropy [82] is expressed in terms of digamma function Ψ as,

$$S^{RMT} = \Psi(\nu D/2 + 1) - \Psi(\nu + 1) \tag{4.9}$$

where the parameter $\nu = 1$ for the Gaussian Orthogonal Ensemble and $\nu = 2$ and 4, respectively, for Gaussian Unitary Ensemble (GUE) and the Gaussian Symplectic Ensemble (GSE) of random matrix theory. For large D, where D is the dimensionality of the random matrices in the ensemble, the information entropy is,

$$\mathcal{S}^{GOE} \sim \log(\frac{D}{2}) - \frac{1}{D} - \Psi(\frac{3}{2}) \tag{4.10}$$

where D is large and is the dimensionality of the random matrices in the ensemble. In eq. (4.9) we find the expected entropy of *finite* dimensional GOE matrices. Thus we have to adapt the equation to an infinite dimensional Hilbert space in which the quantum mechanics of the oscillator resides. To this end we seek an *effective* dimensionality of a state, and we expect that the larger the energy the larger would be this

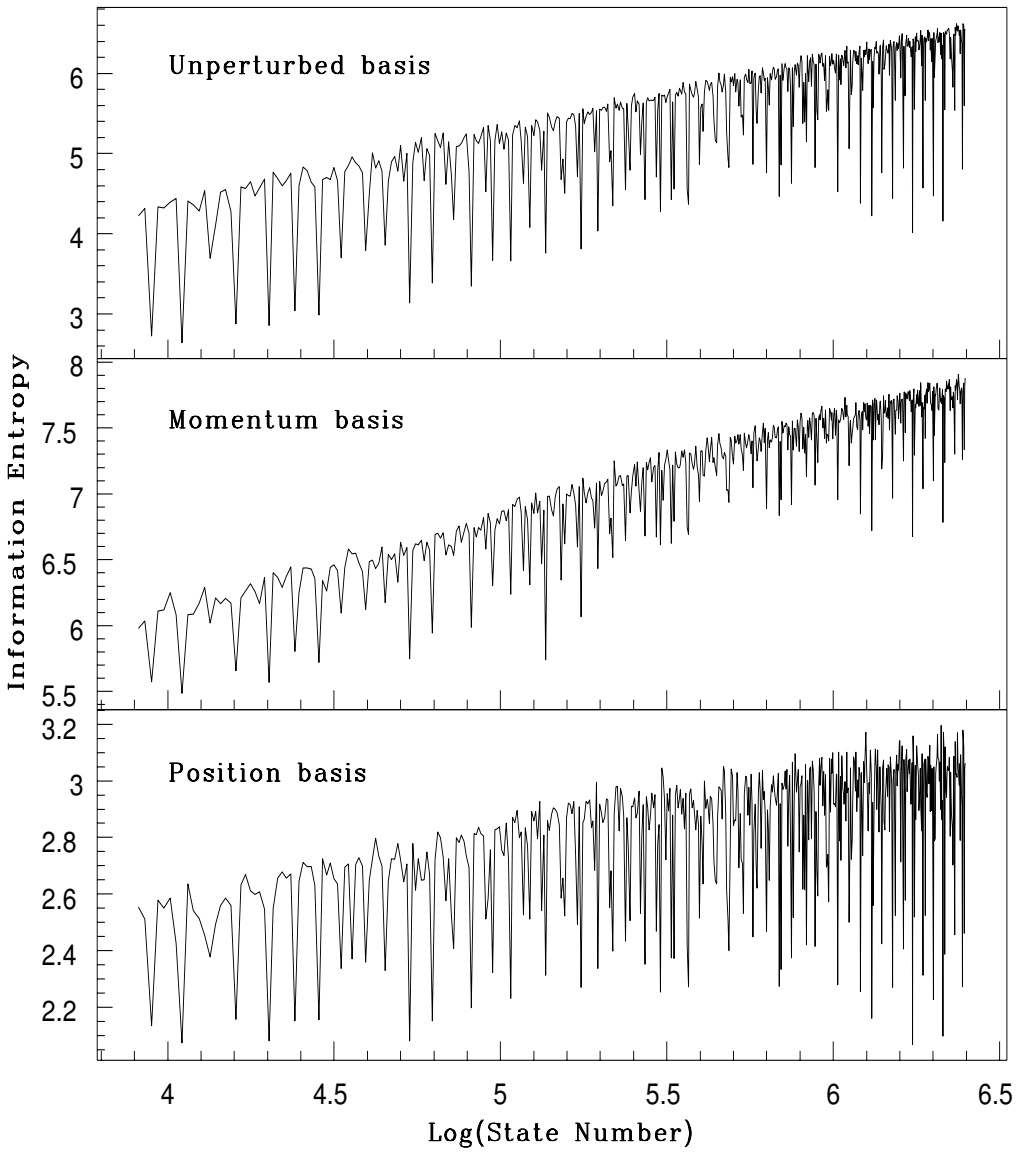

Figure 4.4: *Information entropy against the logarithm of the state number, in the unperturbed, momentum and position basis for state numbers from 50 to 600 at* $\alpha = 64.66$.

dimensionality. The simplest such measure is the integrated level density, that is the number of states whose energy is less than the energy of the given state. Thus we take D in eqs. (4.9,4.10) to be proportional to $N(E)$, the number of states less than a given energy E. There are several more elaborate means of finding such a dimension, like the participation ratio or simply the number of states which make up more than, say, 99% of the wavefunction etc. However we have found that these measures are on the average proportional to the state number, and seeking only to verify the logarithmic dependence on such a dimension we have used the most easily accessible. It is however clear that while measures such as the participation ratio are basis dependent, the integrated level density is not. We may note here that previous verifications of the above relation eq. (4.10) has been restricted to quantum maps in finite dimensional Hilbert spaces [83]. It has also been verified in the case of a globally chaotic system, namely the free motion on a compact surface of constant negative curvature [84].

In fig. 4.3, the information entropy curve reveals an almost linear behaviour as predicted in eq. (4.10) by the random matrix theory. In the unperturbed basis, the slope of the line fitted to the envelope of the information entropy curve is close to unity. However, we observed that in position and momentum basis the information entropy measure for the eigenfunctions does not exactly follow the RMT prediction, although the linearity is still evident. The failure of the entropies in the position basis to follow RMT like behaviour may perhaps be due to the uncountably infinite number of basis vectors in the Hilbert space as opposed to the countably infinite unperturbed basis states, thus complicating the issue of effective dimensionality. Integrated density of states could be one such measure of effective dimensionality. Another method is to employ the participation ratio defined as,

$$P_n = \frac{1}{\sum_{i=1}^{M} a_{ni}^4}$$

which gives the number of states that effectively participate in the building up of wavefunction [85].

Another more serious problem concerns the eigenvector distribution for the Hamiltonian systems in infinite dimensional Hilbert space, which classically exhibits mixed phase space. In such a case, it has not yet been conclusively verified that the eigenvector distribution follows RMT predictions. The distribution of eigenvector components $r =< \psi(x,y)|\Psi(x,y) >$ can be derived from the random matrix theory by only assuming that norm is the only eigenvector characteristic that is invariant under a group of canonical transformation. The general eigenvector distribution for the three universality classes of RMT is given by [80],

$$\chi_\nu^2(r) = \left(\frac{\nu}{2 < r >}\right)^{\nu/2} \frac{r^{\frac{\nu}{2}-1}}{\Gamma(\frac{\nu}{2})} \quad \exp\left(\frac{-r\nu}{2 < r >}\right) \tag{4.11}$$

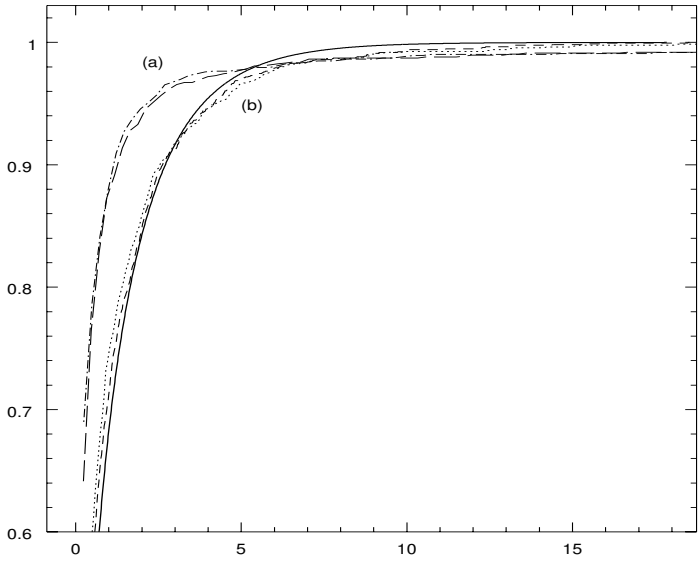

Figure 4.5: *The standard cumulative Porter-Thomas distribution (solid line). Curves (a) are for channel localised states (409 and 423 at $\alpha = 64.44$. In curve (b) dotted curve corresponds to a generic state and dashed curve corresponds to a strongly scarred state (state 552 at $\alpha = 64.44$.*

where $\nu = 1, 2$ and 4 for the GOE, GUE and GSE respectively. From the point of view of statistics, eq. (4.11) is the distribution of sum of squares of ν independent random variables $v_i, i = 1, 2, ...\nu$ drawn from Gaussian distribution with certain conditions on mean and variance. For the time-reversal symmetric, time-independent chaotic Hamiltonian systems the appropriate ensemble is the Gaussian Orthogonal Ensemble. The eigenvectors of the Hamiltonian matrices belonging to GOE class follow Porter-Thomas distribution obtained by putting $\nu = 1$ in eq. (4.11). There have been many studies of eigenvector distribution for finite dimensional systems and the validity of Porter-Thomas distribution has been verified. Yet the basis dependence of all such analysis is obvious. One way out is to select a generic and physical basis. We may take as the natural or 'generic' basis the unperturbed basis, or the position or the momentum basis. If in fact the eigenstates are truly random we expect there to be no difference in their statistical behaviour in any generic representation. In our case the unperturbed basis is one such possibility; however it is clear that it preferentially treats the channel localised states.

We performed the analysis for eigenvector distribution of several states in the quartic oscillator spectrum. Three cases arise, namely, (i) the eigenvectors of those eigenfunctions which are spread over all the classically accessible domain, (ii) the eigenvectors of strongly scarred states and (iii) the eigenvectors of the channel localised states. The fig. 4.5 shows the cumulative Porter-Thomas distribution for the square

of the eigenvector components normalised to unit mean given by,

$$f(r) = 1 - \text{Erf}\left(\sqrt{r/2}\right),$$

where Erf() is the standard error function. It is evident that the cases (i) and (ii) have similar eigenvector distribution, which is close to the standard Porter-Thomas distribution (solid line). The strongly scarred state is state no. 552 at $\alpha = 64.66$ (see the gallery for a configuration state plot), and the generic state is state no. 439 at the same value of α In this sense, even the strongly scarred state can be said to exhibit random matrix like distribution. However the eigenvectors of the channel localised states deviate considerably from the RMT prediction, as the fig. 4.5 shows. A similar result is also obtained recently by Muller *et. al* [68].

One reason for deviation from the RMT behaviour for the channel localised states could be that in the chosen basis states, the eigenvectors of the localised states have come in for a special treatment, which also makes these states outstanding in the entropy analysis. A physical basis that may distinguish the scarred states from the rest could be some coherent basis set, but not the position or momentum basis as indeed we have already demonstrated that the minima of the entropy in these basis states also correspond only to channel localised states [69].

4.4 Structure of Localised States

Even a cursory glance at the image plots of quartic oscillator localised states show that they might be structurally similar. Structural similarity of the localised eigenfunctions in the position representation is expected since the structure of the scarring periodic orbit (channel orbit) itself does not undergo any change due to variation in energy. This similarity must also be reflected in the more fundamental entities like the eigenvector coefficients or eigenfunctions in unperturbed basis given in eq. (3.10). In fig. 4.6(a) an eigenfunction in unperturbed basis $a_{m,j}$ is plotted as a function of j for a highly excited state at $\alpha = 90$. Since we have used 12880 basis states the index j, representing a doublet of quantum numbers, runs from 1 to 12880 in the x-axis, though not all them are shown in the figure. Figure 4.6(b) shows a highly excited channel localised state at the same value of α. We can take a closer look at the dominant peaks in fig. 4.6(b). This is shown in fig. 4.7, in which only the small window of basis states containing the principal contributions is shown.

We immediately recognise that for the channel localised state very few basis states contribute to building up of the wavefunction. The principal peak is made up of (N,0), (N,2), (N,4)... type of basis states, where the even integer N refers to the number of quanta of excitation for the motion along the channel. This integer N plays a significant role in the standard adiabatic approach applied to the quartic oscillator

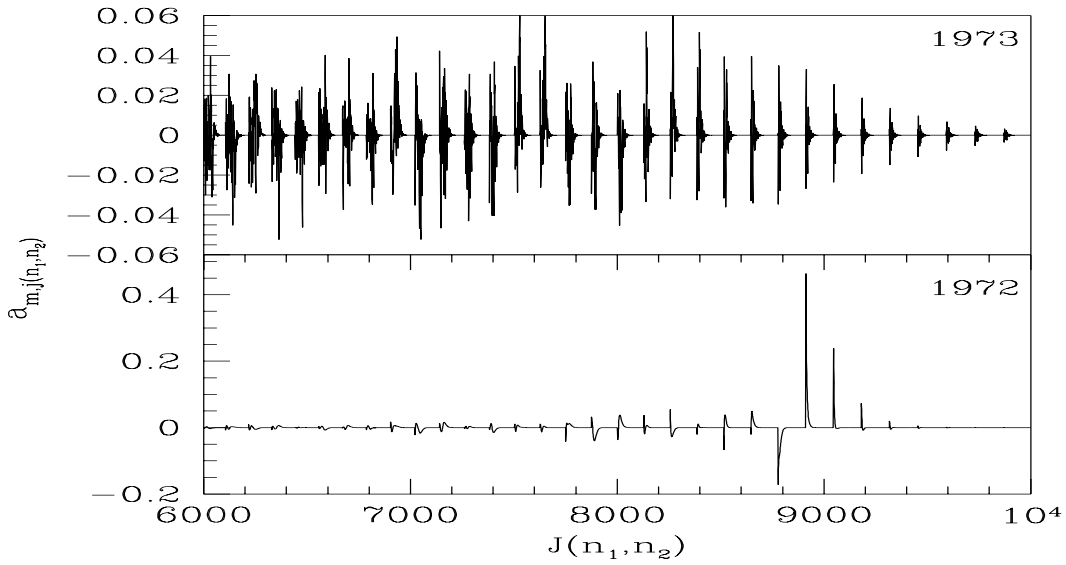

Figure 4.6: *The eigenvector coefficients* $a_{m,j(n_1,n_2)}$ *for (a) state number 1973 (top) and (b) state number 1972 (bottom) , both at* $\alpha = 90.0$.

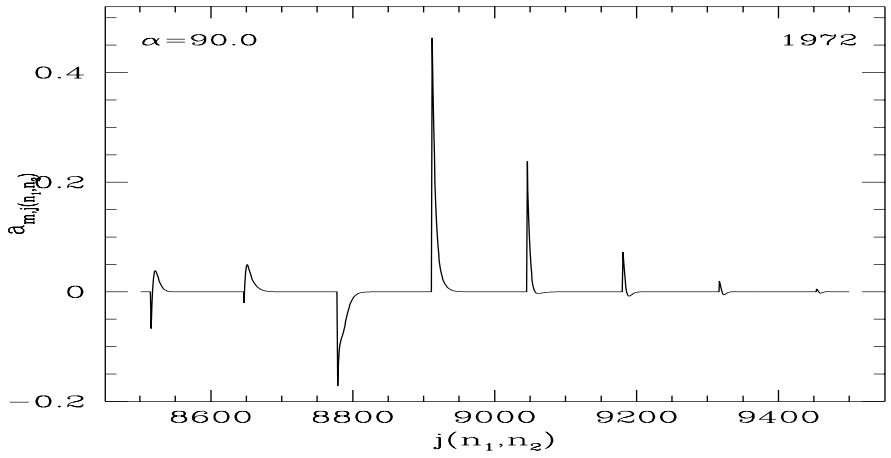

Figure 4.7: *An enlarged view of the principal eigenvector contributions for the localised state 1972 at* $\alpha = 90.0$.

to estimate the energies of the localised states. This will be dealt in the next section. We observed that the pattern in fig. 4.7 is qualitatively generic for all the channel localised states. For instance, in fig. 4.8 we have the eigenvectors of localised states in the unperturbed basis for a range of parameters $\alpha = 88.0$ to 96.0. In all these cases, the principal peak corresponds to $n_1 = N = 252$ (note the change of notation from n_1 to N). Indeed, the structure of eigenfunction in unperturbed basis is universal in character for all the channel localised states. As we shall see later, other similar potentials with channels also have this universal character for their localised states.

First we state the result and then provide the evidence. It has two parts ; (i) our numerical results show that the channel localised states in the unperturbed basis are dominated by a few peaks whose falloff is exponential in nature in the quantum number of the motion perpendicular to the direction of the channel; (ii) and further that the degree of localisation is related to the stability of the channel periodic orbit.

The first contention (i) is taken up in this section. As is pointed out, the integer N corresponds to the quantum number of the motion along the channel. For the localised states, there are about four to five dominant peaks in the plot of eigenvector components (see fig. 4.8) which make significant contribution to build up the wave-function. The falloff of these dominant peaks, as a function of n_2, is on an average exponential, where n_2 is an even integer representing the quantum number for the excitation perpendicular to the channel motion. In fig. 4.9(a) we plot $\log(a_{m,j(N,n_2)})$ as a function of n_2 for five highly excited states whose principal contributions come from $N = 252$ for values of parameter ranging from $\alpha = 88$ to 96. Note that these five are the same states shown in fig. 4.8. The good straight lines obtained in figs. 4.9(b) shows that the fall is indeed exponential. The next dominant peak with contributions coming mainly from $(N+2,0),(N+2,2),(N+2,4)....$ basis states also provides an evidence of exponential localisation. This is shown in fig. 4.9 as a dotted line. However, for the third peak, corresponding to $(N+4,0)$, the values of $a_{m,j}$ fall within the accuracy of our calculation and hence, although unequivocal conclusions cannot be drawn, we expect the fall to be exponential as well.

The $m\ th$ localized eigenfunctions may thus be written as,

$$\Psi_{m(n,l)} = \sum_k A_k \exp(-n/\xi_k)\delta_{N+k,l} \tag{4.12}$$

where n and l are quantum numbers that make up the basis state. A_k describe the amplitude of the peaks and only very few of them are appreciably different from zero. The ξ_k, the localization lengths are the inverse of the slopes of the straight lines such as fig. 4.9.

The result presented above is the first observation of exponential localisation in smooth chaotic systems. Anderson's model in condensed matter physics for the

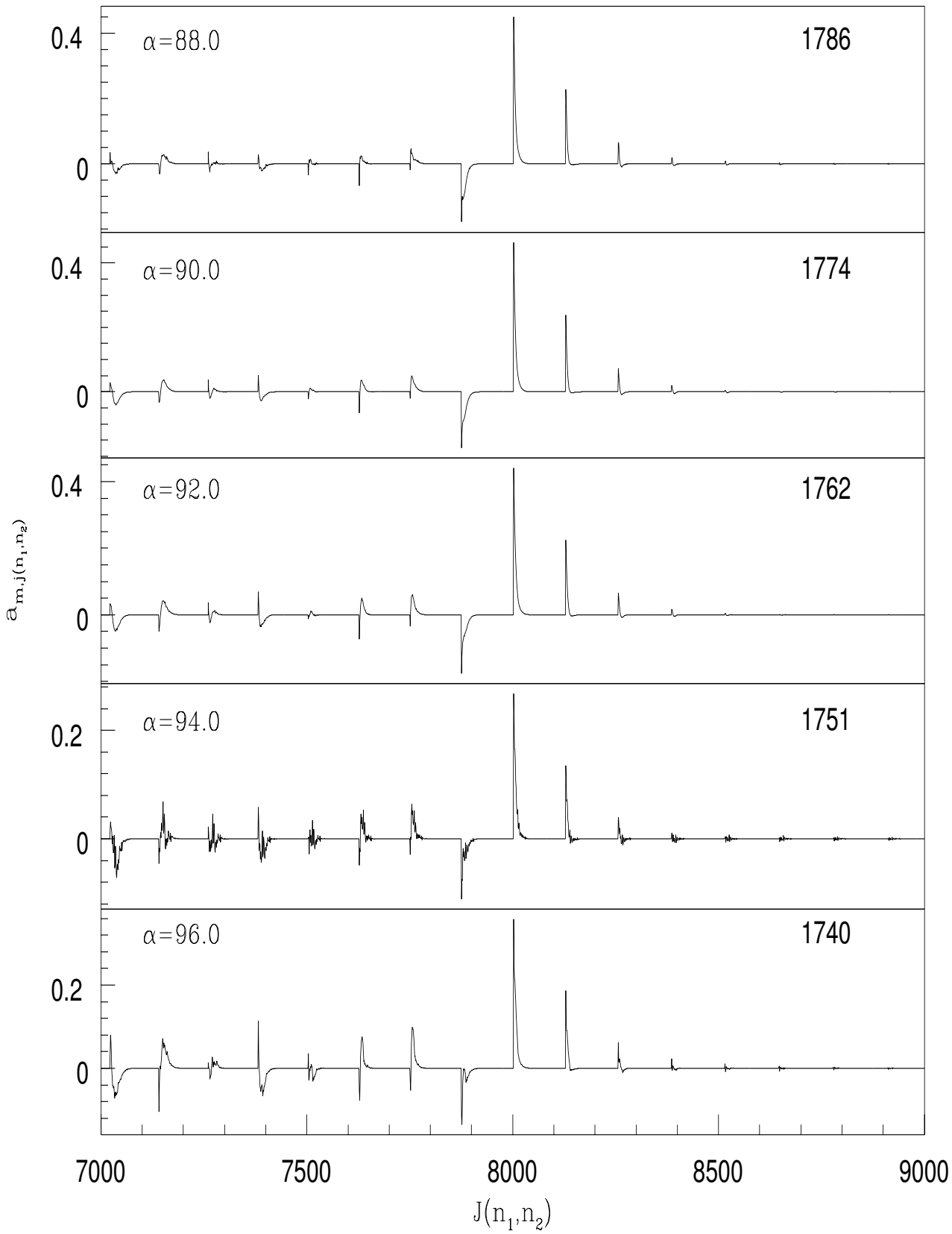

Figure 4.8: *The common eigenvector characteristics of all the channel localised states for a range of parameters. (* $N = 252$ *for all the states shown in this figure.*

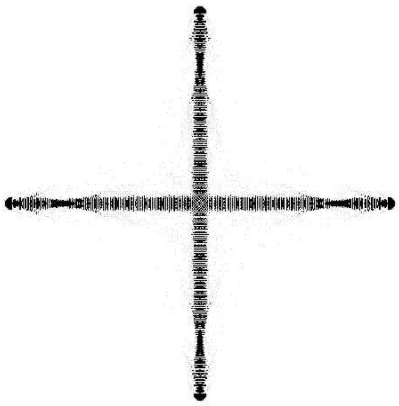

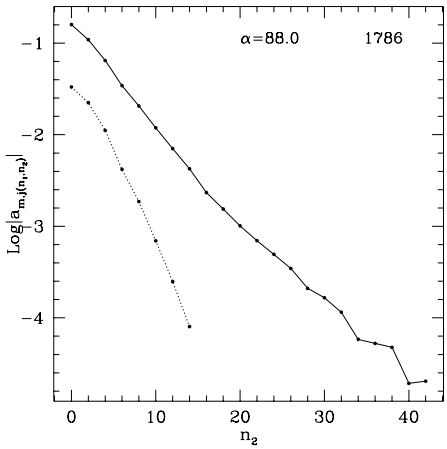
α=88.0
1786
Log|a_{m,j(n1,n2)}|
n2

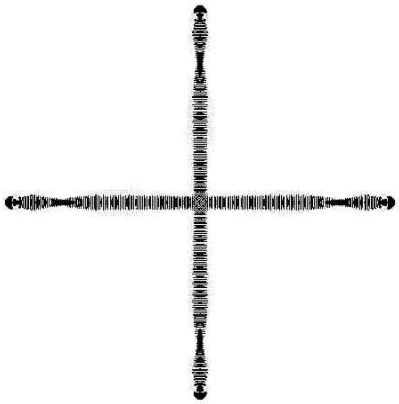

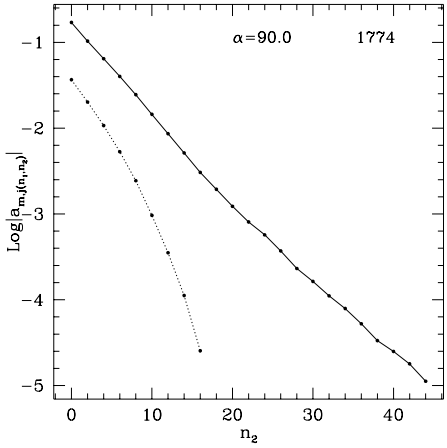
α=90.0
1774
Log|a_{m,j(n1,n2)}|
n2

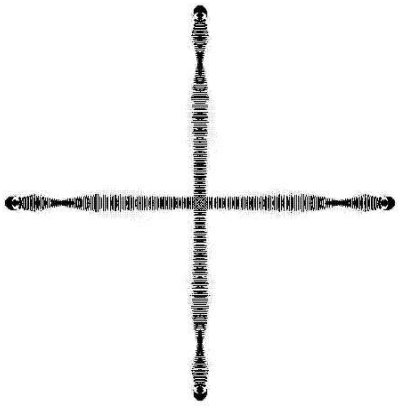

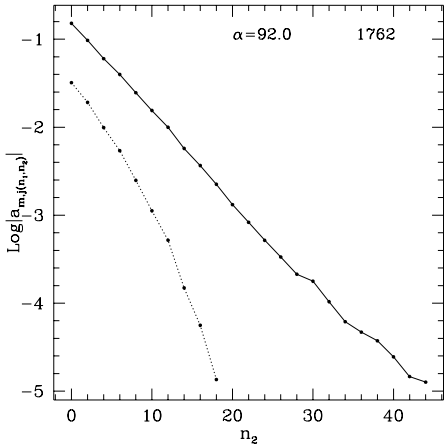
α=92.0
1762
Log|a_{m,j(n1,n2)}|
n2

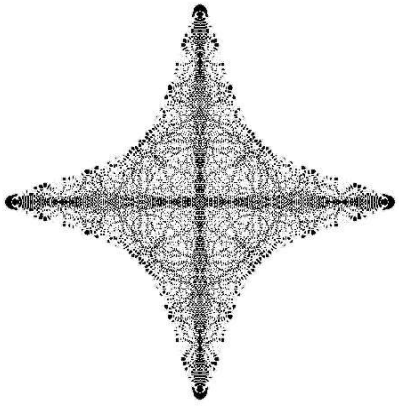

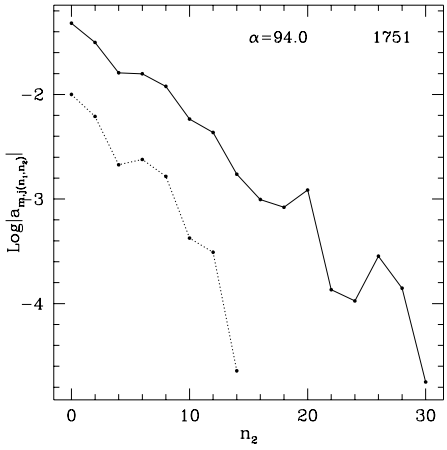
α=94.0
1751
Log|a_{m,j(n1,n2)}|
n2

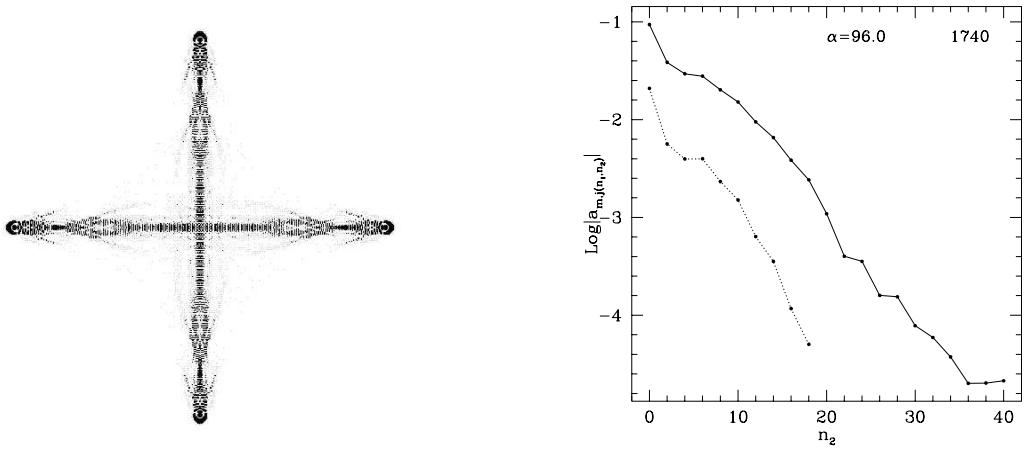

Figure 4.9: The localised states in coordinate representation and the exponential localisation for several values of α. For all the states in this figure principal peak corresponds to $(N = 252, 0)$. Note that $\alpha = 94$ is an avoided crossing. (see text for more details). All the images have same colour map. Inside the plot, α and the state number are given.

motion of a charged particle in series of potential wells with random depths is a well-known instance for which exponential localisation is rigorously established. In the context of quantum chaos, it has been established that the eigenstates of time-dependent systems, like the kicked rotor, are also exponentially localised [79]. Since kicked rotor has been mapped to the Anderson's model the exponential localisation follows as a consequence though with the important difference that the potential in the kicked rotor is not random [37]. To emphasise that the localisation in the kicked rotor arises from the dynamics rather than from randomness in the potential, this variety of localisation is termed as dynamical localisation. From the point of view of exponential localisation, Feingold [70] has discussed the differences and properties related to the structure of Hamiltonian matrices for time-independent and kicked systems.

Why not exponential localisation for other scarred states? We believe that the answer lies in the fact that; (a) the basis in which there is exponential localisation belongs to the Hamiltonian, namely eq. (2.3) with $\alpha = 0$. The channel orbit that scars these eigenstates is also a valid orbit for the unperturbed system. (b) the stability of such an orbit is high, the channel orbit never becomes very unstable, however large the nonlinearity. For instance the 45^o straight line periodic orbits could be exponentially localised in the 45^o rotated unperturbed basis, but this orbit becomes extremely unstable thereby creating complex states in which other orbits also contribute to the scarred state. It is important to recognise that though intuitively one does expect the localised states to have lesser spread and a faster fall in the space of basis states, the

fact that the fall should be exponential is not obvious.

In this section, we have provided evidence for exponential localisation of eigenfunctions in the unperturbed basis for a smooth Hamiltonian system. The question of connection between the stability and the degree of localisation will be taken up in a later section.

4.5 Adiabatic Approaches for The Quartic Oscillator

In this section we will discuss certain adiabatic methods that lead to further understanding of the role of quantum number N, that appeared in the previous section, in estimating the energies of these localised states. The Born-Oppenheimer approximation [86] in molecular physics is a well-known example of adiabatic approximation in which we exploit the fact that nuclear motion is much slower than the electronic motion. Hence the electronic motion can be be treated separately under the assumption that the nucleus is at rest. This leads to factoring of the molecular wavefunction as, $\psi = \psi_{elec}\psi_{nuclear}$ with consequent simplification. The theories on chemical-reaction dynamics also use the adiabatic techniques [87].

The basic premise of the classical adiabatic method in two degrees of freedom is that the time scales of motion in the two perpendicular modes are vastly different. For instance, in the specific case of coupled quartic oscillator, the frequency of the motion along the channel (say, x axis) is assumed to be slower than the frequency of the motion perpendicular (y axis) to it, resulting in the perpendicular action being an adiabatic invariant for the motion along the channel. This is not true in general since the frequencies of motion for both the modes are the same on an average when the particle wanders all over the classically accessible configuration space. However, the local separation of time scales holds good only in a restricted case when the particle enters one of the channels of the potential, resulting in an increase in the instantaneous frequency of motion along y direction. We first treat the fast motion in y direction retaining coordinate variable x as a parameter and then a locally integrable Hamiltonian is obtained for the channel motion which is then quantised to obtain the energy eigenvalues. We will implement this plan of action to derive an approximate expression for the energy of the localised states.

Using the Hamiltonian in eq. (2.11), we average over the fast motion first by taking $p_x = 0$. Then eq. (2.11) becomes,

$$H_y(x, \alpha) = p_y^2 + y^4 + (\alpha x^2)y^2 = E_y \tag{4.13}$$

where x is also treated as a parameter. The classical action associated with the y motion,

$$J_y(x, \alpha) = \int_0^{y_{max}} \sqrt{E_y(x, \alpha) - y^4 - \alpha x^2 y^2 dy} \tag{4.14}$$

becomes the adiabatic invariant for the channel motion in x direction and y_{max} is the positive turning point in y for a given x. Now since the excursions in y direction is small, we assume $y \sim 0$. Hence, under this approximation, J_y is the action of a harmonic oscillator and 4.14 can be easily evaluated to give,

$$J_y(x,\alpha) = 2\pi \frac{E_y}{\sqrt{\alpha} \mid x \mid} \tag{4.15}$$

Then in the classical adiabatic approximation, Hamiltonian for x motion can be written as,

$$H_{ad} = p_x^2 + x^4 + J_y(x,\alpha)\frac{\sqrt{\alpha} \mid x \mid}{2\pi} = E_{ad} \tag{4.16}$$

and its corresponding action is given by,

$$J_x = 4\int_0^{E_{ad}^{1/4}} dx \quad \sqrt{E_{ad} - x^4 - \sqrt{\alpha}x\frac{J_y}{2\pi}} \tag{4.17}$$

From here we go through a series of approximations to obtain a locally integrable Hamiltonian to describe the channel motion. By subjecting this approximate Hamiltonian to a semiclassical quantisation, we obtain a WKB-like formula for the energy of the localised states. First in the series of approximations is the following. The upper limit for the integration in eq. (4.17) is not the turning point of the adiabatic Hamiltonian eq. (4.16), but it shall be the turning point of the Hamiltonian given by, $H_q = p_x^2 + x^4 = E$, namely $\pm E^{1/4}$.

$$J_x \simeq 4\int_0^{E^{1/4}} \sqrt{(E - x^4)}\sqrt{1 - \frac{\sqrt{\alpha}\ J_y\ x}{2\pi(E - x^4)}}\ dx$$

We do a binomial expansion of the second term to obtain,

$$J_x \simeq 4\ \int_0^{E^{1/4}} \sqrt{(E - x^4)}\ dx - 4\ \int_0^{E^{1/4}} \frac{\sqrt{\alpha}\ J_y\ x}{4\pi\sqrt{E - x^4}}\ dx$$

Both the integrals can be easily performed to give,

$$J_x \simeq 4C_1 E^{3/4} - \frac{J_y\sqrt{\alpha}}{2} \tag{4.18}$$

where $C_1 = \frac{\sqrt{\alpha}\Gamma(1/4)}{8\ \ \Gamma(7/4)}$. Then the integrable Hamiltonian is a function of actions,

$$H_{ad} \simeq \left(\frac{1}{4C_1}\right)^{4/3}\left(J_x + \frac{\sqrt{\alpha}J_y}{2}\right)^{4/3} \tag{4.19}$$

Note that under this approximation, we have a locally integrable Hamiltonian, exhibiting the usual torus structure in phase space. The approximate Hamiltonian is plagued by non-analyticity at the origin, i.e at $|x| = 0$. This leads to a mismatch between exact classical solution and adiabatic solution in the vicinity of the origin since all the tori of the adiabatic Hamiltonian touch one another at the origin leading to dynamics crossing over from one torus to another. On the other hand, in the quantum

regime, the adiabatic potential surfaces suffer from nonanaliticity at the origin. Due to this pathological problem the adiabatic approximation is not valid near the origin, as shown graphically in ref. [88]. Hence we can expect that under the conditions of channel motion, where the particle will spend most of its time far away from the origin, a semiclassical WKB quantisation will produce good estimate for the energy of the localised states. We proceed further to do this.

The semiclassical WKB quantisation of the Hamiltonian in eq. (4.19) is straightforward ($\hbar = 1$),

$$J_x = \left(n_1 + \frac{1}{2}\right) 2\pi \qquad\qquad J_y = \left(n_2 + \frac{1}{2}\right) 2\pi \tag{4.20}$$

By quantising the actions thus we get,

$$E(n_1, n_2) \simeq \left(\frac{1}{4C_1}\right)^{4/3} \left[(n_1 + \frac{1}{2})2\pi + \frac{\sqrt{\alpha}}{2}(n_2 + \frac{1}{2})2\pi\right]^{4/3} \tag{4.21}$$

In fact, this expression can be used to estimate the energies of the localised states. However to obtain a familiar WKB-like relation we perform one more binomial expansion as follows.

$$E(n_1, n_2) \simeq \left(\frac{\pi}{2C_1}\right)^{4/3} \left(n_1 + \frac{1}{2}\right)^{4/3} \left(1 + \frac{\sqrt{\alpha}\ (n_2 + 1/2)}{2\ (n_1 + 1/2)}\right)^{4/3}$$

$$E(n_1, n_2) \simeq b_1\ (n_1 + 1/2)^{4/3} + \frac{2\ b_1}{3}(n_2 + 1/2)\sqrt{\alpha}(n_1 + 1/2)^{1/3} \tag{4.22}$$

where

$$b_1 = \left(\frac{4\ \sqrt{\pi}\ \ \Gamma(7/4)}{\Gamma(1/4)}\right)^{4/3} = 2.18507 \tag{4.23}$$

We started out with the aim to further understand the role of N in section 4.4. The even quantum number n_1 appearing in eq. (4.20) is identical to N appearing in the previous section. To use the same old notation, we use N instead of n_1 in equations appearing further ahead. For the channel localised states, $n_2 = 0$ and hence the final adiabatic energy formula reduced to,

$$E_N(\alpha) \simeq b_0\sqrt{\alpha}\left(N + \frac{1}{2}\right)^{1/3} + b_1\left(N + \frac{1}{2}\right)^{4/3} \tag{4.24}$$

where $b_0 = b_1/3 = 0.728356$. This approximate expression for the energy has been derived as a consequence of the adiabatic breakup of channel motion and gives a good estimate for the energy of the localised states. In fig. 4.10(a) we show the difference ($E_{ad} - E_{QM}$) between the adiabatic energy (E_{ad}) estimated by the eq. (4.24) and the actual energies (E_{QM}) obtained by diagonalisation. In this case we use the value of constant b_0 given by eq. (4.23) and b_1 as given above. This figure shows that N dependence is still present and hence there is continuous deterioration of predicted energy values. Hence, to obtain a better estimate of the energies of localised states, the

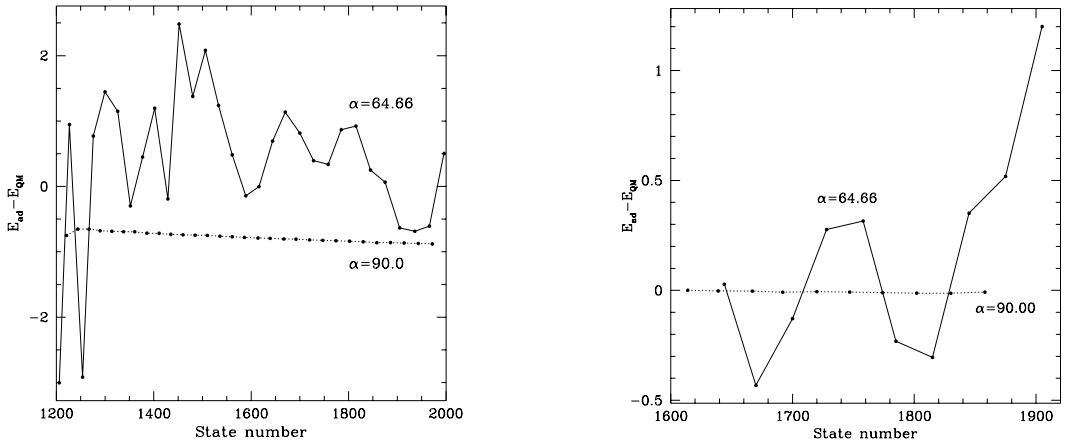

Figure 4.10: *The adiabatic approximation in graphical form. (a) E_{ad} and constants obtained from the eq. (4.24) and 4.23. (b) The E_{ad} is obtained by fitting to energy levels of localised states.*

constants b_1 and b_0 were obtained by fitting the eq. (4.24) to the actual energies of the localised states. For plotting the fig. 4.10(b), we used 10 localised states between the state numbers 1300 to 1600 for fitting to eq. (4.24). Using fitted values of constants, we estimated the adiabatic energies and the fig. 4.10(b) shows the difference between the energies thus estimated and the exact energies.

This figure shows that at $\alpha = 90$, the energy estimated by eq. (4.24) using the fitted values for b_0 abd b_1 agrees well with the actual energies, but at $\alpha = 64.66$, the agreement is not as good, though the estimate does not significantly from the mean level spacing which is about unity. Wherever the difference ΔE exceeds one, at those points we can invariably find an avoided crossing. The table below shows the constants obtained by regression.

	$\alpha = 64.66$	$\alpha = 90.0$	From formula 4.24
b_0	0.66976	0.72991	0.72835
b_1	2.18660	2.18546	2.18507

This difference in the accuracy of the energy estimates based on the formula eq. (4.24) is related to the stability of the underlying scarring periodic orbit. In fact, as the table above shows, the values of constants b_0 and b_1 obtained by fitting are close to the theoretically predicted values for $\alpha = 90.0$ but not so for $\alpha = 64.66$. We recall that at $\alpha = 90$, the channel orbit is marginally stable whereas at $\alpha = 64.66$ the channel orbit is passing through a window of instability. Our results, including the figs. 4.10(a) and 4.10(b) and the Table above strongly indicate that the energy formula in eq. (4.24) performs well when the underlying scarring orbit is at the point of pitchfork bifurcation ($\alpha = 90$ is one such point) and is less accurate when the

orbit moves away from this parametric value. We have noticed this behaviour at other values of the parameters too. Based on these observations, we expect that the stability exponent should also enter as a parameter in the adiabatic energy formula. In fact, an extension of Bohr-Sommerfeld quantisation condition for chaotic systems based on periodic orbit expansion of Gutzwiller includes the stability λ of the classical periodic orbit γ as a parameter [89]. For a linearised Poincaré return map P around γ, P is a 2 x 2 matrix and has eigenvalues $e^{\pm\lambda}$ if the orbit is unstable. Then, the quantisation condition is given by,

$$\int_\gamma p \;\; dq = [2\pi n_x - (n_y + 1/2)i\lambda + \nu\pi/2]\hbar \tag{4.25}$$

where ν is the number of conjugate points of the periodic orbit. As Voros argues [89], this extended quantisation condition yields fairly good estimates for the energy levels in the case when the classical orbit is stable in which the eigenfunctions tend to concentrate on this orbit as $\hbar \to 0$. But when the classical orbit is unstable, this formula gives rise to imaginary eigenvalues. Hence in the unstable case, eq. (4.25) cannot be usefully interpreted as a quantisation condition.

Though the quantum and semiclassical adiabatic methods provide good energy estimates in this case, they do not separate the eigenvalues coming from different irreducible representations. For a fair comparison, the eigenvalues from this approach must be tallied with the average quantum eigenvalues from different irreducible representations. Incorporating discrete symmetries in the adiabatic approach is still an open problem. However, Sinha and Sheorey [90] have used an adiabatic energy formula similar to eq. (4.24) for coupled quartic oscillator. By fitting the exact quantal energies from A_1 irreducible representation to their adiabatic formula and determining the constants they were able to predict fairly accurately the energies of a group of localised states in A_1 symmetry in the range of state numbers from 400 to 500. In the last few years, there have been few attempts at applying adiabatic methods to different systems. The quantum mechanically untamed potential $V(x, y; \alpha) = \alpha x^2 y^2$ has been studied in cartesian adiabatic approximation [52]. Ring type localisation in quartic oscillator has been explained using the polar coordinate adiabatic breakup [91].

The adiabatic treatment involving semiclassical quantisation, by its very nature, presupposes the existence of a series of particular type of scarred states. However, our own experience with the computation and visualisation of nearly 2000 eigenfunctions for various α values amply confirms a series for channel states but does not show any evidence for a series of ring states. One reason for the absence of clean ring states in the deep semiclassical regime could be instability of the underlying periodic orbits. It may be remarked that the previous studies rely on low-lying eigenfunctions which do not show many avoided crossings and inspite of it being such a simple spectrum in

the energy region considered, the identification of ring-states seems, at times, to be subjective. The highly excited region exhibits a large number of avoided crossings and many localised states stand on them and the adiabatic approach cannot unambiguously identify such states which differ in energy by less than mean energy spacing. We show one such case in fig. 4.11, for $\alpha = 90.0$. Since the semiclassical spectrum

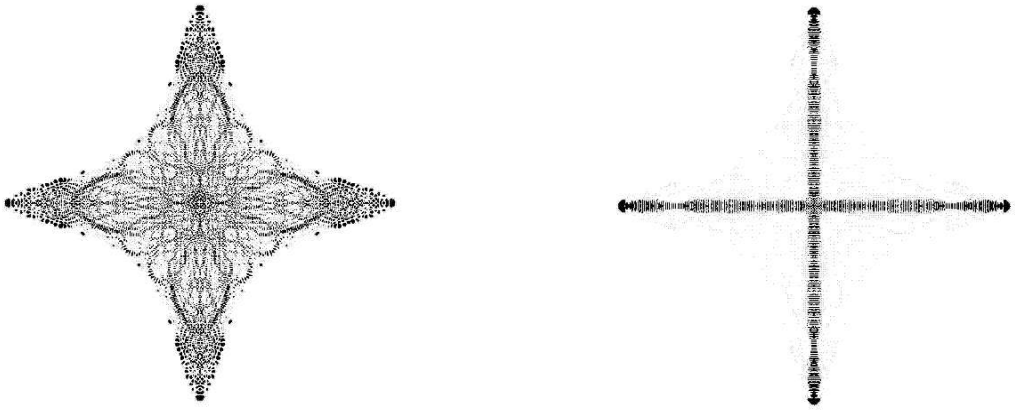

Figure 4.11: *Configuration space intensities for two consecutive states for* $\alpha = 90.0$. *The states are (a) 1857th state with energy 3642.9626 and (b) 1858th state with energy 3643.0294. Note that state number 1858 is a localised state. The difference in their energies is 0.0668*

has a large number of such cases, it becomes necessary to visualise eigenfunctions to confirm the results obtained by this approach. In this sense, the adiabatic approach provides more of a qualitative insight rather than precise quantitative results. Hence we emphasise that, at the moment, the visual methods have to necessarily complement these other techniques for correct interpretation of these approximate methods.

4.6 Localisation and Stability

We now take up the second contention regarding the connection between the degree of localisation and stability of the classical orbit The term 'degree of localisation' is used in the sense of the extent of localisation or the effective spread over the basis states, somewhat similar to the localisation length, and we use the information entropy as a measure of the degree of localisation. In fact, quite surprisingly we found that even a gross measure like the information entropy is quite sensitive to different degrees of localisation.

The channel periodic orbit loses stability through a pitchfork bifurcation (Tr $J(\alpha) = -2$) at $\alpha = 90.0$ while giving birth to two other stable orbits. The eigenvectors of the localised states seems to be affected by the bifurcation in its scarring orbit. The fig.

4.9 shows the localised eigenstates in coordinate representation and its corresponding $\mathrm{Log}(a_{m,j(N,n_2)})$ for the first two dominant peaks. For the dominant peak (shown as solid line in fig. 4.9) $N = 252$ and for the next dominant peak (shown as dotted line in fig. 4.9) $N = 254$. The third dominant peak (not shown in the figure) will have $N = 254$ and so on.

We notice from fig. 4.9 that we get the best exponential behavior at $\alpha = 90.0$ and it progressively moves away from exponential behavior as we explore the parameter regions in which the channel orbit also becomes progressively unstable. This figure also provides a striking visual evidence for the above statement. It shows five wavefunctions for a range of α values at which the channel orbit is first stable ($\alpha = 88.0$ case) and then undergoes a pitchfork bifurcation ($\alpha = 90.0$ case) and then enters the unstable regime (for example, $\alpha = 96.0$). The wavefunction at $\alpha = 90.0$ is compact and has almost collapsed on to the underlying periodic orbit in comparison with the wavefunction at $\alpha = 88.0$ and $\alpha = 96.0$. At $\alpha = 94.0$, the wavefunction shows much more spread than at $\alpha = 96.0$. This is another instance of an avoided crossing leading to exchange of characters between two the wavefunctions. Hence the 1751st state with energy 3533.6064 at $\alpha = 94.0$ appears to be an anamoly. The state number 1752 at $\alpha = 94.0$ with energy 3533.9782 is shown in the gallery of pictures. These two states differ in energy by 0.3718 which is less than the mean spacing of unity. Thus the wavefunction has more spread at parametric values not associated with the pitchfork bifurcation of the scarring orbit.

All the localised states at $\alpha = 90.0$ show a nearly perfect exponential fall. But as the parameter moves away from the point of pitchfork bifurcation, i.e $\alpha = 90.00$, the exponential fall gets distorted for all the localised states, though it still remains exponential on an average, similar to exponential localisation in kicked rotor. In order to see that the best and compact localisation of all the channel localised states occurs at the point of pitchfork bifurcation ($\alpha = 90.0$), we do the following. We calculated the average information entropy for a particular α by taking the mean of information entropies, $< S_\alpha >= \sum_\sigma \mathcal{S}_\sigma^\alpha / k$ for a group of k localised states represented by σ within some energy range. Strictly speaking this quantity may not be physically meaningful, but it is a coarse-grained value that would reveal the average trend in the degree of localisation. The participation ratio also shows an identical trend. For our purposes, we have chosen a large energy range that contains about 1000 eigenstates including 40 localised states in it for each value of the parameter α. The plot of $< S_\alpha >$ in fig. 4.12 shows that the average information entropy shows a minimum at $\alpha = 91$. Even this averaged measure reflects the trend observed in the stability oscillations of the channel orbit in the vicinity of $\alpha = 90.0$; although the exact minimum of the entropy seems to be slightly removed from this point of bifurcation. A tentative explanation

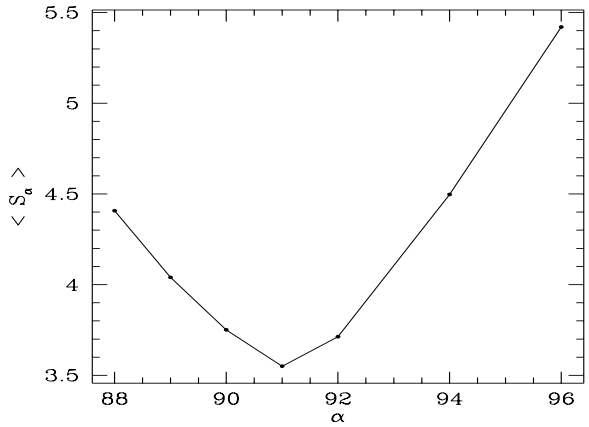

Figure 4.12: *The variation of average entropy* $< S_\alpha >$ *as a function of the parameter* α.

of this is provided in the observation that exactly at the point of bifurcation, the region around the channel orbit is locally flat while just after the bifurcation although the channel orbit has lost stability and become hyperbolic there are two neighboring newly created stable orbits that provide the region with enhanced overall stability. Thus an initial wavepacket launched in the channel would spread out slower immediately after the bifurcation thereby enabling relatively sharper localization. Moving away from the point of bifurcation the stable orbits move away from the channel orbit and thus their stability is of no consequence and the wavefunctions relatively delocalize. All these results in totality imply a strong correlation between the stability of channel orbits and degree of localisation, and also are indicative of the dominant role played by the channel orbit. In a similar spirit, though not quite the same, Atkins and Ezra [92] have qualitatively studied the effect of pitchfork bifurcation of the diagonal classical periodic orbit on the eigenstates of the quartic oscillator. This orbit is always unstable beyond a particular value of the parameter. The bifurcation of the diagonal orbit is shown to be associated with the spread in the eigenstate in configuration space transverse to the 45^o orbit considered. However, they have confined themselves to low-energy spectrum only.

At this point, to study this phenomena further, we take up the perturbed harmonic oscillator given by the Hamiltonian,

$$H_p(x,y) = \frac{p_x^2}{2} + \frac{p_y^2}{2} + \frac{x^2}{2} + \frac{y^2}{2} + \beta x^2 y^2 \tag{4.26}$$

where β is the parameter; we have taken $\beta = 0.1$. This is a non-homogeneous system and hence for a fixed value of β, energy E acts as the chaos parameter. For the parameters as fixed above, the system is dominated by chaotic trajectories beyond energy 25.0. By substituting, $q' = \sqrt{\beta}q$, where q is the phase-space variables (x, y, p_x, p_y), it

can be easily shown that the scaled parameter is $\epsilon = \beta E$. Hence the onset of chaos and other classical properties can be studied as a function of the scaled parameter. Pullen and Edmonds [93] have studied this system and concluded that this exhibits the properties conjectured by Percival for an irregular system. Anchell's study of this system concentrates on the correspondence between classical Poincaré section and quantum phase-phase distribution like the Husimi [94].

However, for our purposes, we will be interested in the channel orbit, its stability properties and their relation to the quantum eigenfunctions. This potential also allows for a channel motion and the stability of the channel orbit oscillates as a function of the parameter β. The stability curve is shown in fig. 4.13 below. To study the

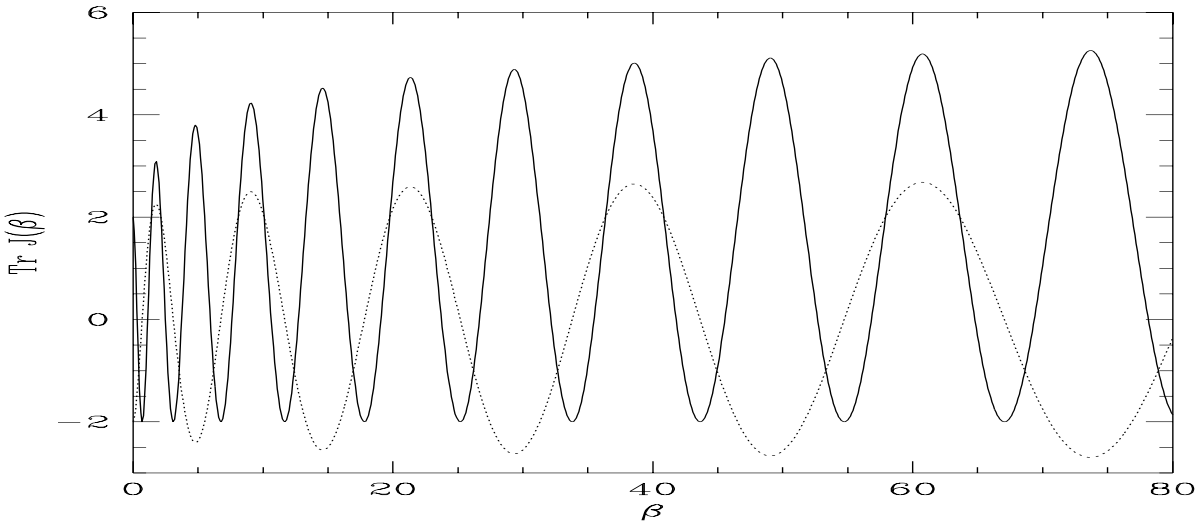

Figure 4.13: *The stability curve for the channel orbit of the perturbed harmonic oscillator. The solid curve is for the full Poincaré map and dotted curve for the half map.*

stationary states of this system, we numerically solved the Schroedinger equation in the unperturbed basis, using the eigenfunctions of the two-dimensional harmonic oscillator, ($\beta = 0$ case of eq. (4.26)), as the basis states. Since this also has the C_{4v} symmetry, the wavefunctions are given by

$$\Psi_n(x, y) = \sum_{j=1}^{\infty} b_{n,j} \psi_j(x, y) \tag{4.27}$$

where $\psi_n(x, y)$ now will represent the linear combination of one-dimensional harmonic oscillator eigenfunctions as per the requirement of A_1 representation of C_{4v} group and $b_{n,j}$ are the eigenvectors in unperturbed space, the expansion coefficients. From now on, all the results presented will be for the perturbed harmonic oscillator given by eq. (4.26), unless otherwise specified. We computed about 2000 eigenstates by

diagonalising matrices of order 12880 and calculated the information entropy for each state, which will used later.

First we plot the Poincaré sections at two different energies corresponding to regular and predominantly chaotic motion. At energy $E = 1$ the dynamics is mostly regular

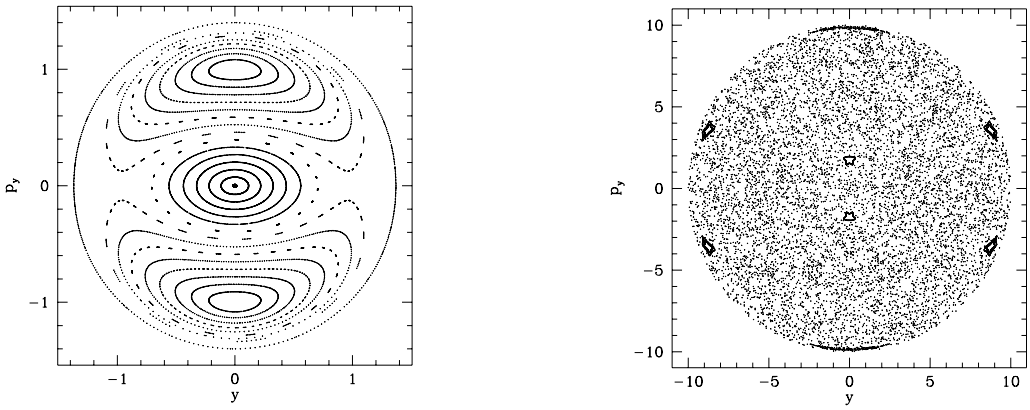

Figure 4.14: *(a) Poincaré section at energy* $E = 1$ *(b) Section at* $E = 50.0$*. The parameter for the both cases is* $\beta = 0.1$*.*

and we see the usual invariant tori. At $E = 50$ the system has already made a transition to predominantly chaotic behaviour. As in the case of coupled quartic oscillator, the system never becomes completely chaotic since the channel periodic orbit oscillates between stability and instability. However high the parameter, there are likely to be windows of stable region for this orbit and thus there will be miniscule islands in phase space. The presence of channel leads to a series of quantum states localising along the channels, influenced by the channel periodic orbit. Apart from the channel localised states there are other scarred states of coming in different varieties. It must be remarked that since Anchell's study [94] confined only to 62 states from the ground state, his conclusion that all the eigenstates have configuration space densities concentrated either along the channels (shape of +) or 45^o to the channels (shape of X) does not seem to be borne by the results of eigenstates from the highly excited states. Here we present eigenststates for a typical state and a channel localised state. Now we directly go to look at the structure of the eigenstates in the unperturbed space. For the same two states presented above the modulus of the eigenvector coefficients are plotted in the fig. 4.15. All the channel localised states have the same structure in the unperturbed space, which as we pointed out for the quartic oscillator, is universal in nature. A closer look at the structure of eigenvectors $|b_{n,j}|$ reveals that they too are dominated by exponentially falling peaks in the quantum number of motion perpendicular to that of the channel motion. The graphical evidence for exponential falloff from the dominant peak is presented below for three values of energies corre-

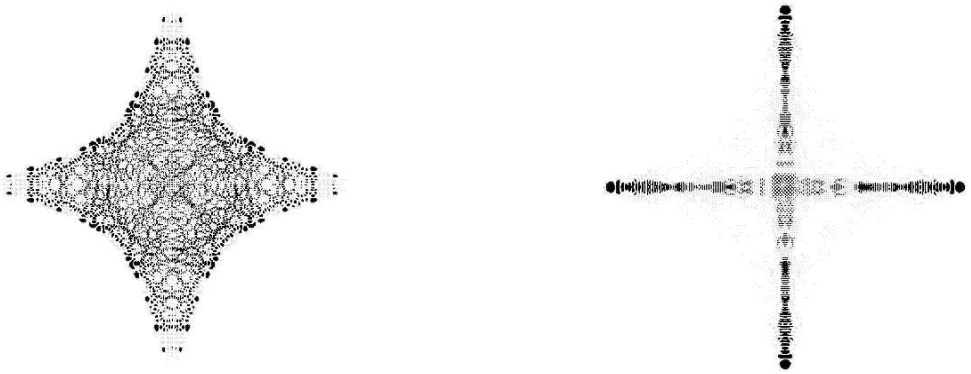

Figure 4.15: *(a) A typical eigenstate (958th state) (b) A channel localised state (874th state)*

sponding to marginally stable and unstable cases of the channel periodic orbit. This system provides right testing ground to study the relation between the stability of the channel orbit and the degree of localisation. Note that in this system the stability is a function of scaled parameter ϵ. Since the scaled parameter ϵ is a function of the energy E, a global picture of the stability of the channel orbit and its influence on the degree of localisation, as measured by the information entropy, can be obtained in this system.

Except for the Berry-Voros hypothesis, which has later been shown to be incomplete, there have been no theoretical attempts since then to explain the scarring phenomena in a individual eigenfunction for a chaotic system. The theoretical framework for scars developed by Berry [33] and Bogomolny [34] provide predictions for groups of eigenfunctions averaged over a small energy range and not an individual eigenstate.

In the general analytical framework of scarring as developed by Berry, the spectral Wigner function averaged over a small energy scale is shown to be influenced by isolated periodic orbits semiclassically. For a Hamiltonian system $H(\mathbf{x})$ with M degrees of freedom the Weyl transform of the spectral operator $\delta_\varepsilon(E - \hat{H})$ gives the spectral Wigner function defined as,

$$W(x; E, \varepsilon) = h^M \sum_n \delta_\varepsilon(E - E_n) W_n(x) \tag{4.28}$$

where W_n are the Wigner functions of the eigenstates of the system. The goal is to obtain a semiclassical expression for the spectral Wigner function. The function eq. (4.28) is represented as a time integral in terms of K_w, the Wigner-Weyl transform of the coordinate propagator,

$$W(x; E, \varepsilon) = \frac{2}{h} Re \int_0^\infty dt \ \exp\left[-\frac{it}{\hbar}(E - i\varepsilon)\right] K_w(\mathbf{x}, t) \tag{4.29}$$

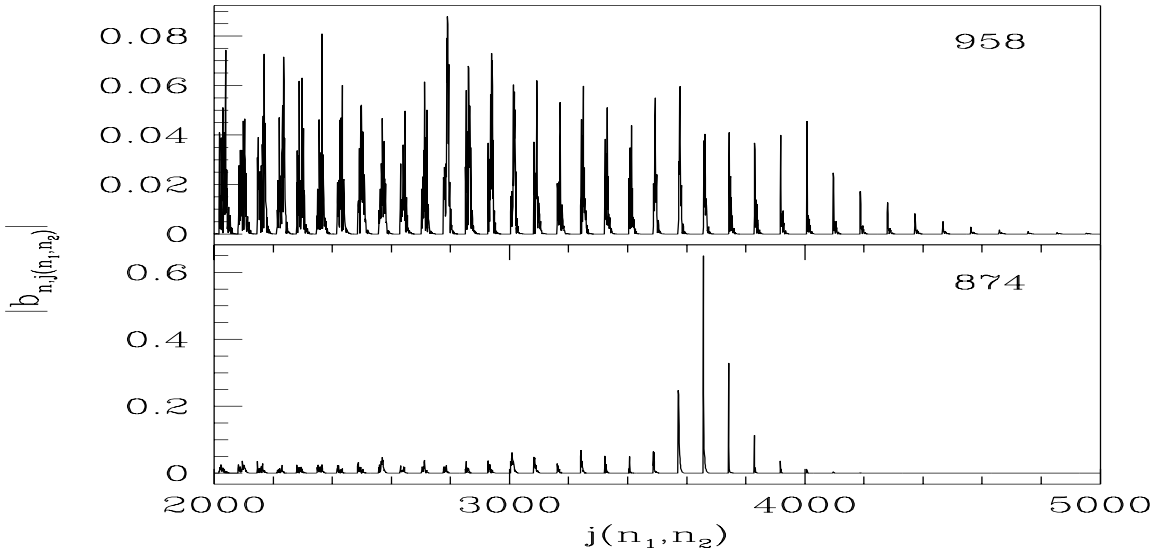

Figure 4.16: *The eigenvectors for (a) A typical eigenstate (958th state) (b) A channel localised state (874th state)*

The Wigner-Weyl transform of the coordinate propogator $K =< \mathbf{q}_b|exp(-i\hat{H}t/\hbar)|\mathbf{q}_a >$ from point $\mathbf{q}_a$ to $\mathbf{q}_b$ in time t is given by,

$$K_w(\mathbf{x},t) = \int dq' \quad \exp(-\frac{i}{\hbar}\mathbf{q}'.\mathbf{p}) \quad K(\mathbf{q} - \frac{\mathbf{q}'}{2}, \mathbf{q} - \frac{\mathbf{q}'}{2}, t) \tag{4.30}$$

The usual semiclassical approximation for the coordinate propogator K is used to express it as a sum over all the classical paths starting from $\mathbf{q}_a$ and terminating at $\mathbf{q}_b$ in time t. The integral in eq. (4.30) is evaluated in stationary phase approximation and further manipulated to obtain the semiclassical expression,

$$W(x;E,\varepsilon) \approx \delta_\varepsilon(E - H(\mathbf{x})) + \sum_j W_j^{scar}(\mathbf{x};E,\varepsilon) \tag{4.31}$$

The first term in eq. (4.31) corresponds to the neighbouthood of $t \to 0$ limit which gives the classical result for W, namely the microcanonical distribution of states near E over the entire energy surface. The second term gives strong contributions to smoothed Wigner function from closed orbits of period T, which form the density enhancements called scars. In ref. [33] Berry evaluates the contribution from the second term and we will not reproduce it here. We will confine only to the quantities of interest; the scar weight d_w defined as the phase space integral of the spectral Wigner function, and scar amplitude d_a and their relation to the stability of the classical orbit. If $\mathbf{M}$ represents the linearised Poincaré map for the closed orbit of interest then,

$$d_w \propto det(\mathbf{M} - \mathbf{I})^{-\frac{1}{2}} \qquad d_a \propto det(\mathbf{M} + \mathbf{I})^{-\frac{1}{2}} \tag{4.32}$$

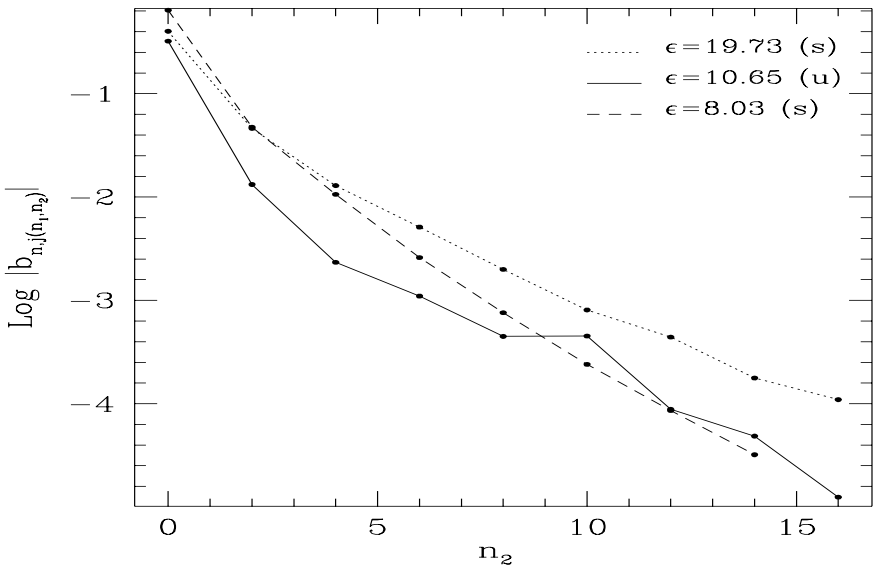

Figure 4.17: *Exponential localisation for three channel localised states of the perturbed oscillator.* u *and* s *represent the unstable and marginally stable nature of the channel orbit. Note that* n_1 *is not the same for all the curves.*

For a two-dimensional system, the monodromy matrix is of order 2 with eigenvalues $e^{\pm\lambda}$. By varying the parameter the orbit bifurcations can take place, due to which the denominators in eq. (4.32) can vanish leading to infinite amplitude or infinite scar weight. Specifically, Berry's scar formula predicts that the scar amplitude for a group of eigenstates diverges at all the points of pitchfork bifurcation (Tr$J = -2$ for half map). Armed with this result we proceed to look at our observations.

The fig. 4.18 is an unmistakable evidence for the second contention we made earlier in this chapter; that the degree of localisation is strongly correlated with the stability of the underlying orbit. In this figure, the entropy and the stability curves are superimposed. The stability of the channel orbit is given by Tr $J(\epsilon)$ where J is the monodromy matrix explained in chapter 1, and we have used the usual full Poincaré map to compute the stability. Since Tr J $= -2$ in half map corresponds to Tr J $= 2$ for a full Poincaré map, in the fig. 4.18, the quantity $|\text{Tr } J(\epsilon) - 2|$, an indicator of the stability of the channel orbit, and the information entropy for the first 2000 states are plotted against ϵ. In fig. 4.18 all the channel localised states are connected by a solid line while the broken line is the stability curve for the channel periodic orbit. In the pictures of the localised eigenstates shown in the gallery, we identify the scar concentrations along the channel periodic orbit as the scar amplitude defined by Berry. The entropy measure is an indication of how good the scar concentration is. Though Berry's formula predicts infinite scar amplitudes, in practice the computational results indicate large scar concentrations rather than infinities.

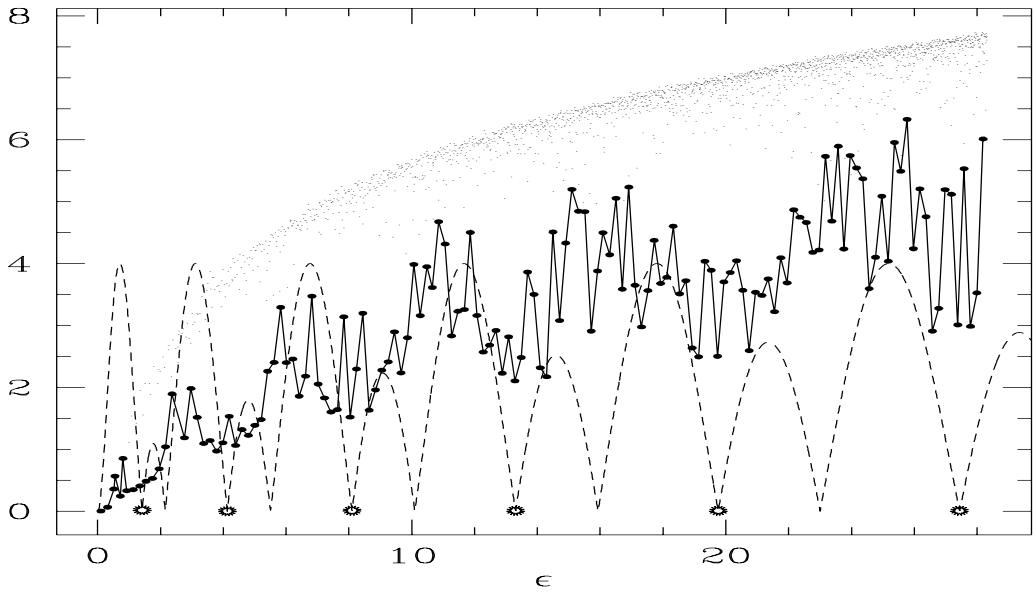

Figure 4.18: *The information entropy oscillates as function of the parameter and is correlated with the stability of the channel orbit. The y axis corresponds to the information entropy curve and matches with the stability curve only at $y = 0$ (see text).*

The light dots in the background in the fig. 4.18 represent the entropies of the typical extended states. Neglecting this envelope of the information entropy in fig. 4.18, which follows the predictions of random matrix theory, the entropy of channel localised states show remarkable oscillations that strongly correlate with the stability oscillations of the channel orbit. We note from fig. 4.18 that the open circles corresponding to Tr $J(\epsilon) = 2$ are points of pitchfork bifurcation at which channel orbit loses stability after a brief spell of stability. As the figure shows these points correlate strongly with the local entropy minima of the channel localised states. It is indeed remarkable that a gross measure of localisation as information entropy captures the nuances of localised states.

The pitchfork bifurcation also occurs at points where the channel orbit crosses over to stable behaviour after being unstable for a small window of parametric values. We may note that when the orbit gains stability at these points the entropy is not a minimum although Gutzwiller's trace formula breaks down here as well; and Berry's scar amplitude formula also predicts divergence. The trend in entropy oscillation clearly indicates that the area of stability also plays a crucial role in determining the degree of localisation. When the channel orbit begins to gain stability the island structure in the Poincaré section is not well-developed and is of miniscule size. On the other hand, when the orbit loses stability the size of the island is much larger and is just beginning to bifurcate in to two. Thus we emphasise that the entropy

minima must also have to do with the local structure around the periodic orbit and not depend only on the stability matrix of the scarring orbit.

Berry's scar formula is strictly valid for averaged Wigner functions rather than for individual eigenstates in coordinate representation. Quantitative verification of scar theories such as these do not seem to be straightforward. The numerical computation of a large number of eigenstates of time-independent systems is not feasible beyond a point and more importantly there are problems of interpretation and of adapting them to the requirements of the theory. The results obtained above should be viewed in the light of these difficulties. Though the results of the foregoing studies convey lot of information, we can atleast unambiguously make the following two statements. The numerical results strongly indicate that (i) the channel localised states are in some sense exponentially localised and (ii) the stability of the scarring orbit correlates strongly degree of localisation.

CHAPTER 5

Three-Dimensional Systems

The interest in three-dimensional chaotic quantum systems has just begun in the last few years and some of the first results have started appearing in the literature. Both classically and quantum mechanically, the three-dimensional systems reveal much richer dynamical structure than what can be seen in two-dimensional systems. In this chapter, we will present some results on the eigenvalue spacing distribution for two different three dimensional potentials.

Classically, the three-dimensional systems exhibit phenomena called Arnold diffusion, which is absent in the two-dimensional systems [44]. In two-dimensional systems, resonance between the two degrees of freedom gives rise to dense regions of stochasticity near the seperatrices, called the resonance layer. The resonance layers are separated from one another by the KAM tori. In a two-dimensional system, the KAM tori are also two-dimensional and hence they divide the three-dimensional phase space into compartments. The trajectories cannot go from one resonance layer to another. Due to conservation of the integrals of motion for a Hamiltonian system, the trajectories are restricted to move only across the resonance layer. Suppose if the system has three degrees of freedom, then the three dimensional KAM surfaces cannot divide five-dimensional energy volume in water-tight compartments. This leads to slow diffusive motion of the stochastic trajectories along the resonance layer. This is called Arnold diffusion. Clearly this phenomena can take place in systems with more than two-degrees of freedom. Thus the different resonance layers are connected by these trajectories forming what is called the Arnold web. Arnold has rigorously shown the existence of the web for a particular Hamiltonian system [95]. Later on, Chirikov and others [96] have calculated the rates for Arnold diffusion. More recently, Milczewski *et. al.* have computed the Arnold's web for the hydrogen atom in crossed electric and magnetic fields [97].

While even the classical behaviour of three degree of freedom systems have not yet been exhaustively studied, the quantum mechanics of such systems is still an unexplored area. For instance, classically it is difficult to visualise the four-dimensional Poincaré sections. In 1970 Froeschle had devised a graphical and numerical method, using the 'surface of section' technique, to study the dynamics of three-dimensional systems [98]. Recently, a frequency analysis method has been proposed to study the dynamical behaviour of systems with more than two-degrees of freedom. This method relies on computation of frequency vectors associated with the invariant tori or resonant regions in phase space. This procedure has been implemented to get the global

phase-space structure for a three-dimensional system of an electron in coloumbic and harmonic potential perturbed by static electric and tilted magnetic field [99]. In this system they have reported on the order-chaos transition and scarring of a wave-function by an unusual 'exotic' orbit. More details on the frequency analysis can be found in ref. [100]. On the other hand, the studies from the point of view of 'quantum chaos' have been undertaken only in the last one or two years. In one of the first attempts, two thousand states of three-dimensional Sinai billiard have been computed and shown that periodic orbits in two- and three-dimensions lead to scars thus strongly affecting the quantum spectral properties. Prosen [101] has quantised the generic three-dimensional billiards with smooth boundaries and has studied the high-lying eigenstates and statistical properties of the eigenvalues. This study shows that most of the highly excited eigenstates are uniformly spread over the energy surface. Inspite of strong classical chaos, there are a class of localised states which are influenced by the periodic orbits or certain classically invariant manifolds. Infact, he provides numerical evidence to show that localisation in lower dimensional manifold leads to significant deviations from the usual GOE prediction for the eigenvalue spacing distribution for 3D billiards. Our interest is to study the smooth Hamiltonian systems like the coupled nonlinear oscillators. In this chapter, our limited assignment is to obtain the eigenvalue spacing distributions of two different homogeneous three degree of freedom systems.

5.1 3D Sextic Oscillator

The first of such potential is the three dimensional sextic oscillator given by,

$$H_{so}(x, y, z; p_x, p_y, p_z; \beta_1) = p_x^2 + p_y^2 + p_z^2 + x^6 + y^6 + z^6 + \alpha x^2 y^2 z^2 \tag{5.1}$$

where α is the chaos parameter and the potential is bounded for all positive values of this parameter. Classically this system is integrable only for $\alpha = 0$. As α is increased the system makes a transition from regular to predominantly chaotic behaviour. This particular form of the potential was chosen with the following facts in mind : A class of problems in atom in strong fields can be reduced to that of sextic oscillators [7]. Secondly this is computationally simple and yet physically non-trivial problem in three-dimension. This is so because it affords the luxury of numerically banding the Hamiltonian matrix as pointed out in Chapter 3. This enables us to compute more number of highly excited states without accumulating much error.

The time-independent Schroedinger equation corresponding to the coupled sextic oscillator was solved in the unperturbed basis; namely the $\alpha = 0$ case of Hamiltonian

in eq. (5.1). The eigenstates are expressed as,

$$\Psi_n(x,y,z) = \sum_{j=1}^{\infty} d_{n,j}\psi_j(x,y,z) \tag{5.2}$$

where $\psi_n(x,y,z)$ is appropriately symmetrised linear combination of the one-dimensional sextic oscillator eigenfunctions,

$$\begin{aligned}\psi_j(x,y,z) &= C(n_1,n_2,n_3)\ [\chi^e_{n_1}(x)\chi^e_{n_2}(y)\chi^e_{n_3}(z) + \chi^e_{n_1}(y)\chi^e_{n_2}(x)\chi^e_{n_3}(z) + \chi^e_{n_1}(y)\chi^e_{n_2}(z)\chi^e_{n_3}(x) \\ &\quad + \chi^e_{n_1}(x)\chi^e_{n_2}(z)\chi^e_{n_3}(y) + \chi^e_{n_1}(z)\chi^e_{n_2}(y)\chi^e_{n_3}(x) + \chi^e_{n_1}(z)\chi^e_{n_2}(x)\chi^e_{n_3}(y)]\end{aligned}$$

where $C(n_1,n_2,n_3)$ is the normalisation constant given by,

$$\begin{aligned}C(n_1,n_2,n_3) &= \frac{1}{\sqrt{6}} \qquad (n_1 \neq n_2 \neq n_3,\ \ n_1 \neq n_3) \\ &= \frac{1}{6} \qquad (n_1 = n_2 = n_3) \\ &= \frac{1}{\sqrt{12}} \qquad (n_1 = n_2 \neq n_3,\ \ n_1 = n_3 \neq n_2,\ \ n_2 = n_3 \neq n_1)\end{aligned}$$

and n_1, n_2 and n_3 are the quantum numbers. The one-dimensional sextic oscillator eigenfunctions $\chi_n(x)$ are accurately computed using the phase-amplitude method referred to in Chapter 3. We used 35 one-dimensional basis states to compute 7000 three dimensional basis states leading to Hamiltonian matrices of order 7000. The numerical diagonalisation gave between 900-1000 converged eigenvalues for the ranges of parameter $\alpha = 1$ to $\alpha = 25$ used.

We begin by first unfolding the spectrum. The method we follow is presented in detail in ref. [26]. The mean level density $d(E) = \sum \delta(E - E_i)$ and its Laplace transform for a M degree of freedom system is given by,

$$Z(\beta) = \int_0^{\infty} e^{-\beta E} d(E) dE = \frac{1}{2\pi\hbar^M} \int d\mathbf{q}\ \ d\mathbf{p}\ \ [e^{-\beta H}]_w(\mathbf{p},\mathbf{q}) \tag{5.3}$$

which requires the Wigner transform, $[e^{-\beta H}]_w(\mathbf{p},\mathbf{q})$. Usually an equation is generated by differentiating with respect to β and applying the product rule for Wigner transform of the product of two operators. A series solution of the form,

$$[e^{-\beta H}]_w(\mathbf{p},\mathbf{q}) = \exp\ \left[\sum_{n=0}^{\infty} \left(\frac{-\hbar^2}{4}\right)^n \frac{A_n(\mathbf{q},\mathbf{p},\beta)}{2n!}\right] \tag{5.4}$$

is obtained where the first coefficient A_1 has been derived by Wigner [30] and is given by,

$$A_1(\mathbf{p},\mathbf{q},\beta) = \frac{1}{m}\left(\beta^2 \bigtriangledown^2 V(\mathbf{q}) - \frac{\beta^3}{3m}[m \bigtriangledown V(\mathbf{q}).\bigtriangledown V(\mathbf{q}) + (\mathbf{p}.\bigtriangledown)^2 V(\mathbf{q})]\right) \tag{5.5}$$

where m is the mass. By taking the inverse Laplace transform of $Z(\beta)$ the level density is determined. The level density $d(E)$ is related to the staircase function by the relation,

$$d(E) = \frac{dN(E)}{dE}$$

We follow this procedure to calculate the staircase function for the sextic oscillator system. In fact, the leading energy behaviour can also be obtained by the application of the semiclassical rule that each quantum state is associated with a phase-space volume h^M, where M is the dimensionality of the quantum system. Our derivation proceeds as follows,

$$Z(\beta) = \frac{1}{(2\pi\hbar)^N} \int d\mathbf{q}\ d\mathbf{p}\ \ [e^{\beta H}]_w(\mathbf{q},\mathbf{p}) \tag{5.6}$$

$$Z(\beta) = \frac{1}{(2\pi\hbar)^N} \int d\mathbf{q}\ d\mathbf{p}\ \ \exp[-\beta H_w - \hbar^2 A_1/8] \tag{5.7}$$

where H_w is Wigner transform of the Hamiltonian and in this case happens to be identical with the Hamiltonian (5.1). To obtain the level density we have to perform the follwing integral.

$$d(E) = \frac{1}{4\pi^2} \int d\beta\ e^{\beta E} \int d\mathbf{q}\ \ d\mathbf{p}\ \ \exp\left[-\beta H_w - \hbar^2 A_1/8\right] \tag{5.8}$$

For instance, leading order energy dependence can be obtained as,

$$\bar{d}(E) = \frac{1}{4\pi^2} E \int_{-i\infty}^{i\infty} dr\ e^r\ r^2 \int\ dx\ \ dy\ \ dz\ \ \exp[-(x^6+y^6+z^6+\alpha x^2y^2z^2)] \tag{5.9}$$

where $r = \beta E$ and this result agrees with the Thomas-Fermi term. Thus, leading behaviour of the staircase function is obtained by differentiating with respect to energy E. Performing this entire exercise after including the second term in the integral (5.7), we get the follwing result.

$$N(E) \sim aE^2 + bE^{3/2} \tag{5.10}$$

where a and b are independent of energy E and are determined by fitting this expression to a sequence of quantum energy levels. In the fitting procedure, about 800 eigenvalues were used and first 50 eigenvalues were removed as usual. In the fig. 5.1, the staircase function in eq. (5.10) is plotted along with the one obtained from the exact quantum energy levels obtained by numerical diagonalisation. The figure clearly shows that eq. (5.10) is a very good approximation to the actual staircase function. In fig. 5.2 we show the eigenvalue spacing distribution curves. The histogram is the energy spacing distribution curve for the sextic oscillator and the solid curve is the eigenvalue spacing distribution for the Gaussian orthogonal ensemble of the random matrix theory. We have performed this exercise for four different values of the parameter, namely $\alpha = 1.0, 3.0, 10.0$ and 25.0. The figures clearly reveal that the GOE distribution in eq. (1.12) becomes a good fit as the parameter is increased. At $\alpha = 25.0$ the histogram and the solid curve are in good agreement. The shift in the histogram curve in fig. 5.2 from poisson like at $\alpha = 0$ to GOE distribution at $\alpha = 25.0$ indicates that the underlying classical dynamics also undergoes transition to predominantly chaotic behaviour.

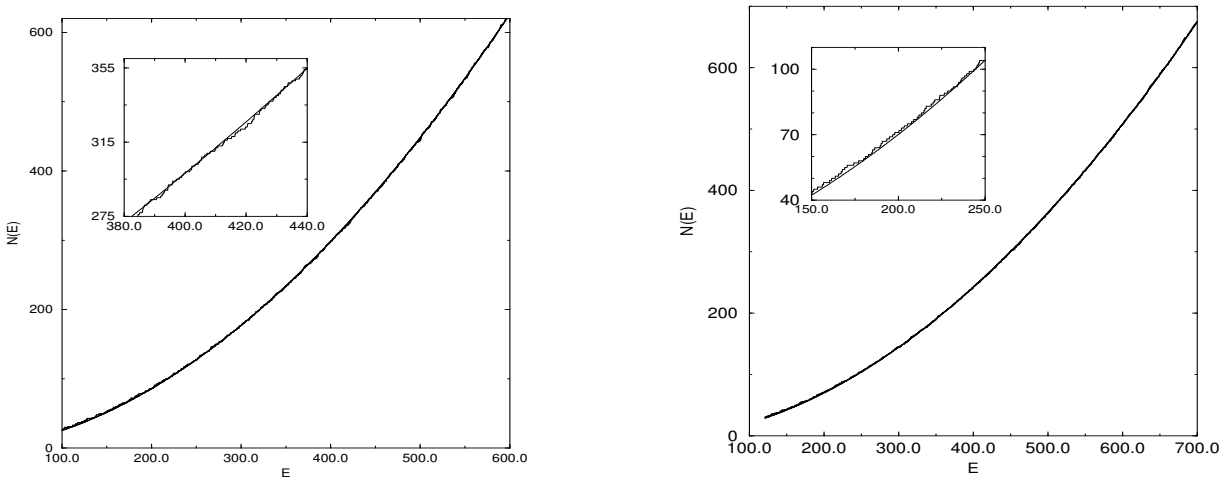

Figure 5.1: The staircase function $N(E)$ given by eq. 5.10 and the exact staircase function are plotted for (a) α = 3.0 and (b) α=25.0. The inset is the enlargement of a portion of the larger graph for clarity.

5.2 3D Coupled Quartic Oscillator

The next three dimensional system we study is the 3-coupled quartic oscillator given by,

$$H_{3d}(x,y,z;p_x,p_y,p_z;\alpha_1,\alpha_2,\alpha_3) = p_x^2+p_y^2+p_z^2+x^4+y^4+z^4+\alpha_1 x^2y^2+\alpha_2 y^2z^2+\alpha_3 z^2x^2 \quad (5.11)$$

where, α_1, α_2 and α_3 are parameters. We will assume a single parameter Hamiltonian by setting for the rest of our work $\alpha_1 = \alpha_2 = \alpha_3 = \alpha_q$.

The contours of this 3-dimensional potential are isosurfaces corresponding to different values of constant potential energy. Due to limitations of visualisation, we see only the outermost isosurface. The isosurface is in the form of an octohedron in three-dimensional space. This system is classically integrable for $\alpha_1 = \alpha_2 = \alpha_3 = 0, 2$ Lakshmanan and Sahadevan [102] have performed the Painleve analysis for a more general coupled oscillator and have listed the various parameter values for which the system is integrable. This system is homogeneous implying the usual scaling with respect to energy [46]. The potential is bounded for all the positive values of the parameter. This system also makes a transition from regular to chaotic behaviour as the perturbation strength is increased.

5.3 Group Structure of Quartic Oscillator

The Hamiltonian in eq. (5.11) possesses much richer symmetry properties than the 2D quartic oscillator. This belongs to different point group symmetries depending on

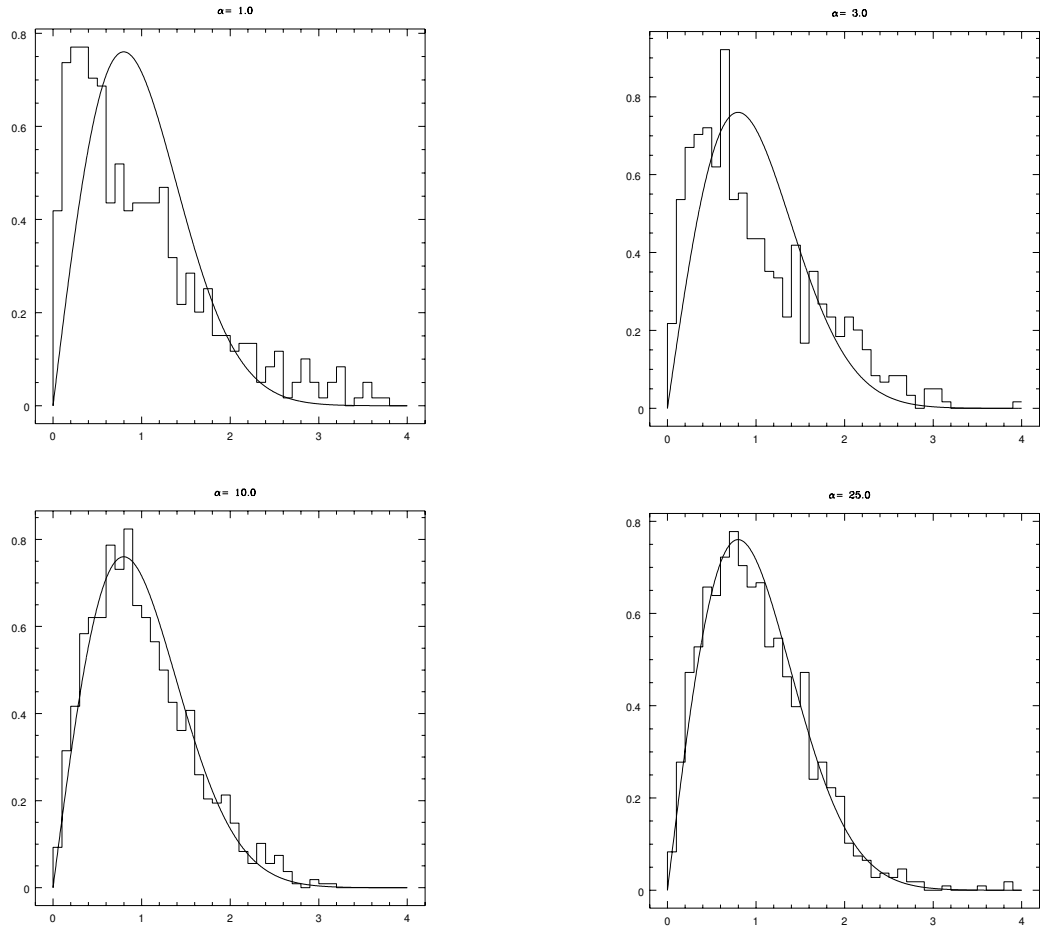

Figure 5.2: *Eigenvalue spacing distribution for coupled sextic oscillator for parametric values ; (a)* $\alpha = 1.0$ *(b)* $\alpha = 3.0$ *(c)* $\alpha = 10.0$ *(d)* $\alpha = 25.0$*. The solid curve is the GOE curve.*

the values of α_1, α_2 and α_3. The following three cases can be identified :

(a) If all the parameters take equal values, $i.e, \alpha_1 = \alpha_2 = \alpha_3$, the case we are interested in this present work, then this Hamiltonian belongs to the full octohedral group O_h. Since this is also the group of all transformations of a regular cube, for convenience, we can imagine the octahedron to be enclosed inside a cube such that the six corners of the octahedron touch the midpoint of each face of the cube. Thus, this configuration of Hamiltonian has very high degree of symmetry with 48 group elements.

(b) If any two of the parameters are equal, then the symmetry group is D_{4h}. This is the group of transformations of an irregular 'cube', in which the top and bottom faces are squares and all other remaining faces are rectangles. This group has 24 symmetry elements.

(c) If $\alpha_1 \neq \alpha_2 \neq \alpha_3$ and $\alpha_1 \neq \alpha_3$, then the group is D_{2h}. This is the group of transformations of a cuboid. This is the lowest possible symmetry for this Hamiltonian

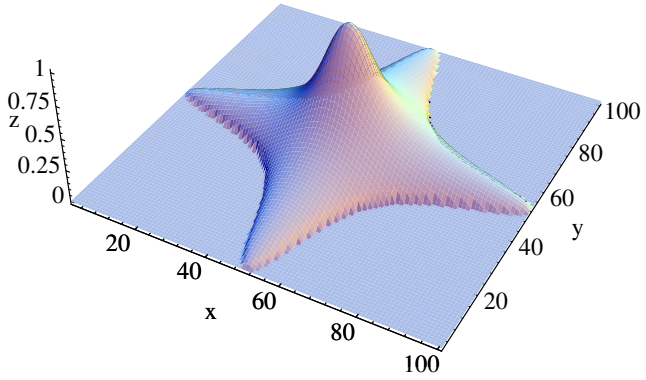

Figure 5.3: Top portion of the isosurface for the 3D coupled quartic oscillator at $\alpha_q = 90.0$

with 10 group elements.

5.3.1 The Octahedral Group

The O_h group has 48 elements including identity, eight $\pi/3$ rotations about body diagonals, three π and six $\pi/2$ rotations about X, Y, Z axes, six π rotations about axes through origin and midpoint of the edges and the inversion. To get a concrete picture, we can consider the molecule SF_6, with S atom at the centre and six F atoms sitting in the six corners of tetrahedron [103]. We follow the standard group theory notations as given, for instance, in ref. [57]. The character table for O_h group is obtained from the direct product $O_h = O \otimes i$, where the inversion operator i has the character table given below,

	E	i
Γ^+	1	1
Γ^-	1	-1

The character table for O_h group is given below:

	E	$8C_3$	$3C_2$	$6C_2^{'}$	$6C_4$	$-E$	$8(-C_3)$	$3(-C_2)$	$6(-C_2^{'})$	$6(-C_4)$
A_1	1	1	1	1	1	1	1	1	1	1
A_2	1	1	1	-1	-1	1	1	1	-1	-1
E	2	-1	2	0	0	2	-1	2	0	0
T_1	3	0	-1	-1	1	3	0	-1	-1	1
T_2	3	0	-1	1	-1	3	0	-1	1	-1
$\bar{A_1}$	1	1	1	1	1	-1	-1	-1	-1	-1
$\bar{A_2}$	1	1	1	-1	-1	-1	-1	-1	1	1
$\bar{E}$	2	-1	2	0	0	-2	1	-2	0	0
$\bar{T_1}$	3	0	-1	-1	1	-3	0	1	1	-1
$\bar{T_2}$	3	0	-1	1	-1	-3	0	1	-1	1

In constructing basis functions, we will be presently interested only in the one-dimensional irreducible representations. For the O_h symmetry, the basis functions are as follows.

$$\begin{aligned}\psi_j^{A_1}(x,y,z) &= \phi^e_{n_1}(x)\phi^e_{n_2}(y)\phi^e_{n_3}(z) + \phi^e_{n_1}(y)\phi^e_{n_2}(x)\phi^e_{n_3}(z) + \phi^e_{n_1}(y)\phi^e_{n_2}(z)\phi^e_{n_3}(x) \\ &\quad + \phi^e_{n_1}(x)\phi^e_{n_2}(z)\phi^e_{n_3}(y) + \phi^e_{n_1}(z)\phi^e_{n_2}(y)\phi^e_{n_3}(x) + \phi^e_{n_1}(z)\phi^e_{n_2}(x)\phi^e_{n_3}(y)\end{aligned}$$

$$\begin{aligned}\psi_j^{\bar{A}_2}(x,y,z) &= \phi^o_{n_1}(x)\phi^o_{n_2}(y)\phi^o_{n_3}(z) + \phi^o_{n_1}(y)\phi^o_{n_2}(x)\phi^o_{n_3}(z) + \phi^o_{n_1}(y)\phi^o_{n_2}(z)\phi^o_{n_3}(x) \\ &\quad + \phi^o_{n_1}(x)\phi^o_{n_2}(z)\phi^o_{n_3}(y) + \phi^o_{n_1}(z)\phi^o_{n_2}(y)\phi^o_{n_3}(x) + \phi^o_{n_1}(z)\phi^o_{n_2}(x)\phi^o_{n_3}(y)\end{aligned}$$

$$\begin{aligned}\psi_j^{\bar{A}_1}(x,y,z) &= \phi^o_{n_1}(x)\phi^o_{n_2}(y)\phi^o_{n_3}(z) - \phi^o_{n_1}(y)\phi^o_{n_2}(x)\phi^o_{n_3}(z) - \phi^o_{n_1}(y)\phi^o_{n_2}(z)\phi^o_{n_3}(x) \\ &\quad + \phi^o_{n_1}(x)\phi^o_{n_2}(z)\phi^o_{n_3}(y) - \phi^o_{n_1}(z)\phi^o_{n_2}(y)\phi^o_{n_3}(x) + \phi^o_{n_1}(z)\phi^o_{n_2}(x)\phi^o_{n_3}(y)\end{aligned}$$

$$\begin{aligned}\psi_j^{A_2}(x,y,z) &= \phi^e_{n_1}(x)\phi^e_{n_2}(y)\phi^e_{n_3}(z) - \phi^e_{n_1}(y)\phi^e_{n_2}(x)\phi^e_{n_3}(z) - \phi^e_{n_1}(y)\phi^e_{n_2}(z)\phi^e_{n_3}(x) \\ &\quad + \phi^e_{n_1}(x)\phi^e_{n_2}(z)\phi^e_{n_3}(y) - \phi^e_{n_1}(z)\phi^e_{n_2}(y)\phi^e_{n_3}(x) + \phi^e_{n_1}(z)\phi^e_{n_2}(x)\phi^e_{n_3}(y)\end{aligned}$$

5.3.2 The D_{4h} Group

The second case arises when any two of the parameters in the Hamiltonian defined by eq. (5.11) are equal and the potential has D_{4h} point group symmetry. This group has two $\pi/2$ and π rotations about the axis of highest symmetry, four two-fold axis perpendicular to it. Another crucial symmetry element is the inversion i. The organic molecule cyclobutane, C_4H_8 is an example of a real system having this symmetry configuration [103]. In the top left quadrant of the character table is the one for D_4 group. By including the inversion, the character table for D_{4h} group is obtained from the relation, $D_{4h} = D_4 \otimes i$.

The character table shows 8 one-dimensional irreducible representations and 2 degenerate representations.

	E	C_2	$2C_4$	$2C_2^{'}$	$2C_2^{''}$	$-E$	$-C_2$	$2(-C_4)$	$2(-C_2^{'})$	$2(-C_2^{''})$
A_1	1	1	1	1	1	1	1	1	1	1
A_2	1	1	1	-1	-1	1	1	1	-1	-1
B_1	1	1	-1	1	-1	1	1	-1	1	-1
B_2	1	1	-1	-1	1	1	1	-1	-1	1
E	2	-2	0	0	0	2	-2	0	0	0
$\bar{A}_1$	1	1	1	1	1	-1	-1	-1	-1	-1
$\bar{A}_2$	1	1	1	-1	-1	-1	-1	-1	1	1
$\bar{B}_1$	1	1	-1	1	-1	-1	-1	1	-1	1
$\bar{B}_2$	1	1	-1	-1	1	-1	-1	1	1	-1
$\bar{E}$	2	-2	0	0	0	-2	2	0	0	0

The A_1 identical representation of D_{4h} and O_h point groups share the same basis function. Without listing again, the basis functions for B_2, $\bar{B}_2$ and $\bar{A}_1$ representations of D_{4h} point group are the same as the ones for B_1, B_2 and A_2 representations respectively of O_h point group discussed above. The remaining basis functions are as follows:

$$\begin{aligned}
\psi_j^{\bar{A}_2}(x,y,z) &= \phi_{n_3}^o(z)\,[\phi_{n_1}^e(x)\phi_{n_2}^e(y) + \phi_{n_1}^e(y)\phi_{n_2}^e(x)] \\
\psi_j^{\bar{B}_1}(x,y,z) &= \phi_{n_3}^o(z)\,[\phi_{n_1}^e(x)\phi_{n_2}^e(y) - \phi_{n_1}^e(y)\phi_{n_2}^e(x)] \\
\psi_j^{B_1}(x,y,z) &= \phi_{n_3}^e(z)\,[\phi_{n_1}^o(x)\phi_{n_2}^o(y) + \phi_{n_1}^o(y)\phi_{n_2}^o(x)] \\
\psi_j^{A_2}(x,y,z) &= \phi_{n_3}^e(z)\,[\phi_{n_1}^o(x)\phi_{n_2}^o(y) - \phi_{n_1}^o(y)\phi_{n_2}^o(x)]
\end{aligned}$$

The structure of these above four basis functions show that the z direction enjoys a special status. It should be emphasised that *only* $\phi_n(z)$, and not $\phi_n(x)$ or $\phi_n(y)$, can be multiplied to a linear combination of symmetrised two-dimensional functions. This is because the transformations of irregular 'cube' do not mix z axis with any other axes. It is evident from the transformation matrices that while x and y axes go from one to another, z axis does not mix with other axes. Obviously we cannot further symmetrise this structure by including more terms, since the parity of n_1, n_2 and n_3 are fixed for a particular representation.

5.3.3 The D_{2h} Group

The Hamiltonian in eq. (5.11) has D_{2h} symmetry if $\alpha_1 \neq \alpha_2 \neq \alpha_3$ and $\alpha_1 \neq \alpha_3$. The group D_2 admits only four symmetry transformations, namely, identity and rotation by π about each of the three axes. Thus, including the inversion, this group has

8 elements. For instance, the plane C_2H_4 and N_2O_4 molecules belong this symmetry family. This configuration has the lowest symmetry for the case of Hamiltonian given by (1). Since we will not consider this case, here the basis function for A_1 is representation is provided.

$$\psi_j^{A_1}(x,y,z) = \phi_{n_1}^e(x)\phi_{n_2}^e(y)\phi_{n_3}^e(z)$$

Again, for A_1 representation here, we could also have used the same basis function as in A_1 representations of O_h and D_{4h}.

	E	C_2^z	C_2^y	C_2^x	$-E$	$-C_2^z$	$-C_2^y$	$-C_2^x$
A_1	1	1	1	1	1	1	1	1
B_1	1	1	-1	-1	1	1	-1	-1
B_2	1	-1	1	-1	1	-1	1	-1
B_3	1	-1	-1	1	1	-1	-1	1
$\bar{A}_1$	1	1	1	1	-1	-1	-1	-1
$\bar{B}_1$	1	1	-1	-1	-1	-1	1	1
$\bar{B}_2$	1	-1	1	-1	-1	1	-1	1
$\bar{B}_3$	1	-1	-1	1	-1	1	1	-1

The basis function for the one-dimensional representations are given below :

$$\psi_j^{A_1}(x,y,z) = \phi_{n_1}^e(x)\phi_{n_2}^e(y)\phi_{n_3}^e(z)$$
$$\psi_j^{B_1}(x,y,z) = \phi_{n_1}^o(x)\phi_{n_2}^o(y)\phi_{n_3}^e(z)$$
$$\psi_j^{B_2}(x,y,z) = \phi_{n_1}^o(x)\phi_{n_2}^e(y)\phi_{n_3}^o(z)$$
$$\psi_j^{B_3}(x,y,z) = \phi_{n_1}^e(x)\phi_{n_2}^o(y)\phi_{n_3}^o(z)$$
$$\psi_j^{\bar{A}_1}(x,y,z) = \phi_{n_1}^o(x)\phi_{n_2}^o(y)\phi_{n_3}^o(z)$$
$$\psi_j^{\bar{B}_1}(x,y,z) = \phi_{n_1}^e(x)\phi_{n_2}^e(y)\phi_{n_3}^o(z)$$
$$\psi_j^{\bar{B}_2}(x,y,z) = \phi_{n_1}^e(x)\phi_{n_2}^o(y)\phi_{n_3}^e(z)$$
$$\psi_j^{\bar{B}_3}(x,y,z) = \phi_{n_1}^o(x)\phi_{n_2}^e(y)\phi_{n_3}^e(z)$$

Again, for A_1 representation here, we could also have used the same basis function as in A_1 representations of O_h and D_{4h}.

5.4 Eigenvalue Spacing Distribution

This system is classically integrable for $\alpha_1 = \alpha_2 = \alpha_3 = 0, 2$ and we will assume a single parameter Hamiltonian by setting for the rest of our work $\alpha_1 = \alpha_2 = \alpha_3 = \alpha_q$. This system is homogeneous implying the usual scaling with respect to energy [46]. The

potential is bounded for all the positive values of the parameter. This system also makes a transition from regular to chaotic behaviour as the perturbation strength is increased.

To compute the stationary states, we follow the usual procedure outlined in Chapter 3. The symmetry properties of this potential are analysed and the basis states for the various irreducible representations are provided in Chapter 3. In this chapter we confine to A_1 irreducible representation only. The eigenstates of this system are given by,

$$\Psi_n(x,y,z) = \sum_{j=1}^{\infty} c_{n,j}\psi_j(x,y,z) \tag{5.12}$$

where $\psi_n(x,y,z)$ is a linear combination of the one-dimensional quartic oscillator eigenfunctions for the A_1 representation given in eq. (5.12). The coefficients $c_{n,j}$ are the eigenvectors in the unperturbed space. Using 30 one-dimensional quartic oscillator basis states, we constructed Hamiltonian matrices of order 7500 and obtained about 800 converged eigenvalues for values of the parameters ranging from $\alpha = 1$ to $\alpha = 60$.

We digress a bit to mention an important point about numerical banding we implemented for the sextic oscillator. The point to note is that the Hamiltonian matrix we used for the current problem was the full real symmetric matrix and numerical banding outlined in Chapter 3 was not performed on it. Though numerical banding worked well in the case of the two-dimensional quartic oscillator system and the three-dimensional sextic oscillator, it could not be beneficially implemented for the three-dimensional quartic oscillator for the following reason; The coupling part of the potential $x^2y^2 + y^2z^2 + x^2z^2$ has three terms, each one coupling only two of the three independent modes. Hence, if we use a basis state of the form given by, eq 5.12 there could be atleast one delta function in each of them leading to sparse Hamiltonian matrix. We observed that nearly 60% of the matrix elements are exact zeros. On the other hand, presence of three three terms in the potential and three quantum numbers (n_x, n_y, n_z) means that the possibility of all the three coupling terms adding to produce a number close to zero is less pronounced. The matrix element would become vanishingly small only if the difference between any pair of quantum numbers is at least larger than 10. Since this condition is difficult to satisfy for all the three coupling terms simultaneously, the numerical banding is not effective. It can still be done, but not beneficial enough to optimise the computation time and random access memory space in the computer.

Following the procedure mentioned above, for the coupled sextic oscillator we determined the energy dependence of the staircase function to be,

$$N(E) \sim aE^{9/4} + bE^{1/4} \tag{5.13}$$

where a and b are independent of energy and were determined by fitting this relation to a sequence of quantum energy levels. Of the 1000 converged eigenvalues from a diagonalisation of matrices of order 7000, we removed first 30 levels and used about 750 levels to obtain the constants a and b. We first take a graphical view of the staircase function $N(E)$ in the following figure. In the figure that follows, the eigenvalue

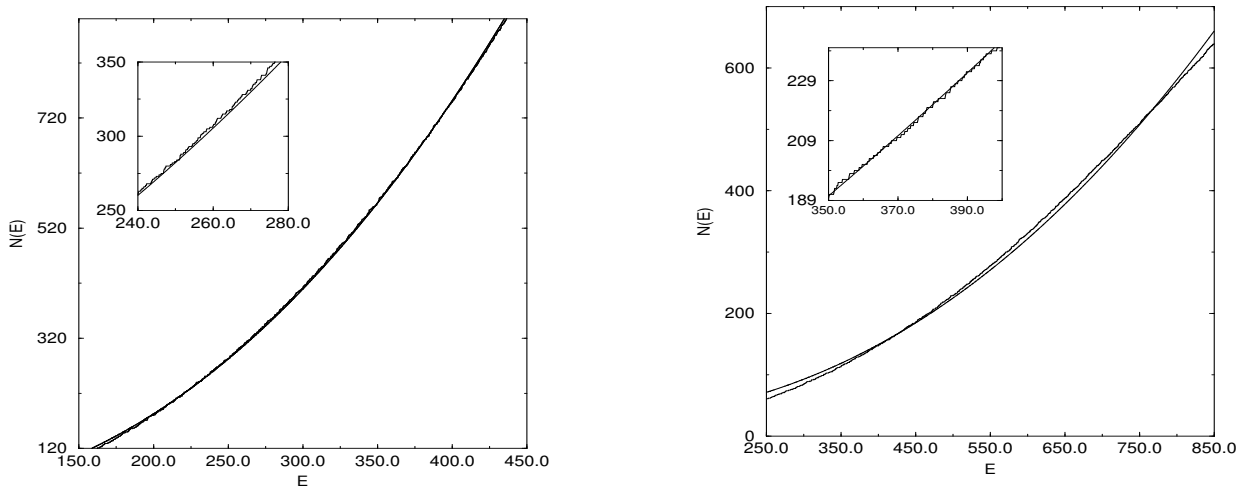

Figure 5.4: The staircase function $N(E)$ given by eq. 5.13 and the exact exact staircase function are plotted for (a) α_q = 1.0 and (b) α_q=60.0. The inset is the enlargement of a portion of the larger graph for clarity.

spacing distribution is shown for the three-coupled quartic oscillator for four different values of the parameter. At $\alpha_q = 1$ the systems shows a spacing distribution close to Poisson like curve. As $\alpha_q = 1$ increases in the positive direction, the distribution curve shows shift towards GOE curve predicted by the random matrix theory. However, as we see, the agreement between the GOE curve and the histogram is not perfect. Our preliminary results from the eigenvector computation showed that three-dimensional coupled quartic oscillator displays interesting hierarchy of localised states not seen in the two-dimensional systems. Our preliminary investigations indicate that, apart from other kinds of strongly states, there exist the familiar channel localised states and that they too form a series. However, more work needs to be done in this direction. Thus, in this sense, there is an increase in the number of states that are not 'random' enough to follow the random matrix principles. In order to obtain a better agreement with the RMT-like behaviour it might be necessary to have a large number of levels so that the localised states become statistically insignificant. As pointed before, Prosen [101] also finds significant deviations from random matrix predictions which he attributes to localisation effects.

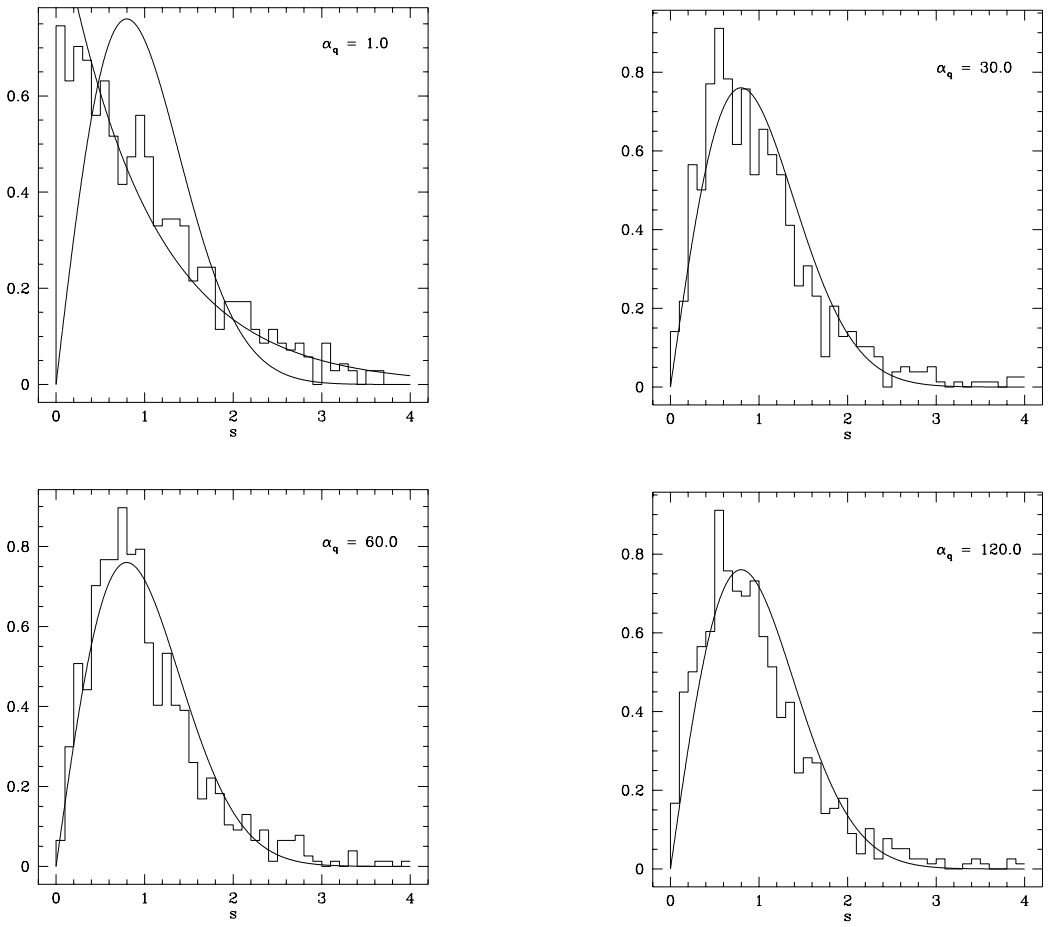

Figure 5.5: *Eigenvalue spacing distribution for coupled quartic oscillator for parametric values ; (a)* $\alpha_q = 1.0$ *(b)* $\alpha_q = 30.0$ *(c)* $\alpha_q = 60.0$ *(d)* $\alpha_q = 120.0$*. The solid curve is the GOE curve and histogram is the spacing distribution.*

Conclusions And Future Directions

The principal aim of the work carried out in this thesis was to understand certain aspects of the quantum mechanics of the classically chaotic systems. Although quantum mechanics had been one of the most successful theories ever known in physics, still its working is not yet completely understood when the underlying systems involved are classically chaotic. This thesis may be regarded as a step taken in this direction; towards exploring the quantum limit of the classically chaotic systems and the relation between the classical and quantum mechanics. In pursuit of these goals, one had two options; study simple systems which may not be generic or take up real-life systems that might be too complicated to obscure the details we are looking for. Adopting middle path, we studied coupled oscillator models, results of which we believe will have a bearing on a wide ranging physical systems such as, for example, the dynamics of atoms in astrophysical objects with strong magnetic fields or localisation effects in the semiconductor heterostructures and so on. Apart from such applications of 'quantum chaos', this study of quantum mechanics has revealed a rich and interesting dynamical properties of the coupled oscillators and also aesthetically pleasing pictures of the eigenstates we had displayed in this thesis. We highlight the important results and possible directions for further studies.

Since the results and conclusions of each chapter have been pointed out in the respective chapters, here we will only look at some salient features of the results to emphasise them. The significant result in the classical dynamics is the *local* parametric scaling of Poincare sections with respect to a single parameter for two-dimensional homogeneous Hamiltonian systems. While scaling with energy itself is well-known for such systems, however what stands out in this result is that the scaling is a function of a single parameter. Thus, we distinguish between the more common and well-known case of dynamical scaling with energy from our new result on the parametric scaling. The scaling formula and scaling exponents we obtained are valid for a large class of Hamiltonian systems. The scaling exponents depend simply on the degree of homogeneity of the system. Intuitively one does not expect scaling behaviour when the phase space is predominantly chaotic. Yet, remarkable result is not only that the scaling exists *locally* in the vicinity of the channel orbit and is valid for a large class of Hamiltonian systems but also that it is valid even when strong chaos predominates in phase space and there are only miniscule stable regions around the channel orbit. We believe the numerical evidence we have provided in Chapter 2 for parametric scaling though we have not been able to give a rigorous mathematical proof. This could be

an important theoretical challenge.

The surprising result from the study of quantum chaotic systems in the last decade is the existence of scars or the concentration of probability density of the eigenstates around the classical periodic orbits. Now it is well-known that the wavefunctions of the most generic quantum system exhibit scars and the theoretical work of Heller, Berry and Bogomolny in this direction have brought to focus the role of the classical periodic orbits in supporting enhanced probability structures in eigenstates. Though we studied several oscillators in this thesis, our principal attention was on the coupled quartic oscillator. We identified one important class of scarred states for further investigation, namely the ones that show density enhancements along the vicinity of the channel periodic orbit. Such eigenstates are called the localised states since the probability density is confined to certain sub-regions of the entire configuration space. We have made an indepth study of their structure, morphology and systematics. Our work also throws light on the relation between certain purely classical quantities like the stability of the periodic orbit and the degree of localisation and information entropy of the quantum wavefunctions scarred by them.

At first sight, one is stuck by the variety of structures exhibited by the eigenstates as is evident from the visual pictures provided in this thesis and elsewhere. The channel localised states stand apart in the entire spectrum since they recur frequently and possibly might continue to exist well in to the classical limit. Indeed, these class of states embody some simple physical picture of particle dynamics inside the potential and are markedly different from a large number of other generic eigenstates. To begin with, the localised states can be identified by the information entropy measure we proposed in Chapter 4. Secondly, as of now, these are the only class of states amenable to approximate theoretical description under the adiabatic approximation which includes semiclassical quantisation. We have refined the adiabatic energy formula for the localised states by including the chaos parameter in it. However, our results indicate that the stability of scarring orbit should also enter as a parameter to complete the picture. Thirdly, the channel localised states do not follow the Porter-Thomas distribution for the eigenvector distribution as predicted by the random matrix theory. This result we have obtained has implications on the assumption of a random Hamiltonian to model the eigenvalue spacing distribution and eigenvector statistics.

The information entropy we apply is a gross measure of localisation and yet surprisingly it is able to distinguish between eigenstates localised to different degree. The 'shadow' states are a point in case. The shadow are called so because they always seem to occur in the vicinity of the channel localised state. These states also form a series in the spectrum of both the coupled quartic and perturbed harmonic oscillator. They are also localised along the channel but are *not* scarred by the channel

orbit *alone*. Generic states are characterised by high entropy values and the channel localised states have low entropy values and for the shadow states the entropy values lie between these two extremes and thus they also stand out in the spectrum. It is not yet clear if these states form a series in the same sense as the series of channel localised states, though they seem to exist in the vicinity of a channel localised state. It must be noted that the shadow states could be located only because we were able to compute, with better computational techniques, nearly 2000 eigenstates from the ground state. The earlier studies have not noticed them possibly because they confined only to study of low-lying eigenstates.

Localisation can also be viewed in the unperturbed space. We expect that the eigenvector coefficients for the localised states will fall faster and will be localised over a few dominantly contributing basis states. Our study of quartic oscillator and perturbed harmonic oscillator shows that it is indeed true since the unperturbed space of the localised states is dominated by a few peaks which fall off rapidly. The remarkable result is that the fall of these eigenvectors in the space of basis states is on an average exponential in nature, which is indicative of very tight and compact localisation features. One recalls that Anderson tight-binding model and kicked rotor display exponential localisation and yet the mechanism of localisation in these systems and in the nonlinear oscillators we studied in this thesis are not the same. Ours is the first observation of exponential localisation in a smooth Hamiltonian system.

Having established that the channel localised states belong to the class of exponentially localised states, the next obvious question is whether the classical properties of the channel orbit affect its localisation properties. All the scar theories predict that scar enhancement is a function of the stability of the orbit. These theories predict for a group of eigenstates in coordinate or in Wigner representation. Hence exact numerical verification of scar theories, though desirable, is not straightforward. The results obtained in this thesis provide systematic numerical evidence for the predictions of the scar theories. We recollect that the stability of the channel orbit as a function of the the parameter is oscillatory in nature and bifurcations also occur as a function of the parameter. In this context our numerical evidence shows that the gross measures of individual wavefunction localisation, such as entropy, are strongly correlated with the periodic orbit's stability oscillations (with a parameter). Berry's scar formula predicts infinite scar amplitude at all the points of pitchfork bifurcation. When the orbit loses stability we find that the entropy is also low, with the point of bifurcation being approximately the point of a local minimum in the entropy (again as a function of a parameter). However, when the orbit gains stability the entropy is not a minima, though Berry formula predicts an infinite scar amplitude at these points too. Thus we believe that apart from the stability of the scarring orbit, the scar enhancements

will also depend on the local structure of the phase space around it. The evidence for this argument comes from both the coupled quartic oscillator and the perturbed harmonic oscillator.

Finally, we also studied two different three-dimensional systems. One immediately recognises that possibilities exist for several hierarchies of scarred states due to freedom allowed by one more degree of freedom. This is also reflected in the eigenvalue statistics of these systems we studied in Chapter 5. We noticed significant deviations from the standard GOE curve for high values of the parameters of three-dimensional coupled quartic oscillator. Other independent studies have also come to similar conclusions for a different three-dimensional system.

This thesis, for most part, concerned itself with the quantum mechanics of some nonlinearly coupled oscillator models. Most of our conclusions and insights we got in to the working of 'quantum chaos' are essentially through the study of such model systems. Yet, what strikes us is the generality of the results, whether it is the validity or deviation from the random matrix predictions, localisation properties or the scaling of sections for a class of Hamiltonian systems. For instance, any chaotic quantum system which might show tendency towards localisation of its eigenstates or similar behaviour is likely to affect the statistics of eigenvalues and eigenvectors or any two-dimensional homogeneous Hamiltonian system will display parametric scaling properties we discussed earlier on in the thesis. Inspite of the general relevance of some of these results there are grey areas which can be improved upon in the coming years.

As of now, the parametric scaling we had proposed and verified numerically remains valid only for two-dimensional systems. One obvious extension would be look for scaling behaviour in three and possibly higher dimensional systems. Another possible course could be to study if similar parametric scaling properties exist in non-homogeneous systems. Even within the subclass of homogeneous systems, there are other possible varieties of Hamiltonian systems that could be important candidates for displaying classical scaling. Then, the question of the implications of scaling in the corresponding quantum systems could also be explored.

Any progress in the study of quantum chaotic systems is coupled with the progress in devising better algorithms and faster computers. The work presented in this thesis have significantly relied upon the computational resources. We were able to compute 2000 eigenstates from the ground states mainly because we succeeded in numerically banding the Hamiltonian matrix without using harmonic oscillator basis. As we enter the arena of three-dimensional systems, we recognise that the Hamiltonian matrix gets sparser depending on the kind of potential term in Hamiltonian. Hence the next step should be implement sparse matrix techniques to study the spectrum of their

highly excited states.

For the first time, we have reported on the existence of the shadow states. Since they too form a series in the quantum spectrum, it would be interesting to study the systematics and the periodic orbits associated with the shadow states. The Husimi distributions have been used as a tool in correlating classical invariant structures with the quantum density enhancements. From our own experience in dealing with complicated scarring orbits, we believe study of Husimi functions in the context of shadow states offers challenging problems and would reveal interesting dynamics.

The adiabatic approach, as applied to the channel localised states, is useful in qualitatively (sometimes quantitatively too) understanding this type of localisation, although it does not include the parameter of orbit stability. We can envisage improvements in the methodology to take into account these features. Although the eigenvalue estimates have had some success, eigenfunctions continue to be a challenge, even in the description of their grossest features. The eigenvector statistics for the smooth time-independent Hamiltonian systems should be systematically studied to gauge the extent of influence of the localised states in causing deviations from random matrix models.

The structure of the localised eigenstates showed remarkable universal characteristics. Our preliminary results from the eigenvectors of the three-dimensional system also confirm this view. Hence, it must be understood within a suitable theoretical framework. The oscillating stability of the underlying periodic orbits may play a key role in the presence of these localised states, and hence the question of the effect of stability on localisation has to be more rigorously established. Attempts should also be made to verify the scar theories of Berry and Bogomolny.

The field of three-dimensional systems is completely open and the attempts to study them have just begun. One of the important questions could be about the signatures, if at all any, of Arnold diffusion in quantum systems. While this could be ambitious, efficient methods must also be devised to handle eigenfunctions, Poincare sections and so on in three dimensions. On the other hand, systems that could be directly amenable to experimental possibilities should be taken up. Recently, Connerade [104] had proposed arguments for the occurance of quantum chaos in helium. He has also suggested possible experiments to verify the results. World over such experimental attempts using lasers and semiconductor quantum wells are on to study the properties of 'quantum chaos', which we hope will clarify the fundamental questions related to the world of quantum chaos.

Bibliography

[1] J. Shukla and M. J. Fennessy, J. Atmos. Sci., **45**, 9 (1988).

[2] *An Introduction to Chaotic Dynamical Systems*, Robert L. Devaney, (Addison-Wesley, 1987); see also J. Banks *et. al.* Am. Math. Monthly 332 (April, 1992).

[3] B. V. Chirikov *Lectures at the International Summer School "Nonlinear Dynamics and Chaos"*, Ljubljana, Slovenia (1994), LANL preprint number : chao-dyn/9705003.

[4] Joseph Ford, *Directions in Chaos*, ed by Hao Bai-Lin, (World Scientific, 1988); Physics Today, 40 April 1983 ; V. M. Alekseev and M. V. Yakobson, Phys. Rep. **75**, (1981).

[5] V. I. Arnold, *Mathematical Methods of Classical Mechanics* (Springer-Verlag, 1978).

[6] G. C. Benettin *et. al.* Nuovo Cimento B **79** 201 (1984).

[7] K. Ganesan and M. Lakshmanan, Phys. Rev. A **42**, 3940 (1990).

[8] D. Bohm and B. J. Hiley, Phys. Rep. **144** 323 (1987).

[9] U. Schwengelbeck and F. H. M. Faisal, Phys. Lett. A **199** 281 (1995).

[10] Ian Percival in *Order and Chaos in Nonlinear Physical Systems*, Ed. by Stig Lundquist, N. H. March and Mario Tosi, (Plenum Press, New York, 1988).

[11] J. M. Sanz-Serna in *Acta Numerica* 243-286 (1991); G. J. Marzyna and M. E. Tuckerman, J. Chem. Phys. **102** 8071 (1995).

[12] Friedrich H. and Wintgen D., Phys. Rep. **183** 37 (1989) and the references therein.

[13] H. Ruder, G. Wunner, H. Herold and F. Geyer, *Atoms in Strong Magnetic Fields* (Springer-Verlag, 1994).

[14] G. Casati, B. V. Chirikov and D. L. Shepelyansky, Phys. Rev. Lett. **53** 2525 (1984).

[15] J. E. Bayfield, G. Casati, I. Guarneri and D. W. Sokol, Phys. Rev. Lett. **63** 364 (1989).

[16] P. B. Wilkinson *et al.*, Nature **380** 608 (1996).

[17] R. C. Ashoori, Nature **379** 413 (1996).

[18] R. A. Jalabert, H. U. Baranger and A. D. Stone, Phys. Rev. Lett. **65** 2442 (1990).

[19] E. Akkermans, G. Montambaux, J.-L. Pichard and J. Zinn-Justin, (Eds) *Mesoscopic Quantum Physics* (North-Holland, Amsterdam, 1996).

[20] S. R. De Groot and L. G. Suttorp, *Foundations of Electrodynamics*, (North-Holland, Netherlands, 1972).

[21] M. C. Gutzwiller, *Chaos in Classical and Quantum Mechanics* (Springer-Verlag,New York, 1990).

[22] M. C. Gutzwiller in *Les Houches 1989 : Chaos and Quantum Physics*, edited by M. J. Giannoni, A. Voros and J. Zinn-Justin, (North-Holland, 1989).

[23] R. Balian and C. Bloch, Ann. Phys. **69** 76 (1972); **85** 514 (1974).

[24] I. C. Percival, J. Phys. B Atom. Molec. Phys. **6** L229 (1973).

[25] M. L. Mehta, *Random matrices and statistical theory of energy levels* (Academic Press, 1967); F. J. Dyson, J. Math. Phys. **3** 140 (1962).

[26] O. Bohigas, M. J. Giannoni and C. Schmit, Phys. Rev. Lett. **52** 1 (1984).

[27] M. V. Berry, Phil. Trans. Roy. Soc. Lond. **287** (1977).

[28] A. M. O. De Almeida, *Hamiltonian Systems : Chaos and Qantisation* (Cambridge Univ. Press., 1988).

[29] A. Voros, Annls. Inst. H. Poincare XXIV (1976).

[30] E. P. Wigner, Phys. Rev. **40** 749 (1932).

[31] A. I. Shnirelman, Usp. Mat. Nauk **29** 181 (1974)

[32] E. J. Heller, Phys. Rev. Lett. **53** 1515 (1984).

[33] M. V. Berry, Proc. R. Soc. Lond. A **423**, 219 (1989); see also M. V. Berry in *Les Houches : Chaos and Quantum Physics*, edited by M. -J. Giannoni, A. Voros and J. Zinn-Justin, (North-Holland, 1991).

[34] E. B. Bogomolny, Physica D **31** 169 (1988).

[35] S. Sridhar, Phys. Rev. Lett. **67**, 785 (1991).

[36] R. E. Prange, in *Proceedings of the Adriatico Conference on Quantum Chaos*, edited by : H. A. Cerdeira, R. Ramaswamy, M. C. Gutzwiller and G. Casati (World Scientific, 1991)

[37] P. W. Anderson, Phys. Rev. **109** 1492 (1958); N. F. Mott, Adv. Phys. **16** 49 (1967).

[38] A. R. P. Rau, Rev. Mod. Phys. **64** 623 (1992).

[39] B. V. Chirikov, F. M. Izrailev and D. L. Shepelyansky, Physica D (Special issue on nonlinear dynamics) **33** 77 (1988).

[40] O. Bohigas, S. Tomsovic and D. Ullmo, Phys. Rep. **223** 43 (1993).

[41] G. Casati and B. Chirikov (Eds), *Quantum Chaos : Between Order and Disorder* (Cambridge Univ. Press, 1995).

[42] B. V. Chirikov in *Les Houches : Chaos and Quantum Physics*, edited by M. -J. Giannoni, A. Voros and J. Zinn-Justin, (North-Holland, 1991).

[43] D. R. Grempel, R. E. Prange and S. Fishman, Phys. Rev. A **29** 1639 (1984).

[44] A. J. Lichtenberg and M. A. Lieberman, *Regular and chaotic dynamics*, (Springer-Verlag, 1992).

[45] P. Cvitanovic and B. Eckhardt, Nonlinearity **6** 273 (1993).

[46] L. D. Landau and E. M. Lifshitz, Classical Mechanics (Pergamon Press, 1960).

[47] V. I Arnold, *Mathematical Methods of Classical Mechanics* (Springer, New York, 1978).

[48] B. Eckhardt, Phys. Rep. **163** 205 (1988).

[49] H. Yoshida, Cel. Mech. **31** 363 (1983); Physica **D 29** 128 (1987).

[50] J. M. Mao and J. B. Delos, Phys. Rev. A **45** 1746 (1992).

[51] A. Lakshminarayan, M. S. Santhanam and V. B. Sheorey, Phys. Rev. Lett. **76** 396 (1996).

[52] S. G. Martinyan, G. K. Savvidi and T. A. Savvidi, Sov. Phys. JETP **53** 421 (1981).

[53] P. Dahlqvist and G. Russberg, Phys. Rev. lett. **65** 2837 (1990).

[54] B. Simon, Ann. Phys. **146** 209 (1983).

[55] J. M. Blatt, J. Comput. Phys. **1** 382 (1967); J. N. Bass, J. Comput. Phys. **9** 555 (1972).

[56] M. D. Feit, J. A. Fleck Jr. and A. Steiger, J. Comput. Phys. **47** 412 (1982).

[57] Michael Tinkham, *Group Theory and Quantum Mechanics*, (McGraw-Hill, 1964).

[58] M. V. Berry and M. Tabor, Proc. R. Soc. London**A356** 375 (1977).

[59] O. Bohigas, and M.-J. Giannoni, *Chaotic Motion and Random Matrix Theories*, IPNO-TH 84-22, (1984); See also Bohigas's artcle in [22].

[60] Biswas *et. al.*, J. Math. Phys. **14** 1190 (1973); A. Hautot, Phys. Rev. D **33** 437 (1986).

[61] K. Banerjee and J. K. Bhattacharjee, Phys. Rev. D **29** 1111 (1984).

[62] M. Tater and A. V. Turbiner, J. Phys. A Math. & Gen. **26** 697 (1993).

[63] Ulf Larsen, J. Phys. A Math. & Gen. **16** 2137 (1983).

[64] V. B. Sheorey, in *Proceedings of the Adriatico Conference on Quantum Chaos*, edited by : H. A. Cerdeira, R. Ramaswamy, M. C. Gutzwiller and G. Casati (World Scientific, 1991).

[65] URL of netlib : http://netlib.bell-labs.com/netlib

[66] A. S. Householder, *Theory of Matrices in Numerical Analysis* (Blaisdell Pub. Co., 1964); J. H. Wilkinson, *The Algebraic Eigenvalue Problem* (Clarendon Press, Oxford, 1965).

[67] J. Zakrzewski, K. Dupret and D. Delande, Phys. Rev. Lett. **74** 522 (1995).

[68] K. Muller, B. Mehlig, F. Milde and M. Schreiber, Phys. Rev. Lett. **78** 215 (1997)

[69] M. S. Santhanam, V. B. Sheorey and A. Lakshminarayan, Pramana- Journal of physics **48** 439 (1997).

[70] M. Feingold, J. Phys. A **30** 3603 (1997).

[71] B. Eckhardt, G. Hose and E. Pollak, Phys. Rev. A **39** 3776 (1989).

[72] M. S. Santhanam, V. B. Sheorey and A. Lakshminarayan, Mol. Phys. **88** 325 (1996).

[73] Husimi, Proc. Phys. Math. Soc. Jpn. **22** 264 (1940); K. Takahashi, Prog. Theor. Phys. Suppl. **98** 109 (1989).

[74] G. G. De Polavieja, F. Borondo and R. M. Benito, Int. J. quant. chem. **51** 555 (1994).

[75] C. E. Shannon and W. Weaver, *The Mathematical Theory of Communication*, (Univ. of Illinois Press, Urbana, 1949).

[76] E. T. Jaynes, Phys. Rev. **106** 620 (1957); Phys. Rev. **108** 171 (1957); Information Theory in Analytical chemistry, K. Echschlager (Wiley, NewYork, 1994); Optics and Information Theory, F. T. S. Yu (Wiley, London, 1976); Algorithmic Information Theory, G. J. Chaitin (Cambridge Univ. Press, 1987); R. P. Feynman, Found. Phys. **16** 507 (1986).

[77] Wootters W. K., Found. Phys. **20** (1990).

[78] Powell G. E. and Percival I. C., J. Phys. A **12** 2053 (1973).

[79] Izrailev F., Phys. Rep. **196** 299 (1990).

[80] Fritz Haake, *Quantum Signatures of Chaos* (Springer-Verlag, 1991).

[81] Porter C. E., (ed) *Statistical theories of spectra : Fluctuations* (Academic Press, New York., 1965).

[82] K. R. W. Jones, J. Phys. A **23**, L1247, (1990).

[83] K. Zyczkowski, in *Proceedings of the Adriatico Conference on Quantum Chaos*, edited by : H. A. Cerdeira, R. Ramaswamy, M. C. Gutzwiller and G. Casati (World Scientific, 1991).

[84] R. Aurich and F. Steiner, Physica D **64** 185 (1993).

[85] L. Benet, T. H. Seligman and H. A. Weidenmuller, Phys. Rev. Lett. **71** 529 (1993).

[86] M. Born and J. R. Oppenheimer, Ann. Phys. **84** 457 (1927).

[87] V. Aquilanti in *The theory of Chemical Reaction Dynamics*, edited by C. Clary (Reidel, Dordrecht, 1986).

[88] C. C. Martens, R. L. Waterland and W. P. Reinhardt, J. Chem. Phys. **90** 2328 (1989).

[89] A. Voros, J. Phys. A Math. & Gen. **21** 685 (1988).

[90] S. Sinha and V. B. Sheorey, Molec. Phys. **80** 1525 (1993).

[91] Zakrzewski J. and Marcinek R., Phys. Rev. A **42** 7172 (1990).

[92] K. M. Atkins and G. S. Ezra, Phys. Rev. E **51** 1822 (1955).

[93] R. A. Pullen and A. R. Edmonds, J. Phys. A **14** 1477 (1981).

[94] J. L. Anchell, J. Chem. Phys. **92** 4342 (1990).

[95] V. I. Arnold, Russian Math. Surveys, **18** 85 (1964).

[96] B. V. Chirikov, CERN Trans. 71 Geneva (1971); C. Froeschle, Astron. Astrophys. **16** 172 (1972); C. Froeschle and J. -P. Scheidecker, Phys. Rev. A **12** 2137 (1975).

[97] J. v. Milczewski, G. H. F. Diercksen and T. Uzer, Phys. Rev. Lett. **76** 2890 (1996).

[98] C. Froeschle, Astron. & Astrophys. **4** 115 1970; **5** 177 (1970).

[99] J. v. Milczewski, D. Farrelly and T. Uzer, Phys. Rev. Lett. **78** 1436 (1997).

[100] H. S. Dumas and J. Laskar, Phys. Rev. Lett. **70** 2975 (1993).

[101] Tomaz Prosen, chao-dyn/9611016, chao-dyn/9611015

[102] M. Lakshmanan and Sahadevan, Phys. Rep. **224** (1993).

[103] G. Herzberg, Molecular spectra & molecular structure, spectra of polyatomic molecules, Van Nostrand Reinhold Co., (1966).

[104] J-P Connerade, J. Phys. B At. Mol. Opt. Phys. **30** L-31 (1997).